

**SYNERGISTIC METROLOGY OF ANTI-FOULING  
PROPERTIES FOR MIXED SELF-ASSEMBLED  
MONOLAYERS**

A Dissertation Presented to  
the Faculty of the Department of Chemistry  
University of Houston

In Partial Fulfillment  
of the Requirements for the Degree of  
Doctor of Philosophy

By  
Lydia St. Hill  
May 2019

**SYNERGISTIC METROLOGY OF ANTI-FOULING  
PROPERTIES FOR MIXED SELF-ASSEMBLED  
MONOLAYERS**

---

Lydia St. Hill

APPROVED:

---

Dr. T. Randall Lee, Chairman

---

Dr. Arnold Guloy

---

Dr. Tom Teets

---

Dr. John Craft, Jr.

---

Dr. Shoujun Xu

---

Dr. Dan Wells  
Dean, College of Natural Sciences  
and Mathematics

*Dedicated to my husband, children, and parents*

*Adrian St. Hill, Abigail, Hannah, and Josh, David and Pamela Wersler*

*For the love and the outstanding support during my  
academic endeavor.*

## ACKNOWLEDGMENTS

Ever since the 9<sup>th</sup> grade, when I fell in love with chemistry, I knew I wanted to learn as much as I could and even one day earn a Ph.D.. I would like to acknowledge some pivotal people that have helped me on this endeavor.

First and foremost, is Jesus Christ my Lord and Savior who has provided much wisdom and grace through this journey. Secondly, Dr. Lee, thank you for your wisdom, guidance, and support. I appreciate your high expectations and your stern, but gentle approach, as I learned the ways of research. I would also like to extend my gratitude to my dissertation committee members for their time and counsel, and members of the Lee group. I would like to thank Dr. Chul Soon Park for taking me under your wing and showing me the ropes of the SAMs world. I thank Dr. Maria Marquez for her help editing my writing, and the words of wisdom provided about SAMs and adsorbates. I would like to thank the current group members, Tingting, Ploy, Riddihiman, Sam, Will, Parisa, and former group member Johnson for the many hours of conversations, life adventures we had, and the encouragement provided in a family like environment during this experience. I can't forget to thank Dr. Teddy for his constant presence and dedication to the graduate program. Finally, I would like to thank all previous and current Lee group members not mentioned.

I also would like to thank Dr. John Craft in Biology and Biochemistry at the University of Houston for great collaboration and conversations.

I am also grateful for all my friends and family for their support and prayers during this time. To my parents, there are not enough words of thanks and appreciation for all

that you have done to support me and my family through all of my adventures. To my husband, thank you for letting me walk away from my job and telling me "We will figure it out!" so I could go back to school and pursue my dream. Thank you for being there to support me throughout the entire process. I am especially thankful that you guys listen to what I am saying even if you have no clue, and continue to support my efforts. To my children, thank you for letting me take away from "mommy time" to pursue my dreams. Even if I did not get to your event, my heart was always and will always be there with you. It is now time to continue our journey as the St. Hill Family.

Thank you all for everything.

Lydia St. Hill

**SYNERGISTIC METROLOGY OF ANTI-FOULING  
PROPERTIES FOR MIXED SELF-ASSEMBLED  
MONOLAYERS**

An Abstract of a Dissertation

Presented to

the Faculty of the Department of Chemistry

University of Houston

In Partial Fulfillment

of the Requirements for the Degree of

Doctor of Philosophy

By

Lydia St. Hill

May 2019

## ABSTRACT

The work presented in this dissertation focuses on studying the anti-fouling behavior of "conflicted" interfaces, where phase separation is restricted or eliminated, using self-assembled monolayers (SAMs). The adsorbates used to generate the SAMs were comprised of chemically disparate species that are held in close proximity, while preferring to be apart. Three types of SAM surfaces were generated for this dissertation from unsymmetrical partially fluorinated spiroalkanedithiols, unsymmetrical oligo(ethylene glycol) spiroalkanedithiols, and various mixtures of hydrocarbon and partially fluorinated aromatic dithiol adsorbates. All of the bidentate SAM surfaces, spiroalkanedithiol and aromatic dithiol, were compared to the monothiol analogs to evaluate their anti-fouling properties. Properties were investigated with a synergistic approach using ellipsometry, surface plasmon resonance (SPR) spectroscopy, quartz crystal microbalance (QCM), and atomic force microscopy (AFM). The "conflicted" nature of the surfaces was found to positively impact the anti-fouling properties of the SAMs, particularly where the surface was comprised of a mixed partially fluorinated interface. However, the architecture and nature of the conflicted oligo(ethylene glycol) spiroalkanedithiol adsorbate proved detrimental towards the anti-adhesive properties of these types of SAMs. The various analytical techniques provide a robust synergistic characterization method with reproducibility to determine anti-fouling properties of self-assembled monolayers.

# TABLE OF CONTENTS

	<u>Page</u>
Acknowledgments	iv
Abstract	vii
Table of Contents	viii
List of Figures	xii
List of Tables	xx
<b>Chapter 1</b>	<b>A Practical Guide to Synergistic Characterization of</b>
	<b>Biofilm Formation on Self-Assembled Monolayers</b>
	1
1.1	Introduction
	1
1.2	Surface Plasmon Resonance Spectroscopy
	4
1.2.1	Basic Principles of Surface Plasmon Resonance Spectroscopy
	4
1.2.2	Experimental Setup for SPR Spectroscopy
	7
1.2.3	Interpreting Sensorgrams
	8
1.2.4	Surface Plasmon Resonance Spectroscopy for <i>In Situ</i> Protein Interactions
	10
1.3	Quartz Crystal Microbalance
	11
1.3.1	Basic Principles of Quartz Crystal Microbalance
	11
1.3.2	Types of Measurements for Quartz Crystal Microbalance
	14
1.3.3	Quartz Crystal Microbalance Experimental Setup
	15
1.3.4	Quartz Crystal Microbalance Measurements
	15

1.3.5	Quartz Crystal Microbalance Utilized to Monitor Protein Interactions	16
1.4	Atomic Force Microscopy	17
1.4.1	Basic Principles of Atomic Force Microscopy	17
1.4.2	Atomic Force Microscopy Experimental Setup	19
1.4.3	Atomic Force Microscopy Image Evaluation	20
1.4.4	AFM Investigations to Probe Protein Adhesion	23
1.5	Ellipsometry	24
1.5.1	Basic Principles of Ellipsometry	24
1.5.2	Types of Ellipsometry	25
1.5.3	Ellipsometry Experimental Setup	26
1.5.4	Ellipsometric Measurements	27
1.5.5	Monitoring Biofilm Formation with Ellipsometry	28
1.6	X-Ray Photoelectron Spectroscopy	29
1.6.1	Basic Principles of X-Ray Photoelectron Spectroscopy	29
1.6.2	Experimental Setup	31
1.6.3	Chemical Analysis of Protein Absorption using XPS	32
1.7	Synergistic Instrumentation	34
1.7.1	Types of Synergistic Instrumentation	35
1.7.2	Synergistic Analysis In Complementary Techniques	35
1.8	Conclusions	36
1.9	References	38

<b>Chapter 2</b>	Anti-fouling Studies of Partially Fluorinated Spiroalkanedithiol Self-Assembled Monolayers	57
2.1	Introduction	57
2.2	Experimental Section	61
2.2.1	Materials	61
2.2.2	Preparation of Substrates	62
2.2.3	Preparation of SAMs	62
2.2.4	Protein Preparation/Exposure	62
2.2.5	Ellipsometry Measurements	63
2.2.6	SPR Procedures	64
2.2.7	QCM Measurements	64
2.2.8	AFM Imaging and Measurements	65
2.3	Results and Discussion	65
2.3.1	<i>In Situ</i> Analysis of Protein Adhesion Using SPR Spectroscopy	69
2.3.2	<i>Ex Situ</i> Analysis of Protein Adhesion Using QCM	73
2.3.3	Ellipsometric Thickness Measurements	77
2.3.4	Evaluation of Surface Topography Using AFM	80
2.4	Conclusions	88
2.5	References	90
<b>Chapter 3</b>	Biofouling Studies of Unsymmetrical Oligo(ethylene glycol) Spiroalkanedithiols	101
3.1	Introduction	

3.2	Experimental Section	104
3.2.1	Materials	104
3.2.2	Preparation of Substrates	105
3.2.3	Preparation of SAMs	106
3.2.4	Protein Preparation/Exposure	106
3.2.5	Ellipsometry Measurements	106
3.2.6	SPR Procedures	107
3.2.7	QCM Measurements	108
3.2.8	AFM Imaging and Measurements	109
3.3	Results and Discussion	110
3.3.1	<i>In Situ</i> Analysis of Protein Adhesion Using SPR Spectroscopy	111
3.3.2	Ellipsometric Thickness Measurements	116
3.3.3	<i>Ex Situ</i> Analysis of Protein Adhesion Using QCM	119
3.3.4	Evaluation of Surface Topography Using AFM	124
3.4	Conclusions	133
3.5	References	135
<b>Chapter 4</b>	<b>Characterization and Anti-fouling Performance of Mixed Bidentate Self-Assembled Monolayers</b>	<b>145</b>
4.1	Introduction	145
4.2	Experimental Section	148
4.2.1	Materials	148

4.2.2	Preparation of Substrates	149
4.2.3	Preparation of SAMs	150
4.2.4	Protein Preparation/Exposure	151
4.2.5	Ellipsometry Measurements	151
4.2.6	X-ray Photoelectron Spectroscopy (XPS) Measurements	152
4.2.7	Quartz Crystal Microbalance Measurements	152
4.2.8	Atomic Force Microscopy Imaging and Evaluation	153
4.3	Results and Discussion	154
4.3.1	Characterization of SAMs Formation with Varied Surfactant Ratios	154
4.3.1.1	Characterization by XPS	154
4.3.1.2	QCM Characterization of the Mixed SAMs	156
4.3.2	Anti-fouling Properties of the Mixed SAMs	158
4.3.2.1	Quartz Crystal Microbalance Analysis of Protein Adhesion	159
4.3.2.2	Ellipsometric Thickness Measurements of Protein Adhesion	162
4.3.2.3	Evaluation of Surface Topography by AFM	164
4.4	Conclusions	173
4.5	References	174
<b>Chapter 5</b>	<b>Conclusions</b>	<b>184</b>

## LIST OF FIGURES

	<u>Page</u>
1.1 Schematic illustration depicting the three types of functional groups which exhibit antifouling properties	3
1.2 Schematic illustration (A) refraction occurs when polarized light is deflected as it passes through the prism until it reaches the critical angle ( $\theta$ ) and (B) total internal reflection occurs when polarized light enters the prism with a metal film attached to the flat surface which causes the light to reflect like a mirror when it interacts with the metal film.	5
1.3 Schematic diagram of surface plasmon resonance flow cell when a light source passes through a prism and strikes the surface of the flow cell at an angle of total internal reflection, where the interactions of the surface of the gold sensor reduce the intensity of the light beam to generate a response signal in the reflected light.	8
1.4 Diagram of sensorgram for SPR measurements including initial buffer response (gray line), association with the protein solution (blue line), saturation at the steady state (red line), and dissociation (green line). The change in response units ( $\Delta$ RU) are determined by subtracting the response units after dissociation from the initial buffer response indicated by the purple line.	9
1.5 Schematic diagram of a shear wave modulus with applied voltage causes reorganization of the dipoles producing strain resulting in	

	an alternating potential across the surface of the crystal and generating a standing wave	12
1.6	Schematic illustration of the QCM setup depicting changes in the frequency signal of the oscillating sensor when mass changes occurs for different layers.	15
1.7	Schematic illustration of an atomic force microscope imaging a sample by analyzing the cantilevers deflections with a photodetector.	20
1.8	Schematic illustration of peak count determination by bandwidth.	22
1.9	Schematic diagram illustrating polarized light reflecting from a sample surface and the change in polarization is analyzed for a typical ellipsometry setup, $\phi$ is the angle of incidence.	27
1.10	Schematic illustration depicting an irradiated sample surface that emitted photoelectrons that are collected and analyzed by an x-ray photoelectron spectrometer.	32
1.11	XPS spectra in the N 1s region for surfaces exposed to protein. Adapted with permission from Reference 76. Copyright 2009 American Chemical Society.	33
2.1	Molecular structures of unsymmetrical spiroalkanedithiols (SADTs) prepared by the Chinwangso et al.	59
2.2	Molecular structures of the adsorbates and illustration of SAMs derived from the monodentate, <b>C16SH</b> and <b>F8H8SH</b> , as well as	

	the SADT adsorbates, <b>F8H10-C12</b> and <b>F8H10-C18</b> , analyzed in this study.	60
2.3	(A) Inferred changes in the thickness from ellipsometry of the SAMs generated from <b>C16SH</b> , <b>F8H8SH</b> , <b>F8H10-C12</b> , and <b>F8H10-C18</b> after exposure to solutions of protamine, lysozyme, BSA, and fibrinogen. (B) SPR data (C) QCM Mass loading calculations.	67
2.4	SPR sensorgrams of the SAMs exposed to (A) protamine, (B) lysozyme, (C) BSA, and (D) fibrinogen. Protein solutions were prepared at a concentration of 1 mg/mL in a PBS buffer solution.	70
2.5	Change in frequency vs. time for SAMs derived from <b>C16SH</b> , <b>F8H8SH</b> , and <b>F8H10-C12</b> , and <b>F8H10-C18</b> after 1 h exposure to 1 mg/mL of protein in PBS solution: (A) protamine, (B) lysosome, (C) BSA, and (D) fibrinogen.	75
2.6	Topography after exposure to protamine for (A, E) <b>C16SH</b> , (B, F) <b>F8H8SH</b> , (C, G) <b>F8H10-C12</b> , and (D, H) <b>F8H10-C18</b> at 5 $\mu\text{m} \times 5 \mu\text{m}$ (top) and 1 $\mu\text{m} \times 1 \mu\text{m}$ (bottom).	81
2.7	Topography after exposure to lysozyme for (A, E) <b>C16SH</b> , (B, F) <b>F8H8SH</b> , (C, G) <b>F8H10-C12</b> , and (D, H) <b>F8H10-C18</b> at 5 $\mu\text{m} \times 5 \mu\text{m}$ (top) and 1 $\mu\text{m} \times 1 \mu\text{m}$ (bottom).	82

2.8	Topography after exposure to BSA for (A, E) <b>C16SH</b> , (B, F) <b>F8H8SH</b> , (C, G) <b>F8H10-C12</b> , and (D, H) <b>F8H10-C18</b> at 5 $\mu\text{m} \times 5 \mu\text{m}$ (top) and 1 $\mu\text{m} \times 1 \mu\text{m}$ (bottom).	82
2.9	Topography after exposure to fibrinogen for (A, E) <b>C16SH</b> , (B, F) <b>F8H8SH</b> , (C, G) <b>F8H10-C12</b> , and (D, H) <b>F8H10-C18</b> at 5 $\mu\text{m} \times 5 \mu\text{m}$ (top) and 1 $\mu\text{m} \times 1 \mu\text{m}$ (bottom).	83
2.10	Comparison of average roughness ( $R_a$ ) and root mean square (Rms) values for each of the SAMs ( <b>C16SH</b> , <b>F8H8SH</b> , <b>F8H10-C12</b> , and <b>F8H10-C18</b> ) after exposure to protamine, lysozyme, BSA, and fibrinogen, respectively.	83
2.11	Distribution density plots for <b>C16SH</b> , <b>F8H8SH</b> , <b>F8H10-C12</b> , and <b>F8H10-C18</b> after exposure to (A) protamine, (B) lysozyme, (C) BSA, and (D) Fibrinogen determined from AFM images.	87
3.1	Molecular structures of the monodentate, <b>C18SH</b> and <b>EG3C7SH</b> , as well as the bidentate, <b>EG3C7-C18</b> and <b>EG3C7-C7</b> , adsorbates analyzed in this study.	104
3.2	SPR sensorgrams of the SAMs ( <b>C18SH</b> , <b>EG3C7SH</b> , <b>EG3C7-C7</b> and <b>EG3C7-C18</b> ) exposed to (A) protamine, (B) lysozyme, (C) BSA, and (D) fibrinogen. Protein solutions were prepared at a concentration of 1 mg/mL in a PBS buffer.	112
3.3	Graphical representation of the $\Delta\text{RU}$ values for the SAMs after exposure to a 300 $\mu\text{L}$ injection of 1 mg/mL protein solution.	116

3.4	Changes in the thickness of the SAMs generated from <b>C18SH</b> , <b>EG3C7SH</b> , <b>EG3C7-C7</b> , and <b>EG3C7-C18</b> after exposure to solutions of protamine, lysozyme, BSA, and fibrinogen.	118
3.5	Change in frequency vs. time for SAMs derived from <b>C18SH</b> , <b>EG3C7SH</b> , and <b>EG3C7-C7</b> , and <b>EG3C7-C18</b> after 1 h exposure to 1 mg/mL of protein in PBS solution: (A) protamine, (B) lysosome, (C) BSA, and (D) fibrinogen.	121
3.6	Graphical presentation of the calculated values for the mass loading of proteins onto the SAMs derived from <b>C18SH</b> , <b>EG3C7SH</b> , <b>EG3C7-C7</b> , and <b>EG3C7-C18</b> after exposure to 1mg/mL protein solution in PBS for 1 h.	123
3.7	Topography after exposure to protamine for (A, E) <b>C18SH</b> , (B, F) <b>EG3C7SH</b> , (C, G) <b>EG3C7-C7</b> , and (D, H) <b>EG3C7-C18</b> at 5 $\mu\text{m}$ $\times$ 5 $\mu\text{m}$ (top) and at 1 $\mu\text{m}$ $\times$ 1 $\mu\text{m}$ (bottom).	124
3.8	Topography after exposure to lysozyme for (A, E) <b>C18SH</b> , (B, F) <b>EG3C7SH</b> , (C, G) <b>EG3C7-C7</b> , and (D, H) <b>EG3C7-C18</b> at 5 $\mu\text{m}$ $\times$ 5 $\mu\text{m}$ (top) and at 1 $\mu\text{m}$ $\times$ 1 $\mu\text{m}$ (bottom).	125
3.9	Topography after exposure to BSA for (A, E) <b>C18SH</b> , (B, F) <b>EG3C7SH</b> , (C, G) <b>EG3C7-C7</b> , and (D, H) <b>EG3C7-C18</b> at 5 $\mu\text{m}$ $\times$ 5 $\mu\text{m}$ (top) and at 1 $\mu\text{m}$ $\times$ 1 $\mu\text{m}$ (bottom).	125
3.10	Topography after exposure to fibrinogen for (A, E) <b>C18SH</b> , (B, F) <b>EG3C7SH</b> , (C, G) <b>EG3C7-C7</b> , and (D, H) <b>EG3C7-C18</b> at 5 $\mu\text{m}$ $\times$ 5 $\mu\text{m}$ (top) and at 1 $\mu\text{m}$ $\times$ 1 $\mu\text{m}$ (bottom).	126

3.11	Average roughness ( $R_a$ ) and root mean square (Rms) values for each of the SAM surfaces ( <b>C18SH</b> , <b>EG3C7SH</b> , <b>EG3C7-C7</b> , and <b>EG3C7-C18</b> ) after exposure to protamine, lysozyme, BSA, and fibrinogen.	129
3.12	Height density distributions for each of the SAM surfaces ( <b>C18SH</b> , <b>EG3C7SH</b> , <b>EG3C7-C7</b> , and <b>EG3C7-C18</b> ) after exposure to (A) protamine, (B) lysozyme, (C) BSA, and (D) fibrinogen.	130
4.1	Molecular structures of the bidentate adsorbates, <b>PF PDT</b> and <b>HDPDT</b> , used to derive mixed SAMs in this study.	147
4.2	X-ray photoelectron spectra of the (A) Au 4f, (B) C 1s, (C) F 1s, and (D) S 2p regions of the mixed SAMs derived from the bidentate alkanethiols ( <b>PF PDT</b> and <b>HDPDT</b> ).	155
4.3	XPS elemental composition for the mixed SAMs derived from the bidentate alkanethiols in ethanol. (A) The fluorine to carbon (F/C) ratios and (B) the gold to fluorine (Au/F) ratio. Error bars indicate the standard deviation for the data. Error bars not visible fall within the symbols.	156
4.4	Mass loading of the SAMs on QCM sensors compared to the theoretical values.	158
4.5	Calculated mass loading values determined by QCM for the mixed SAMs, <b>PF PDT1</b> , <b>PF PDT75</b> , <b>PF PDT50</b> , <b>PF PDT25</b> , and <b>HDPDT1</b> , after exposure to 1 mg/mL of protein in PBS solution for 1 h.	160

4.6	Graphical representation of the changes in film thickness of the mixed SAMs derived from the bidentate alkanethiols ( <b>PF PDT</b> and <b>HDPDT</b> ) after exposure to protein solutions.	164
4.7	Topography after exposure to protamine for (A, F) <b>PF PDT1</b> , (B, G) <b>PF PDT75</b> , (C, H) <b>PF PDT50</b> , (D, I) <b>PF PDT25</b> and (E, J) <b>HDPDT1</b> at $5\ \mu\text{m} \times 5\ \mu\text{m}$ (top) and $1\ \mu\text{m} \times 1\ \mu\text{m}$ (bottom).	166
4.8	Topography after exposure to lysozyme for (A, f) <b>PF PDT1</b> , (B, G) <b>PF PDT75</b> , (C, H) <b>PF PDT50</b> , (D, I) <b>PF PDT25</b> and (E, J) <b>HDPDT1</b> at $5\ \mu\text{m} \times 5\ \mu\text{m}$ (top) and $1\ \mu\text{m} \times 1\ \mu\text{m}$ (bottom).	166
4.9	Topography after exposure to BSA for (A, f) <b>PF PDT1</b> , (B, G) <b>PF PDT75</b> , (C, H) <b>PF PDT50</b> , (D, I) <b>PF PDT25</b> and (E, J) <b>HDPDT1</b> at $5\ \mu\text{m} \times 5\ \mu\text{m}$ (top) and $1\ \mu\text{m} \times 1\ \mu\text{m}$ (bottom).	167
4.10	Topography after exposure to fibrinogen for (A, F) <b>PF PDT1</b> , (B, G) <b>PF PDT75</b> , (C, H) <b>PF PDT50</b> , (D, I) <b>PF PDT25</b> and (E, J) <b>HDPDT1</b> at $5\ \mu\text{m} \times 5\ \mu\text{m}$ (top) and $1\ \mu\text{m} \times 1\ \mu\text{m}$ (bottom).	167
4.11	Comparison of average roughness ( $R_a$ ) and root mean square ( $R_{ms}$ ) values for each of the mixed SAM surfaces ( <b>PF PDT1</b> , <b>PF PDT75</b> , <b>PF PDT50</b> , <b>PF PDT25</b> , and <b>HDPDT1</b> ) after exposure to protamine, lysozyme, BSA, and fibrinogen, respectively.	169
4.12	Height distribution density plots determined from AFM images of the <b>PF PDT1</b> , <b>PF PDT75</b> , <b>PF PDT50</b> , <b>PF PDT25</b> , and <b>HDPDT1</b> SAMs after exposure to (A) protamine, (B) lysozyme, (C) BSA, and (D) fibrinogen.	172

## LIST OF TABLES

	<u>Page</u>
2.1 Physical Properties of Proteins Examined in this	68
2.2 The $\Delta$ RU for SAMs after Exposure to 300 $\mu$ L Injection of 1 mg/mL Protein Solution	69
2.3 Calculations of Mass loading for SAMs derived from <b>C16SH</b> , <b>F8H8SH</b> , <b>F8H8-C12</b> , and <b>F8H8-C18</b> after 1 h exposure to 1 mg/mL of protein in PBS solution.	74
2.4 Ellipsometric Thickness Values of SAMs Used to Confirm SAMs Formation	79
2.5 Change in Ellipsometric Thickness Values of the SAMs after Exposure to 1mg/mL of Protein Solution in PBS Buffer	79
2.6 Calculated $R_a$ Values for the Surfaces in this Study	84
2.7 Calculated Rms Values for the Surfaces in this Study	85
3.1 Physical Properties of Proteins Examined in this Investigation	111
3.2 The $\Delta$ RU Values for SAMs after Exposure to 300 $\mu$ L Injection of 1 mg/mL Protein Solution	114
3.3 Ellipsometric Thickness Values of the SAMs Prior to Exposure to Proteins	117
3.4 Changes in Ellipsometric Measurement Values after Exposure to 1 mg/ml in PBS Protein Solutions of Protamine, Lysozyme, BSA, and Fibrinogen for <b>C18SH</b> , <b>EG3C7SH</b> , <b>EG3C7-C7</b> , and <b>EG3C7-C18</b> Adsorbates	119

3.5	Calculated Values for Mass Loading of the SAMs after 1 h Exposure to 1 mg/mL of Protein in PBS Solution	120
3.6	The $R_a$ Values of the Surface Roughness of the SAMs after Exposure to Proteins	127
3.7	The Rms Values of the Surface Roughness of the SAMs after Exposure to Proteins	128
4.1	Mole Fractions of Adsorbates Used to Generate the Mixed SAMs	150
4.2	Ellipsometric Film Thickness Values of the Mixed SAMs	154
4.3	Mass Loading of Surfaces Coated with Mixed SAMs and theoretical values	158
4.4	Physical Properties of Proteins Examined in this Investigation	159
4.5	QCM Mass Loading Values after Exposure to Protein Solutions	161
4.6	Change in Ellipsometric Thickness Values for the Mixed SAMs after Exposure to Protein Solutions	164
4.7	Calculated $R_a$ Values for the Mixed SAMs	169
4.8	Calculated Rms Values for the Mixed SAMs	170

## **Chapter 1. A Practical Guide to Synergistic Characterization of Biofilm Formation on Self-Assembled Monolayers**

### **1.1. Introduction**

Biofouling is a large scale issue that impacts numerous systems, including medical devices,<sup>1-6</sup> pipelines,<sup>7-9</sup> as well as marine shipping and equipment.<sup>10-13</sup> Surfaces in contact with a liquid environment have the potential to build up algae, microorganisms, plants, or animals on the surface. Interactions with proteins tend to result in biofilm formation, which with continued contact lead to cell adhesion and other biological attachments to the surface, increasing the biofilm layer.<sup>9</sup> Biofouling alone costs the marine shipping industry a considerable amount more in fuel cost as a result from drag, additionally of the increased amount of fuel generates greater CO<sub>2</sub> emissions.<sup>10,13,14</sup> With respect to industrial pipelines, biofilms cause structural fatigue, leading to pipeline failure which ultimately require costly repairs and increased production costs.<sup>7,8</sup> With regard to biocompatible medical devices, protein adsorption impedes and degrades the performance of implants, biosensors, catheters, or artificial organs.<sup>15</sup>

There have been great efforts to generate coatings that will reduce or limit biofouling, known as anti-fouling agents. Nanostructures, specifically thin films that are only 1-2 nm thick, are being immensely investigated for their anti-fouling properties. Thin film coatings have proven important due to their added protection to surfaces to limit corrosion and degradation resulting in extended product longevity. As a result of the value that thin films contribute, extensive research has been done in the field of thin film coatings. A long-time research goal of scientists has been to be able to understand, at a molecular level, how the surface, or the thin film coating, interacts with foulants to predict or rationalize

the interactions. Once the understanding of how a system interacts with the foulant, better surface coatings can be developed. To generate thin film coatings that resist or minimize protein adhesion, a basic understanding of factors that influence the interaction at the interface of the protein and surface must be understood.<sup>16</sup> The protein and surface interface contain several factors that contribute toward the energetics of the interaction stemming from multiple sources, including van der Waals, electrostatic, and hydrogen bonding components.<sup>17</sup> Although distinctions between the individual contributions has been difficult to distinguish, it has been suggested that electrostatic interactions may be minimized with electrical neutrality, and hydrogen bonding interactions might be minimized with the absence of hydrogen bond donors.<sup>17</sup>

Since the mechanism of protein resistance is still not clear, scientists have explored three main types of functional groups that exhibit anti-fouling properties, see Figure 1.1: fluorinated, PEGylated, and zwitterionic. The discovery of polytetrafluorethylene (PTFE), also commonly known as Teflon, ignited great interest in fluorinated materials, specifically as surface coatings. Incorporation of fluorocarbons into organic materials imparts unique interfacial chemistry, such as low surface free energy, low adhesion, and chemical resistance and durability.<sup>18-20</sup> Thin film research utilizing self-assembled monolayers (SAMs) has investigated the use of partially fluorinated molecules to examine the properties of the films as the amount of fluorination varies.<sup>16,20,29-34,21-28</sup> The second functional group of interest is polyethylene glycol (PEG), also known as polyethylene oxide (PEO), which has been a widely used as a biocompatible material to coat biological materials. PEG-based surfaces exhibit solubility of the coating in aqueous and organic solutions, lack of toxicity, and the ability to alter the electrical nature of the surface. It is

also notable that PEG-coated surfaces fail to degrade proteins.<sup>35</sup> The properties of PEG-, or oligoethylene glycol- (OEG), based SAMs have also been analyzed for use as anti-fouling materials.<sup>16,21,41,22-24,36-40</sup> The last functional group exhibiting antifouling properties are zwitterionic groups, which contain an overall balanced charged group. The zwitterionic material has both a negatively charged and positively charged region within the same molecule which prevent protein adhesion through the generation of a strong hydration layer.<sup>6,17,21,42-47</sup> However, the synthesis of stable and resilient compounds capable of generating improved coatings, along with methods to better characterize the performance of the generated surfaces are still necessary.

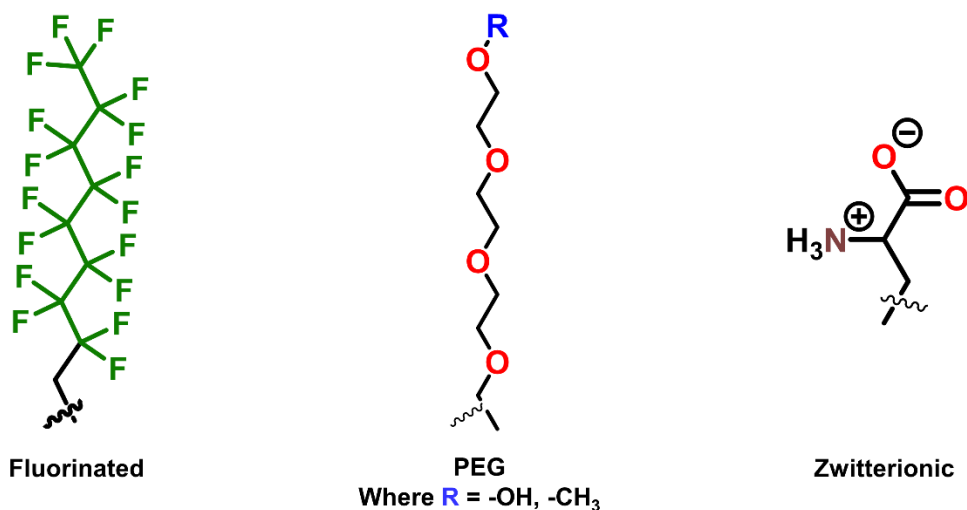


**Figure 1.1.** Schematic illustration depicting the three types of functional groups which exhibit antifouling properties.

To study the interactions between the aforementioned surfaces and foulants, a model system is necessary. The ideal model system should include the following components. First, well known biologics, such as proteins that vary in properties and structure, must be selected. Second, a surface that is structurally well defined, but can also be tailored with control to the environment to allow for maximum interaction parameters.

Lastly, a variety of analytical techniques that can be used to probe the interactions that will allow not only qualification but also quantification of the amount of protein interactions with the surface.<sup>16</sup> Nanostructures ranging in size from 1-2 nm that generate thin film coatings through the process of self-assembly are an excellent model system. SAMs are highly ordered, homogeneous and well-defined systems that possess the ability to be tailored to study the interactions between a substrate and a variety of biocontaminants.<sup>48</sup> This review intends to highlight various analytical techniques, along with literature examples where biofilm formation is characterized and quantified atop thin film coatings. It is our hope to obtain a better understanding of protein interactions with various surfaces by applying a multi-technique approach to maximize knowledge of protein-surface interactions. The techniques highlighted in this chapter are Surface Plasmon Resonance Spectroscopy (SPR), Quartz Crystal Microbalance (QCM), Atomic Force Microscopy (AFM), ellipsometry, and X-Ray Photoelectron Spectroscopy (XPS).

## **1.2. Surface Plasmon Resonance Spectroscopy**

### **1.2.1. Basic Principles of Surface Plasmon Resonance Spectroscopy**

A phenomenon that is of great interest and has been studied using spectroscopic techniques is surface plasmon resonance (SPR). SPR is widely used in a variety of applications, such as biosensors, reaction kinetics, and enhancements of signals. There are two reported methods for the excitation of surface plasmons. The first technique involves surface plasmon waves excited by attenuated total reflection using a prism-coupler-based structure. The second method, an alternative to the aforementioned method, involves diffraction at diffraction gratings. Beginning in the early 1980's, the latter technique became widely applied to study interactions between stationary receptors and analytes in

solutions. The main attractive feature of SPR is the ability to conduct *in situ* studies to understand reaction rates and kinetics, without the need for contact or labeling.<sup>49-56</sup>

The basis for the SPR technique relies on light that is reflected and absorbed at different angles and a measurement of the change of the angle of minimum reflected intensity. To determine which angles are reflected and which are not, the concept of total internal reflection (TIR) is invoked and is illustrated in Figure 1.2B. In a half sphere prism, as seen in Figure 1.2A, a beam of light is directed perpendicular to the middle of the flat side, and the angle of incidence is gradually increased. The angle,  $\theta$ , is between the beam and the line  $90^\circ$  to the flat surface. At an angle of incidence of zero, the beam will exit the sphere prism on the flat side. As the angle is increased, the refractions get closer and closer to the flat surface, until they reach a critical angle. At the critical angle, the beam is parallel to the flat surface of the sphere. At this point, it changes to reflection with no light passing through the prism, thus results in total internal reflection. Even though the light no longer reflects out of the prism the electric field from the light extends about a quarter of a wavelength beyond the reflecting surface.<sup>57-60</sup>

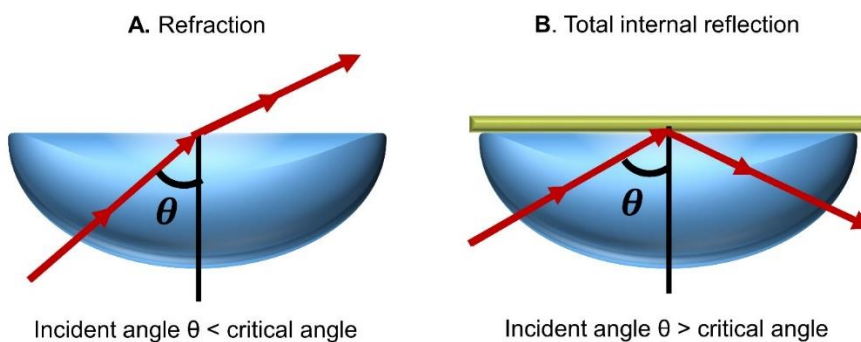


**Figure 1.2.** Schematic illustration (A) refraction occurs when polarized light is deflected as it passes through the prism until it reaches the critical angle ( $\theta$ ) and (B) total internal reflection occurs when polarized light enters the prism with a metal film attached to the flat surface which causes the light to reflect like a mirror when it interacts with the metal film.

Adding a noble metal film to the flat side of a hemispheric prism and shining polarized light on the same system allows the light to reflect like a mirror when it interacts with the metal film. The metal layer contains free valence band and conduction-band electrons. The electric field from the light is able to interact with the metal electrons on the surface of the metal film to generate wave-like oscillations. The oscillations reduce the reflected light's intensity as the incident light photons are absorbed and the energy is transferred to the electrons. The energy is then converted into surface plasmons. This behavior can only be described if both wave and particle properties are exhibited. In TIR, when the quantum energy of the photon matches the energy of the electrons, the photons are converted to plasmons, leaving a gap in intensity of the reflected light.

During the conversion of a photon to plasmon, momentum and energy must be conserved. The momentum of the plasmon are influenced by the nature of the metal film and the media on both sides of the film. Resonance occurs when the momentum of the photons equals the momentum of the plasmons. Using a vector function with magnitude and direction, the momentum of the photons and the plasmons can be described. When the angle or wavelength of the incident light change, the magnitude also changes. When the angle of incidence changes, the intensity of the light can pass through a minimum. At the minimum, the light produces plasmons on the surface, which results in a decrease in the intensity of the light that is reflected; also known as surface plasmon resonance. When the intensity of the reflected light is at the maximum, the SPR angle, or resonance angle, occurs. This angle is dependent on optical properties of the metal surface, such as the refractive index of the media.

Any shift observed in the SPR angle can be related to a change in the conditions of the system. The conditions of the system include the properties of the metal, wavelength of the incident light, and the refractive index of the media, which is temperature dependent. The metal must contain conduction band electrons to resonate with the incoming light at the correct wavelength. The light source should be monochromatic and polarized in the plane of the surface. Since plasmons are confined to the surface of the metal plate, the only vector that needs to be considered in SPR is the part of the momentum that is parallel to the surface. When the plasmon momentum is equal to the parallel plane, part of the specific incident angle of light resonance is observed. Ultimately, to produce SPR, the energy and the angle of incident light must match. Studies that involve SPR allow for real time data collection without the use of labeling. Also, the observed binding rates and response signal levels allow for interpretation of specificity, kinetics affinity, or concentration of the analyte. For more detailed information about theory and the surface plasmon resonance spectroscopy technique, literature can be reviewed.<sup>49,54,56-59,61</sup>

### **1.2.2. Experimental Setup for SPR Spectroscopy**

The experimental arrangement that is shown in Figure 1.3 is based on Kretschmann's work.<sup>62</sup> A light source produces a parallel and monochromatic light that is polarized and parallel to the plane of incidence. The light passes through a half-sphere quartz glass irradiating the surface of a thin metal film. The film has optical contact with the plane of the quartz glass sphere. The angle of incidence must satisfy the conditions of Equation 1.1, where the interactions with these conditions cause the surface plasma waves to be excited at the metal-air boundary reducing the light intensity and generating a response signal.

$$\theta_0 = \arcsin \left\{ \frac{1}{\epsilon_2} \frac{\epsilon(\lambda)}{[\epsilon(\lambda)+1]} \right\}^{1/2} \quad (1.1)$$

Where  $\theta_0$  is the angle of incidence,  $\epsilon$  is the dielectric constant and  $\lambda$  is the wavelength of the light source.

The emitted light passing through the quartz glass is detected by a photomultiplier. Measurements in regards to the intensity of the light scattering in the plane that is at  $90^\circ$  to the plane of incidence as a function of the angle of observation ( $\theta$ ) are recorded. The data is analyzed by software which produces a sensorgram.

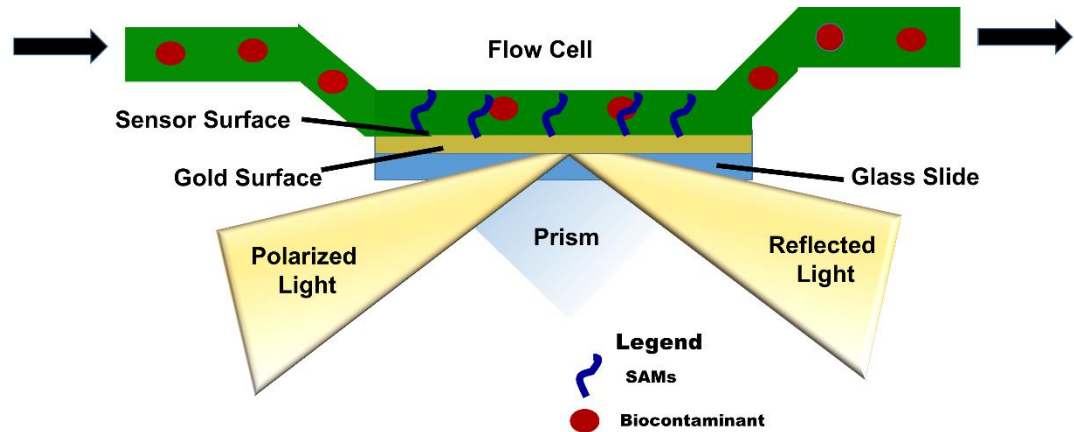


**Figure 1.3.** Schematic diagram of surface plasmon resonance flow cell when a light source passes through a prism and strikes the surface of the flow cell at an angle of total internal reflection, where the interactions of the surface of the gold sensor reduce the intensity of the light beam to generate a response signal in the reflected light.

### 1.2.3. Interpreting Sensorgrams

The sensorgram holds a great deal of information about reaction rates, kinetics, and amount of material bound or unbound to the surface of the sample being analyzed. This review will focus on the amount of material adhered to the surface. Detailed explanations on how to analyze sensorgrams to obtain kinetic and binding rates can be found in the

literature.<sup>49,51</sup> A schematic illustration of a labeled sensorgram is found in Figure 1.4. When determining the amount of analyte attached to the surface, a baseline reading of the solution or buffer should be established to indicate the absence of analyte bound to the surface, which is represented by the gray line. Once a base line reading is obtained, the analyte is injected onto the surface at a desired flow rate, which is represented by the blue line. As noted in the sensorgram, an increase in response units (RU) is observed indicating association with the analyte. The system then reaches a steady state where equal exchange of molecules occurs with the surface (red line). Once the injection is complete, a change in the refractive index is observed, (i.e., inflection in the sensorgram) and is represented by the black line. During this time, the solution or buffer continues to flow over the surface and can remove any analyte unbound to the surface, also known as disassociation (green line). The change in response units ( $\Delta$ RU) can then be determined by subtracting the final RU from the initial RU to obtain the amount of material interacting and binding to the surface (purple line).

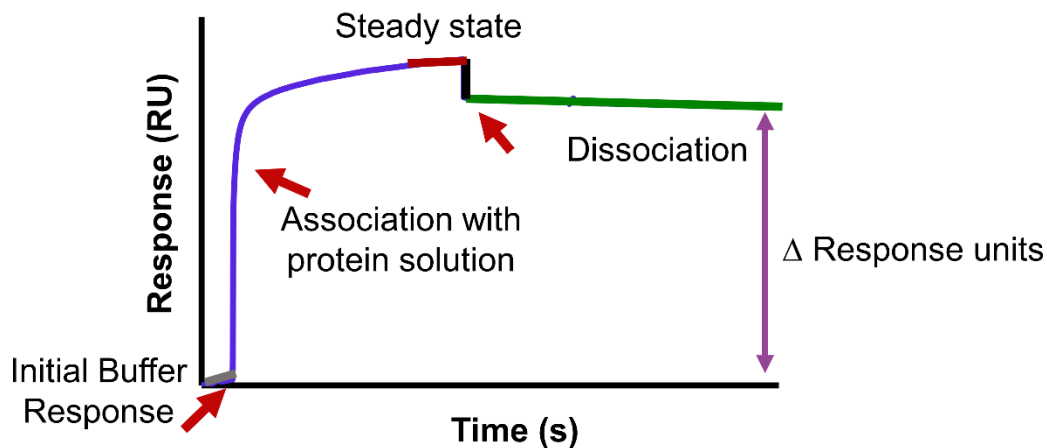


**Figure 1.4.** Diagram of sensorgram for SPR measurements including initial buffer response (gray line), association with the protein solution (blue line), saturation at the steady state (red line), and dissociation (green line). The change in response units ( $\Delta$ RU)

are determined by subtracting the response units after dissociation from the initial buffer response indicated by the purple line.

#### **1.2.4. Surface Plasmon Resonance Spectroscopy for *In Situ* Protein Interactions**

Many studies have employed surface plasmon resonance (SPR) spectroscopy to provide *in situ* monitoring of the interaction of biological materials with SAMs. Many studies have determined anti-fouling characteristics of poly(ethylene glycol) coated SAMs with varying degrees of length and materials by employing the *in situ* monitoring technique.<sup>14,16,36,41,63–65</sup> Similarly, PEG-based surfaces exhibiting amphiphilic nature were monitored for not only protein, but also cell adhesion using SPR techniques.<sup>22</sup> Additionally, ultra-low fouling of various zwitterionic coatings was monitored to determine how modification of the zwitterion altered the protein resistance of the surfaces.<sup>6,42–45,66</sup> SAMs composed of mixed hydrophobic and hydrophilic interfaces have also been monitored with SPR to systematically investigate the protein resistance capabilities of the surfaces.<sup>40,67</sup> Another study investigated how the SAM's stereochemistry affected cell adhesion.<sup>68</sup>

SPR is not only used to monitor the protein resistance of modified SAMs surfaces but can be used to monitor the conjugation of materials onto SAM-modified surfaces.<sup>69</sup> Several studies have investigated the adhesion of biomolecules to patterned surfaces.<sup>70,71</sup> Other studies employed this technique to determine the effect of nanoparticles conjugated to the surface of a SAM with respect to protein adhesion.<sup>72</sup> Lastly, investigations to determine the effect of increased mobilization of materials onto SAMs were also completed using the *in situ* monitoring of SPR.<sup>73–75</sup>

### **1.3. Quartz Crystal Microbalance**

#### **1.3.1. Basic Principles of Quartz Crystal Microbalance**

Advancements in scientific instrumentation generated a great interest in the use of microbalances to investigate physical and chemical processes associated with mass changes. Initially, electrochemical quartz crystal microbalances were used in experiments to measure mass changes during the electrodeposition of metals to an electrode surface.<sup>76</sup> The increased ability to employ this system to measure small mass changes involving thin films, including monolayer and submonolayer films, lead to the differentiation of electrochemical quartz crystal microbalance (eQCM) and quartz crystal microbalance (QCM) for electrochemical and nonelectrochemical applications utilizing QCM technology, respectively.

The QCM technology employs the principle of the piezoelectric effect, where mechanical stress, if applied to the surface of a quartz or other piezoelectric material, generates an electrical potential across the crystal proportional in magnitude to the applied stress. A schematic representation of the piezoelectric effect for shear motion as the electric field induces reorganization of the dipoles of the piezoelectric material, producing an elastic lattice strain and deformation of the material is found in Figure 1.5. The elastic nature of the strain and deformation generates an identical strain in the opposite polarity, resulting in an alternating potential across the surface of the crystal. This causes a vibrational movement in the crystal which produces an amplitude parallel to the surface. The vibrational motion establishes a transverse acoustic wave producing a standing wave. The frequency of the standing wave is denoted as the resonant frequency of the crystal. The quartz crystal must be cut from a specific orientation of the crystal axes. Literature

should be referenced for additional and more detailed explanation of piezoelectric effect as applied to QCM theory and application.<sup>76–82</sup>

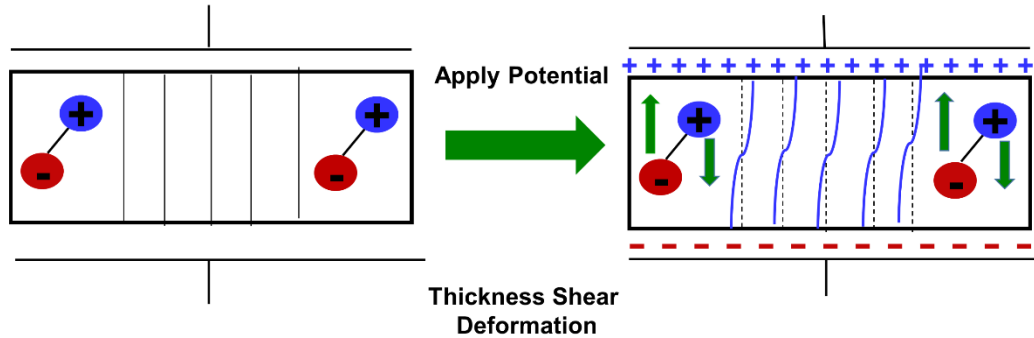


**Figure 1.5.** Schematic diagram of a shear wave modulus with applied voltage causes reorganization of the dipoles producing strain resulting in an alternating potential across the surface of the crystal and generating a standing wave.

Many of the QCM sensors use the AT-cut which has a low temperature coefficient at room temperature resulting in minimal changes of frequency, compared to the BT- or SC (stress-compensated)-cut. The thickness of the crystal wafer, chemical structure, and shape determine the fundamental frequency. Higher frequency crystals have more sensitivity but are much thinner and, consequently, more fragile. The alternate option is a lower frequency at an odd harmonic. The two most common harmonics are 5 MHz and 10 MHz with 15 MHz being the practical limit. Once an electric current near the frequency of the crystal is applied, the resonant frequency can be determined. Treating the mass deposited as an extension of the total mass of the crystal, electrodes, or any material on the surface, Sauerbrey was able to derive the relationship between the change in frequency ( $\Delta f$ ) to the change in mass ( $\Delta m$ ) for the QCM as found in Equation 1.2.<sup>83</sup>

$$\Delta f = -\frac{2f_0^2}{A\sqrt{\rho_q \mu_q}} \Delta m \quad (1.2)$$

Where  $\Delta f$  is the observed change in frequency, in Hz,  $f_0$  is the resonant frequency, in Hz,  $\Delta m$  is the change in mass, in grams,  $A$  is the area of the active crystal between the electrodes, in  $\text{cm}^2$ ,  $\rho_q$  is the density of the quartz ( $2.348 \text{ g} \cdot \text{cm}^{-3}$ ), and  $\mu_q$  is the shear modulus of the AT-cut quartz ( $2.947 \times 10^{11} \text{ g} \cdot \text{cm}^{-1} \cdot \text{s}^{-2}$ ). Equation 1.2 can be reduced to Equation 1.3, by using the calibration constant,  $C_f$ , which is also known as the sensitivity factor.

$$\Delta f = -C_f \Delta m \quad (1.3)$$

Where  $C_f$  is  $56.6 \text{ Hz cm}^2 \mu\text{g}^{-1}$  for a 5 MHz crystal, and  $226 \text{ Hz cm}^2 \mu\text{g}^{-1}$  for a 10 MHz crystal. The addition of metal electrodes on either side of the crystal disk allows for the oscillation of the electric field, producing a resonant frequency. Deposition of a thin film on the surface of the electrode further decreases the frequency and is directly proportional to the mass deposited using the Sauerbrey Equation (Equation 1.2). The equation is limited to oscillation in air for rigid masses attached to the surface of the crystal. Additional studies have shown that QCM can be performed with *in situ* measurements in liquid to probe viscoelastic properties and interactions with modification to the Sauerbrey equation by Kanazawa and Gordan to include the viscosity, found in Equation 1.4.<sup>84</sup>

$$\Delta f = -f_0^3 \left( \frac{\eta_l \rho_l}{\pi \rho_q \mu_q} \right)^{1/2} \quad (1.4)$$

Where  $\Delta f$  is the change in frequency, in Hz,  $f_0$  is the resonant frequency, in Hz,  $\eta_l$  is the viscosity of the liquid,  $\rho_l$  is the density of the liquid,  $\rho_q$  is the density of the quartz ( $2.348 \text{ g} \cdot \text{cm}^{-3}$ ), and  $\mu_q$  is the shear modulus of the AT-cut quartz ( $2.947 \times 10^{11} \text{ g} \cdot \text{cm}^{-1} \cdot \text{s}^{-2}$ ).

### 1.3.2. Types of Measurements for Quartz Crystal Microbalance

When acting as a microbalance, the QCM is able to perform gravimetric analysis to determine the mass loading of the crystal. Gravimetric analysis is the most common use of the QCM. It's important to note that any material with mass can generate a response in the QCM to cause a change in frequency. The use of thiol based SAMs, which can be chemically tailored to interact with specific proteins or binding materials, is leading the way into more specific understanding of mass loading of the electrode surface. Furthermore, the sensitivity of the QCM is defined by the electrode surface, and more completely, the area of the crystal sandwiched between the electrode plates. The amplitude is maximum in the center of the QCM and decays as a Gaussian distribution that is a function of radial distance. It is imperative to know the surface size of the QCM surface electrodes to determine the accurate mass loading of the electrode surface.

Alternately, the QCM has the ability to provide information about the viscoelastic properties of thin films. A simplistic means to detect changes in viscoelastic properties is to monitor the resonance resistance ( $R$ ) of the quartz crystal during the experiment. These experiments can be difficult due to the fact that the shear wave exists within the quartz crystal. The dissipation technique, often noted as QCM-D, drives the crystal voltage at resonant frequency using an oscillator with the ability to be intermittently disconnect, resulting in the exponential decay of the amplitude across the crystal. Using the recorded decay curve, and the absolute Q-factor, which is inversely proportional to  $R$ , the frequency of the oscillator can be determined. QCM-D measurements allow for *in situ* monitoring of mass loading.

### 1.3.3. Quartz Crystal Microbalance Experimental Setup

In a QCM experiment, it is necessary to have a data processor and software, a resonator, an electrode sample holder, and a QCM sensor, as illustrated in Figure 1.6. The QCM sensor consists of typically an AT-cut quartz crystal having a thin layer of Ti or Cr on which usually gold is subsequently deposited to about 1000Å. The sensor is exposed to the material, and the resonator and ultimately the data processor depicts the new resonant frequency of the sensor.

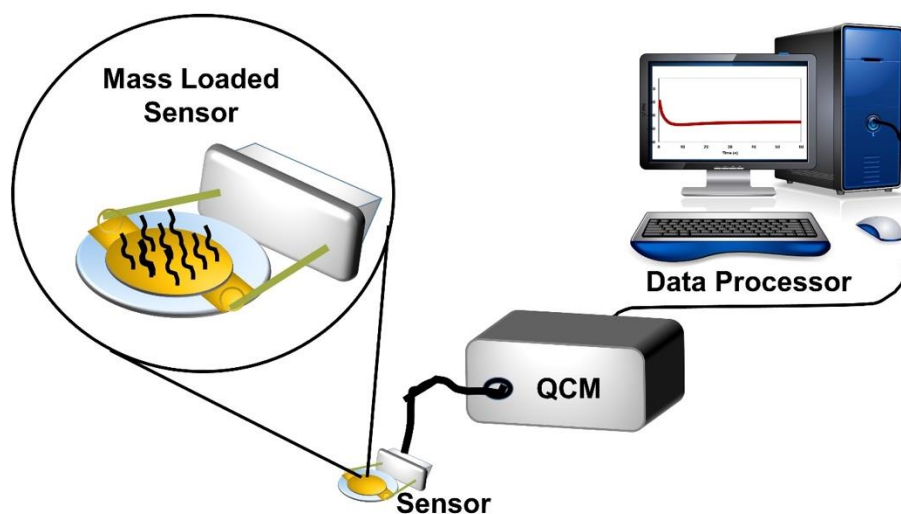


**Figure 1.6.** Schematic illustration of the QCM setup depicting changes in the frequency signal of the oscillating sensor when mass changes occurs for different layers.

### 1.3.4. Quartz Crystal Microbalance Measurements

In the case of *ex situ* experimentation, the resonant frequency of the QCM sensor is recorded. The QCM sensor is then exposed to the SAM solution to generate a well-ordered SAM, then the resonant frequency is measured again. If additional investigation of the SAM with proteins, cells, or other analytes is desired, the exposure to the material takes place, then a third measurement of the frequency is recorded. The change in frequency ( $\Delta f$ ) is then related to the change in mass ( $\Delta m$ ) using Equation 1.3.

The QCM-D allows for *in situ* nanoscale techniques that monitor real-time changes in frequency and in dissipation of a freely oscillating sensor. The dissipation value is determined from the time it takes for the oscillation to stop once the voltage is stopped. The softer the material, the more dampening is observed in the dissipation value. The dissipation value is calculated using Equation 1.5.

$$D = \frac{E_{lost}}{2\pi E_{stored}} \quad (1.5)$$

Where D is the dissipation,  $E_{lost}$  is the energy lost during the oscillation of one cycle, and  $E_{stored}$  is the energy stored. This technique offers the ability to investigate the materials hardness or rigidity by jumping between the fundamental frequency and overtones. Applying the information to viscoelastic models, additional information about the viscoelastic properties can be identified. Understanding the properties of the material, allows for the determination of change in frequency and application of the Sauerbrey equation, or the modified version allows for the determination of the mass loading of material on the sensor surface.

### **1.3.5. Quartz Crystal Microbalance Utilized to Monitor Protein Interactions**

QCM systems are routinely used to obtain information about protein adsorption/desorption, cell adhesion, protein-protein interactions, degradation of polymers, biofouling or biofilm formation, and changes involving self-assembled monolayers.<sup>85-90</sup> The QCM system has been used to monitor both *in situ* and *ex situ* adsorption of proteins to the surface of a SAM.<sup>85-88,91</sup> The interaction of protein adsorption with modified SAMs to determine protein resistance has also been monitored using QCM.<sup>89,90,92</sup> Additionally, modified SAMs with specific binding sites can be monitored for controlled loading of material onto

the SAMs surface.<sup>93–95</sup> The sensitivity of the QCM system allows for not only monitoring of adsorption to the surface, but it also lends to determining desorption<sup>96</sup> and surface structural modifications and interactions,<sup>97</sup> providing a great tool for understanding reaction kinetics and surface interactions.

## **1.4. Atomic Force Microscopy**

### **1.4.1. Basic Principles of Atomic Force Microscopy**

Atomic Force Microscopy (AFM) is part of a larger family of instruments known as Scanning Probe Microscopes (SPMs). SPMs allow for the investigation of surfaces using both imaging and surface characterization techniques in air or fluid, rather than in high vacuum. AFM improves upon Scanning Tunneling Microscopy (STM), by enabling high resolution, three-dimensional imaging of the sample surface that allows for detection of atomic scale features on a wide range of insulating materials, as compared to the STM which only has the ability to image conductive or semi-conductive samples. The SPM uses a very sharp probe to scan the surface and measure properties of the sample surface. Specifically, the AFM measures forces between the sharp probe and the surface of the sample, then generates a 3D profile at the nanoscale. The AFM tip, composed of a probe supported by a cantilever, gently touches the surface of the sample and records the force between the sample surface and the probe. Hook's law, found in Equation 1.6, is used to describe the force between the probe and the sample surface.

$$F = -k C_d \quad (1.6)$$

where  $F$  is the force,  $k$  is the spring constant, and  $C_d$  is the cantilever deflection. The interacting force is dependent on the distance of the probe to the surface. The force applied

to the surface is determined by the technique selected, desired information to be extracted from the surface of the sample, and the composition of sample surface.

The AFM can image in three modes: contact mode, intermittent contact mode, and non-contact mode. In the case of contact mode, the separation of the surface and the probe is less than 0.5 nm. The spring constant of the cantilever is a lower value, causing the cantilever to bend and the probe to experience repulsive forces. The force is constant between the tip and sample, allowing for faster scanning and friction analysis, but it also has stronger forces that can damage softer samples. Intermittent contact mode maintains a distance of 0.5–2.0 nm between the tip and sample. The probe contacts the surface with a "tapping" motion during the bottom of the swinging motion with the resonant frequency, while scanning the surface. This technique is preferred for softer surfaces such as thin films or biomaterials, since there is a decrease in the lateral forces resulting from shorter contact time with the surface. Non-contact mode images, with a distance of 0.1 to 10 nm, use attractive forces (van der Waals forces). As stated with the name non-contact, the probe does not touch the surface, rather, as it scans the surface, the probe oscillates above the surface. This method extends the lifetime of the probe tip due to lower forces but at the cost of lower resolution of images.

In addition to topography imaging, the AFM can provide amplitude and phase imaging. In amplitude imaging, the amplitude of the cantilever oscillation is adjusted to nearly constant to produce an image contrast from the complied error signal resulting from the required voltage needed to keep the amplitude constant. Phase imaging utilizes the difference in material properties to determine the phase lag difference between the driven oscillations and the measured oscillations. Phase imaging can provide qualification

information about differences with respect to composition, adhesion, and frictional properties. For additional details on basic theory and specifications of imaging, the reader is referred to additional literature resources.<sup>98-107</sup>

#### **1.4.2. Atomic Force Microscopy Experimental Setup**

The AFM is comprised of a probe, cantilever, scanner, laser, photodetector, and a data processor, as shown in Figure 1.7. The probe is attached to a flexible microcantilever, and deflections from the arm are monitored as the probe raster scans the surface of the sample. The deflections occur as the probe contacts topographical features of the surface, generating a high resolution, 3D image of the surface.

The probe is responsible for the force interaction with the surface and can be designed with different coatings and materials to meet the needs of the surface being imaged. Common probe tips are silicon or silicon nitride that range in size from 100-200  $\mu\text{m}$  long, 10-40  $\mu\text{m}$  wide, and 0.3-2  $\mu\text{m}$  thick. The top side of the cantilever is usually coated with a reflective coating. Typically, the probe tip and the cantilever are integrated together as one unit. The flexibility of the cantilever is dependent on the spring constant. The spring constant is dependent on the material, shape, and size of the cantilever, where shorter and thicker cantilevers have greater spring constants and higher frequencies.

A piezo-electric tube scanner controls movement of the probe tip in the  $x$ ,  $y$ , and  $z$  directions. The maximum range for imaging at one time is 100  $\mu\text{m}$  x 100  $\mu\text{m}$  in the  $x$ - $y$  plane and 5  $\mu\text{m}$  in the  $z$ -direction. The scanner moves across in a step fashion preset with a number of data points and retracing the same line in a return fashion before making a step perpendicular to continue with scan pattern. A laser light is positioned to reflect from the cantilever onto a photodetector, which is able to monitor any changes to the deflection of

the cantilever. The typical photodetector has 4 quadrants: A, B, C, and D. The deflection signal is calculated as a result of the difference in the detected signal from the A + B compared to the C + D quadrants. Lateral or torsional bending can be determined by comparison of signal strength between A + C and B + D. The deflections are then processed using a data processor or software to determine measurements of the samples.

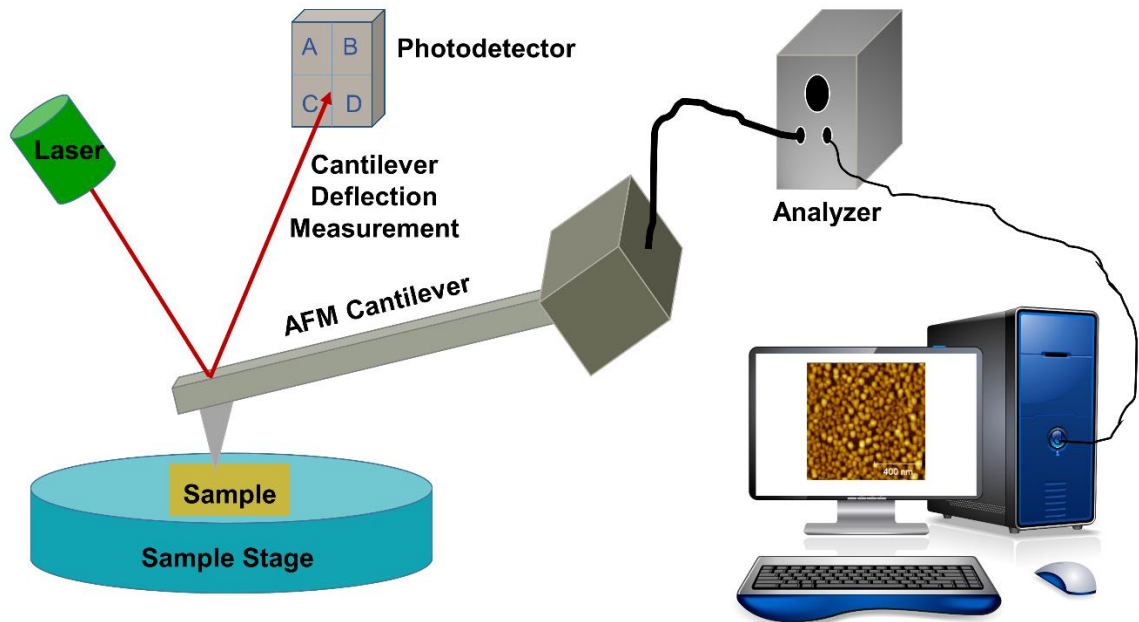


**Figure 1.7.** Schematic illustration of an atomic force microscope imaging a sample by analyzing the cantilevers deflections with a photodetector.

### 1.4.3. Atomic Force Microscopy Image Evaluation

Surface Topography is determined by surface measurements. Some of the more common measurements and calculations are discussed, but for additional measurements and explanation, literature should be reviewed.<sup>101,105,106,108,109</sup> Most data is processed using software, such as Gwyddion, to determine surface measurements, such as shape and roughness. The roughness can be characterized with height, wavelength and spacing parameters, that are referred to as roughness (R) and spacing (S) parameters. Height parameters are the most important parameters with respect to surface roughness. The most

widely used height parameter is roughness average ( $R_a$ ), since it is one of the easiest values to obtain compared to other height parameters. The roughness average can be obtained according to Equation 1.7,

$$R_a = \frac{1}{L} \int_0^L |Z(x)| dx \quad (1.7)$$

where  $R_a$  is the roughness average,  $L$  is the evaluation length of the sample,  $Z(x)$  is the height ( $Z$ ) and position ( $x$ ) of the sample. Since  $R_a$  is a mean absolute profile, a disadvantage lies in the average roughness measurement where it can be the same for multiple surfaces with different profiles. Additional parameters must be used to characterize the surface of the sample.

The root mean square (RMS or  $R_{rms}$ ) of roughness is another statistical measurement resulting from the square of the measurements. Equation 1.8 indicates that  $R_{rms}$  is similar to  $R_a$  with the exception being the mean squared absolute values of the surface roughness.

$$R_{rms} = \sqrt{\frac{1}{L} \int_0^L |Z^2(x)| dx} \quad (1.8)$$

The  $R_{rms}$  is dependent on the scan size and sweep area of the surface, but the squaring of the amplitude makes  $R_{rms}$  more sensitive to the peaks and valleys. Many software programs allow for the determination of maximum height ( $R_T$ ) and valley ( $R_V$ ). The maximum peak height profile ( $R_p$ ) is determined by the vertical distance between the highest peak and lowest valley. These values become helpful when trying to identify defects on the surface.

Roughness spacing parameters relate roughness to repetition or patterning of the surface. Peak count ( $P_c$ ), expressed in peaks/inch or peaks/cm analyzes the number of

peaks along a length that falls outside a determined upper and lower threshold. It is denoted as a bandwidth, and is illustrated in Figure 1.8. Only peaks that exceed the determined bandwidth and return are considered in the peak count. Once the peaks are identified, the peak density ( $P_D$ ) can be determined by evaluation of the number of peaks per unit area.

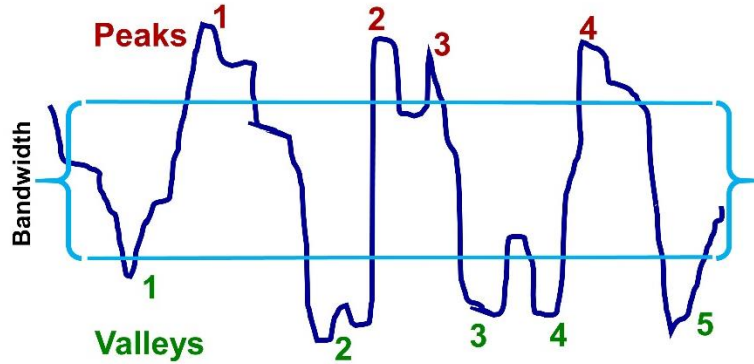


**Figure 1.8.** Schematic illustration of peak count determination by bandwidth.

To further evaluate the repetition of spacing parameters, the mean spacing ( $S_m$ ) can evaluate the average space (denoted in  $\mu\text{m}$  or  $\text{nm}$ ) between peaks over the length of evaluation and is determined using Equation 1.9,

$$S_m = \frac{1}{L} \sum_{i=1}^L S_i \quad (1.9)$$

where  $S_m$  is the mean spacing,  $L$  is the length of evaluation, and  $S_i$  is the average of the spacing individual. The average wavelength ( $\lambda_a$ ) and the RMS wavelength ( $\lambda_{\text{rms}}$ ) are similar to  $R_a$  and  $R_{\text{rms}}$  for the roughness parameters. In the case of average wavelength, the spacing between the peaks and the valleys are weighted by the individual frequencies and amplitudes and are calculated using Equations 1.10 and 1.11, respectively.

$$\lambda_a = \frac{R_a}{\Delta_a} \quad (1.10)$$

Where  $\lambda_a$  is the average wavelength,  $R_a$  is the average roughness, and  $\Delta_a$  is the mean slope of the profile of the evaluation length.

$$\lambda_{rms} = 2\pi \frac{R_{rms}}{\Delta_{rms}} \quad (1.11)$$

Where  $\lambda_{rms}$  is the average wavelength,  $R_{rms}$  is the average roughness, and  $\Delta_{rms}$  is the mean slope of the profile of the evaluation length.

The measurements identified herein are not an exhaustive list, but they are some of the more common measurement used to evaluate the surface of a sample. Additional resources should be explored for more in depth explanation and more advanced calculations regarding data processing of AFM imaging.<sup>110</sup>

#### **1.4.4. AFM Investigations to Probe Protein Adhesion**

Several advantages of the AFM, including the ability to image in air at room temperature and non-conductive surfaces, allows AFM imaging of biological samples to be possible. On a superficial level, AFM has been used to generate 3D topographical images of the surface characterized by identifying distinctions of the surfaces from the image.<sup>64,92,94</sup> Studies have also used the topographical imaging to monitor the various stages of surface modification with AFM<sup>66,74</sup> or monitoring surface patterning.<sup>70</sup> Studies have also employed AFM to probe protein adhesion over time.<sup>111</sup> Additional studies have monitored immobilization of materials on the surface of SAMs using the AFM.<sup>112,113</sup> Not only can the AFM image the surface, various software applications permit mathematical profiling of the surface spacing and height. Studies have routinely employed surface roughness and height profiling to characterize surface interactions and patterning of material adhered to the surface.<sup>114-116</sup>

## 1.5. Ellipsometry

### 1.5.1. Basic Principles of Ellipsometry

Ellipsometry is a light optical technique that is non-contact, non-destructive, which requires little to no sample preparation. Ellipsometry, in a universal sense, measures the change of the polarization state of an elliptical light upon interacting with a thin film allowing for the investigation of the dielectric properties of materials to characterize composition, roughness, and thickness of the thin film. When the polarized light interacts, (reflected, absorbed, scattered or transmitted) with the surface of the thin film, changes to the amplitude ( $\Psi$ ) and phase ( $\Delta$ ) of the electric field vectors parallel and perpendicular to the light beam are observed. The spatial directions parallel and perpendicular to the plane of incidence are denoted as p and s, respectively.

In ellipsometry, the two measured variables are the angles  $\Delta$  (Delta) and  $\Psi$  (PSI). The  $\Delta$  (Delta) variable is the difference in the phase between the p and s direction of the Fresnel reflection coefficient, denoted as  $R_s$  and  $R_p$ , with respect to a given wavelength and angle of incidence, and  $\Psi$  (PSI) is the measure of the absolute values of  $R_s$  and  $R_p$ . Since ellipsometry exploits the ratio of  $R_s$  and  $R_p$ , it is reproducible and exact ranging from sub-nanometer levels to several microns. It is important to note that only  $\Delta$  and  $\Psi$  are measured values and can be accurately and precisely determined from the fundamental equation of ellipsometry, see Equation 1.12.

$$\rho = \frac{R^P}{R^S} = \tan\Psi e^{i\Delta} \quad (1.12)$$

where  $\rho$  is defined as the ratio of the reflectivity of the p-polarized light ( $R^P$ ) and s-polarized light ( $R^S$ ). In this equation, rho ( $\rho$ ) is a complex reflectance ratio of a system:

$\tan \Psi$  is the magnitude of the reflectivity ratio, and  $i\Delta$  is the difference of phase shift and a complex number. Thorough theoretical details regarding Ellipsometric parameters can be found in the literature.<sup>117-121</sup>

To obtain quantitative information such as thickness, optical constants, refractive index, surface roughness, composition, crystallinity, uniformity, and anisotropy, a model based analysis that utilizes equations and "fit" parameters is necessary to describe the interaction of the light with the materials. Altering the model, or "fit" parameter, can alter the obtained values; therefore, the calculated values are model dependent. Measurements are taken with the assumption that the samples are composed of a small number of well-defined, discrete layers that are optically homogeneous. Ellipsometry techniques have advanced in spectral resolution to now include measurements taken over a thousand wavelengths in fractions of a second, as highlighted in the following section. Furthermore, as more wavelength ranges become available, new applications and better modeling techniques will give additional insight into surface interactions at the solid/liquid interface. Additional and more detailed information about ellipsometry, the calculated thickness values, and the model or "fit" parameters can be found in the literature.<sup>122</sup>

### **1.5.2. Types of Ellipsometry**

There are several ellipsometry designs in current use; two common types are null ellipsometry and spectroscopic ellipsometry. Null ellipsometry employs a monochromatic light source, which is usually a laser in the visible spectra region, such as a HeNe laser with a wavelength of 632.8 nm. The single wavelength laser allows for a small focused spot on the sample surface, and the lasers can be higher in power compared to a broad band source. It is important to note that with the single wavelength system, the output is restricted to one

set of values for amplitude ( $\Psi$ ) and phase ( $\Delta$ ). Spectroscopic ellipsometry (SE) in comparison employs a broad-spectrum light source with a particular spectral region, such as infrared, visible, or ultra-violet. SE acquires  $\Psi$  and  $\Delta$  values as a function of each wavelength, greatly increasing the data set obtained in the measurements, and requiring an optical model to be built to fit the data and extract the quantitative properties of the film. Also, SE allows for *in situ* monitoring of film deposition and growth by tracking the complex index of refraction with time. The ability of *in situ* monitoring enables real time analysis that can provide new information of surface interactions. SE can obtain sample mapping, which tracks measurements of the surface, generating an image of the surface.

### **1.5.3. Ellipsometry Experimental Setup**

There are 5 main elements for any ellipsometer: a light source, polarization state generator (PSG), a sample, polarization state analyzer (PSA), and a light detector illustrated in Figure 1.9. The PSG often includes a light source, polarizer, and a phase inducer, such as a quarter-wave plate, compensator, or a phase modulator. The PSA often includes a phase inducer, polarizer (analyzer), and detector. Both the PSG and PSA are optical instruments that contain elements that alter the polarization state of the light as it passes through. In simplistic terms, this technique has a sample placed on the stage, and then a light source emits electromagnetic radiation that passes through a polarizer, to become linearly polarized, and passes through a compensator to irradiate the sample. Upon reflection, the emitted radiation passes through a compensator, then an analyzer to reach the detector.

As shown in a schematic diagram in Figure 1.9, the incident and reflection beams traverse the plane of incidence, where  $\phi$  represents the angle of incidence. The polarization state of the light interacting with the sample can be broken down into the s and p components, where s oscillates perpendicular to the plane of incidence, and parallel to the sample surface, while p oscillates parallel to the plane of incidence, and perpendicular to the sample surface. The  $R^S$  and  $R^P$  values, Equation 1.12, are determined from the amplitude of the s and p components after reflection and normalization to the initial value. The  $R^S$  and  $R^P$  values can then be used to find the complex reflectance ratio.

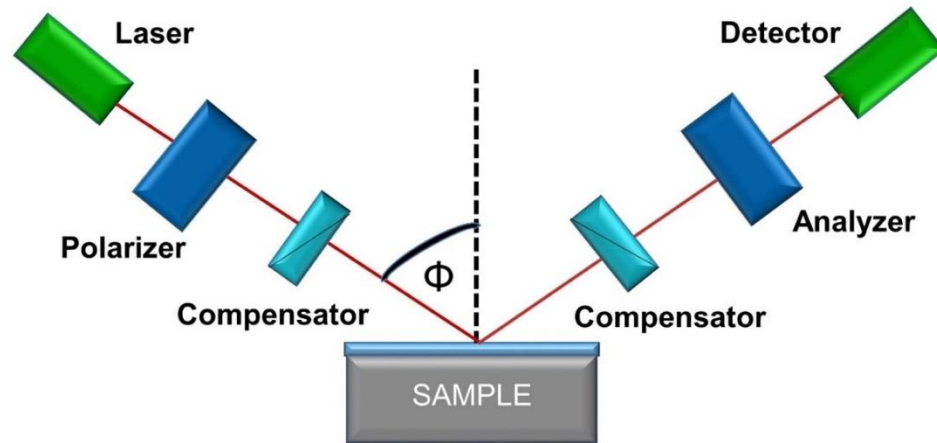


**Figure 1.9.** Schematic diagram illustrating polarized light reflecting from a sample surface and the change in polarization is analyzed for a typical ellipsometry setup,  $\phi$  is the angle of incidence.

#### 1.5.4. Ellipsometric Measurements

Both single-wavelength and SE have been utilized to determine the thickness of thin films, both *in situ* and *ex situ*. In the field of biomaterials, ellipsometry enables the characterization of biofunctional layers that may be optically homogeneous, isotropic, but have a significant change of refractive index at the interface. While *in situ* studies allow

for monitoring film growth in a dynamic environment with the surface, *ex situ* studies merely analyze the change in film thickness during each phase of the surface layers.

### **1.5.5. Monitoring Biofilm Formation with Ellipsometry**

Ellipsometry is a common technique used to characterize the thickness of thin film coatings. Various studies have utilized single wavelength or SE in an *ex situ* or *in situ* capacity in order to gain a better understanding of surface interactions with biologics. For example, *in situ* monitoring has been used to analyze the absorption and removal of biomolecules on a patterned surface generated from self- assembled monolayers using a custom-built single wavelength ellipsometer.<sup>70,71</sup> In this study, the addition of layers of azurin, a blue copper protein, to bare gold was monitored using *in situ* SE and compared to a hexadecanethiol SAM on a gold substrate. The data was fitted to various models to check for accuracy of fitting techniques in monitoring the properties of the protein.<sup>123</sup> *In situ* SE has also been used to evaluate surface chemistry induced cellular responses with respect to SAMs on gold substrates. For example, a study modified SAMs with amino and carboxy termini to monitor the response of Adipose-derived stromal cells to the surface and evaluate the changes to the conformation and orientation of the adhered protein.<sup>124</sup> Another study investigated the ligand binding to SAMs fabricated using aminopropyltriethoxysilane and mixed silanes that are known to bind to human serum albumin. In attempts to understand the solid/water interface, *in situ* SE studies have been used to study the adsorption of proteins on various hydrophobic and hydrophilic SAMs.<sup>92</sup>

In comparison, *ex situ* studies using single wavelength ellipsometry have investigated functionalized SAMs and their interaction with proteins to minimize protein adsorption,<sup>125</sup> and to control protein immobilization and stability.<sup>112</sup> Other studies have

included *ex situ* techniques with SE to determine the attachment and adsorption at the solid/liquid interface of Bovine Serum Albumin (BSA) to functionalized SAMs.<sup>91</sup> The investigation of varying lengths of ethylene glycol repeated patterned SAMs terminated with CF<sub>3</sub> were performed to analyze the relative thickness of protein adsorption.<sup>126</sup> Multiple studies have employed an ellipsometric technique with either an *in situ* or *ex situ* means to aid in understanding biological interactions with SAMs and to monitor layering of material on the surface of the SAMs. The information obtained from the aforementioned studies allow for a better understanding of surface interactions and subsequently allow for the design of optimal surfaces for specific applications.

## **1.6. X-Ray Photoelectron Spectroscopy**

### **1.6.1. Basic Principles of X-Ray Photoelectron Spectroscopy**

X-ray photoelectron spectroscopy (XPS), also known as electron spectroscopy for chemical analysis (ESCA), is a surface sensitive, limited to the first 10 nm of the surface, qualitative and quantitative technique that provides the elemental composition of a surface, with the exception of hydrogen and helium. The peaks observed in an XPS spectrum can also reflect the electronic structure or chemical state of the sample. The local bonding environment is affected by oxidation state, neighboring atoms, bonding hybridization to neighboring atoms, and even bonding hybridization between neighboring atoms. Furthermore, the oxidation state of the elements detected by XPS can also be obtained to yield useful information about their chemical environments. Accordingly, analysis by XPS can provide information about the surface's chemistry, electronic structure, organization, and with ion etching depth profiling can be achieved.

The phenomenon for which XPS is based on is the photoelectric effect, where a photon of light transfers its energy to the electrons in an atom, causing core-level electrons to be emitted with no loss of energy. Photoelectron emissions can only be observed once the intensity of the irradiated light exceeds the energy threshold of the electron at the energy level of the atom and is proportional to the number of electrons emitted.<sup>127</sup> The kinetic energy of the emitted electrons is linearly proportional to the frequency of the exciting photons, and can be described by the Einstein equation, Equation 1.13.

$$E_B = h\nu - (\text{KE} + \phi) \quad (1.13)$$

Where  $E_B$  is the binding energy of the electron in the atom,  $h\nu$  is the known value for the X-ray source used (for example, Al  $K_\alpha$  X-ray,  $h\nu = 1486.7$  eV), KE is the kinetic energy of the emitted electron measured by the instrument, and  $\phi$  is the work function, dependent on the instrument and material. The work function is a correction factor that considers the kinetic energy lost (although only a few eV) by the emitted electron as it is absorbed by the analyzer and detector.

In order to determine the identity, the oxidation state, as well as the environment of the elements present on a surface, the binding energy of the emitted electrons require a deeper understanding. Each emitted electron exhibits a unique binding energy that is dependent on initial and final state effects. The local bonding environment results in chemical shifts, which are subtle reproducible shifts in the binding energy of the emitted photoelectrons as a result of the environment that provides the electronic structure information. Since each element contains a unique set of binding energies, the chemical composition of the sample can be determined.<sup>128,129</sup> Detailed theoretical background on the principles of XPS can be found in the literature.<sup>127,130–135</sup> Tabulated binding energies

to aid in the identification of XPS peaks can be found in various sources.<sup>128,129</sup> Since the analyzer can determine the number of electrons for each energy value, quantitative analysis can be performed on acquired data.

### **1.6.2. Experimental Setup**

The main components of the XPS are the vacuum system, X-ray source, electron energy analyzer, and a data system, shown in Figure 1.10. Most XPS measurements are performed under high vacuum ( $P \sim 10^{-8}$  millibar) or ultra-high vacuum ( $P < 10^{-9}$  millibar) environmental conditions. The sample surface is then irradiated with a photon source in the X-ray energy range. Many commercial XPS instruments use a focused monochromatic Al  $K_{\alpha}$  or a polychromatic Al or Mg  $K_{\alpha}$  X-ray source. After the energy from the photon source is transferred to the electrons of the irradiated atoms, core-level photoelectrons are emitted. The photoelectrons close to the surface are able to escape into the vacuum chamber, where the photoelectrons can reach the analyzer. The analyzer -- consisting of a collection lens, energy analyzer, and a detector -- determines the energy and counts the electrons. The entire system is controlled by a data system, which also processes the data to generate a spectrum. Literature should be referenced for a more detailed technical description of the XPS setup.<sup>134,136</sup>

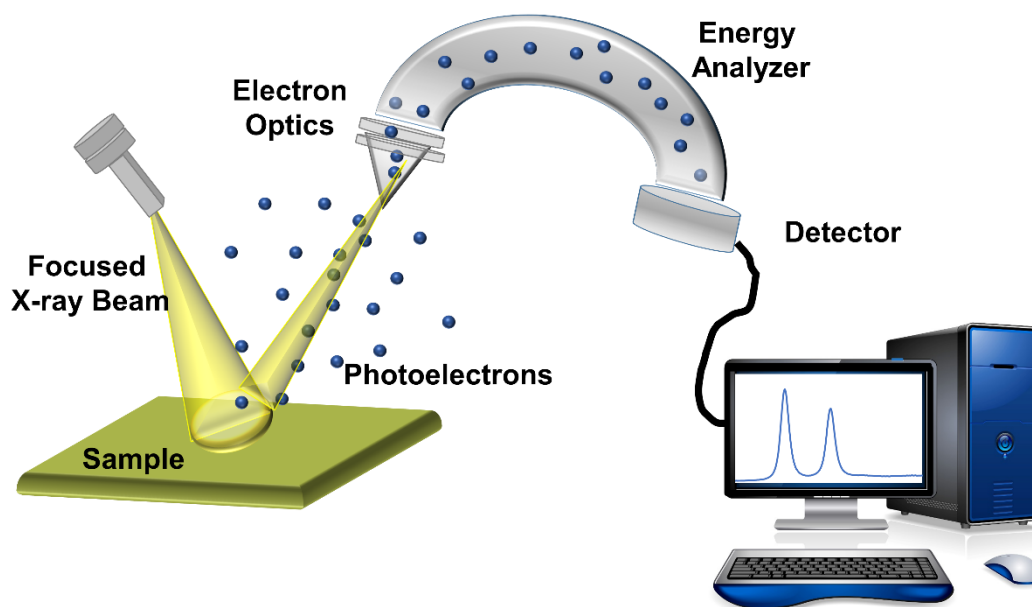


**Figure 1.10.** Schematic illustration depicting an irradiated sample surface that emitted photoelectrons that are collected and analyzed by an x-ray photoelectron spectrometer.

### 1.6.3. Chemical Analysis of Protein Absorption using XPS

With respect to analytical surface characterization techniques, XPS is the most widely used and is continuing to increase in popularity for surface chemical analysis. Several studies analyzing protein absorption onto SAM surfaces employ XPS to monitor the N 1s peak. It is important to note that this type of analysis is often performed on nitrogen-free SAMs, or SAMs where the nitrogen species is chemically distinct from the analyzed biologic and as a representative example, Figure 1.11 illustrates the N 1s peak at 400 eV for a sample that was exposed to a protein and monitored using XPS. The relative intensities can be used to determine the amount of protein on the surface of the sample.

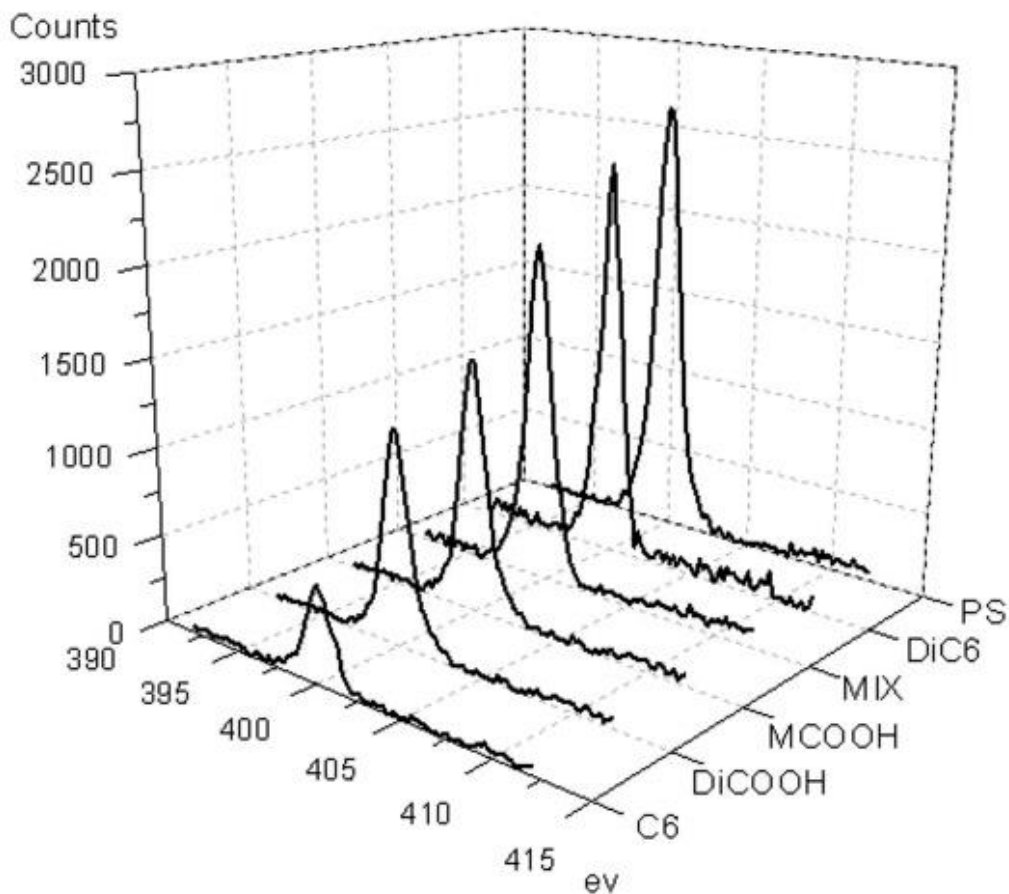


**Figure 1.11.** XPS spectra in the N 1s region for surfaces exposed to protein. Adapted with permission from Reference 76. Copyright 2009 American Chemical Society.<sup>137</sup>

Many studies have incorporated XPS to determine the amount of protein adhered to the surface of modified SAMs to evaluate the anti-fouling or protein resistance properties of the SAMs.<sup>23,92,95</sup> In one study, zwitterionic-based SAMs, containing two oppositely charged thiols terminated with a triethylammonium or a sulfonate group, were tested to determine the fouling and release of proteins to the SAMs surface.<sup>46</sup> Similarly, an amphiphilic homopolymer, synthesized from a monomer bearing hydrophilic and hydrophobic functionalities, was analyzed with XPS to determine protein resistant areas.<sup>137</sup> The anti-fouling performance, compositional heterogeneity, and phase segregation of

mixed surfaces such as amphiphilic polymers<sup>21</sup> and binary SAMs generated from mixtures of alkanethiols and benzyl thiols,<sup>42</sup> hydroxyl-terminated,<sup>23,92,95</sup> amino-terminated,<sup>23,92</sup> and perfluoro-terminated alkanethiols<sup>23,92</sup> have also been determined by XPS.

Moreover, XPS can be used to monitor the adsorption and release of proteins on SAM-modified biosensors. For example, XPS was used to monitor the surface composition of a biosensor bearing immobilized biorecognition sites.<sup>75</sup> Mixed monolayers containing short-chained hydroxyl-terminated alkanethiols with *N*-hydroxysuccinimide-terminated crosslinkers were monitored to determine protein binding density and direct protein immobilization on biosensors by XPS.<sup>74</sup> The surface modification of carboxymethylated dextrane modified *N*-heterocyclic carbene thiol SAMs<sup>36</sup> employed XPS to determine the amount of proteins on the biosensors. XPS has also been used to evaluate how the interface of a SAM -- -COOH, -OH, -CH<sub>3</sub>, and -NH<sub>2</sub> terminated -- can induce cellular response.<sup>124</sup>

### **1.7. Synergistic Instrumentation**

The complexity of the interactions between the SAMs on the substrate surface and the protein require multiple analytical techniques to ensure maximum understanding of the interactions that are achieved. Many studies integrate the use of several techniques to monitor substrate-analyte interactions. Currently, research and instrumentation are utilizing synergistic analysis, where the merging of multiple techniques for analysis into one experimental setup to monitor the interactions on the same surface may provide a more complete analysis with complementary techniques. Synergistic instrumentation might include the ability to investigate QCM and ellipsometry measurements simultaneously, or SPR spectroscopy and ellipsometry evaluations together.

### **1.7.1. Types of Synergistic Instrumentation**

In the case of the Q-Sense Explorer System, both QCM-D and ellipsometric analysis are merged to allow for simultaneous *in situ* measurements under a temperature controlled environment. In addition, the Q-Sense quartz crystal microbalance (E-series) is able to be combined with a J. A. Woollam Alpha SE ellipsometer in synergistic studies to allow for simultaneous *in situ* ellipsometric studies and QCM-D measurements. Biolin Scientific produces the Q-Sense QCM which is a single flow channel that is connected directly to the liquid handling system. In addition to being combined with ellipsometers to obtain ellipsometric thickness, this QCM is able to be combined with an electrochemical module to perform electrochemical studies with the QCM analysis, making a versatile instrument for synergistic investigations.

Bionavis has produced the MP-SPR Navis which combines ellipsometry and Multi-Parametric Surface Plasmon Resonance (MP-SPR) with the ability to determine refractive index or thickness of a surface. This instrument contains a 2-channel system for easy referencing of samples. The MP-SPR can also be combined to perform electrochemical measurements to obtain changes and interactions at different potentials, pH, and temperatures. Another instrument, the FilmTEK 2000, is a benchtop system that combines spectroscopic ellipsometry, multi-angle polarized spectroscopy, and intuitive material modeling. Other variations from FilmTEK employ the ability to generate 2D and 3D mapping of the material.

### **1.7.2. Synergistic Analysis In Complementary Techniques**

Many studies have employed the use of synergistic analysis in complementary techniques to obtain a deeper collective understanding of surface interactions at the

interface. One such study designed a specialized cell allowing the combination of imaging ellipsometry and surface plasmon resonance to obtain highly sensitive kinetic measurements of biomolecular interactions.<sup>138</sup> This synergistic study allowed for the analysis of adsorption and desorption of biomolecules on the gold surface.<sup>138</sup> Additionally, combining ellipsometry with the conditions of total internal reflection, generates simulations that produce greater sensitivity over traditional ellipsometry for protein-surface interactions and corrosion.<sup>60</sup>

Other studies have incorporated the quartz crystal microbalance dissipation technique with surface plasmon resonance measurements to obtain additional information not obtained with one technique alone.<sup>139</sup> In such a study, both techniques simultaneously generated three independent quantities yielding kinetic information, the number of molecules for a given unit and time, the fraction of mass associated with water coupling to the surface, and the mass of the protein that interacted with the sample surface. This information allows for the building of a better model of surface interactions.<sup>139</sup>

The synergistic analysis of surface interactions is a trend that can be expected to continue for the foreseeable future. The combined information provides a more complete understanding of the interactions between the thin film (SAM) and the protein (analytes). Other studies will benefit from the synergistic combination of analytical techniques to understand the interactions at the interface. New doors for integration and combination of techniques will continue as researchers push the boundaries of surface-analyte interactions.

## **1.8. Conclusions**

In this chapter, the methodologies with respect to biofilm formation, quantitative and qualitative, were reviewed for various analytical techniques. These techniques allow for

probing the surface interaction with various biocontaminates to allow for the study of the interactions between the substrate or the thin film (SAM) and the proteins that lead to generate the biofilm. A summary of each technique measurement contributions to the surface protein interaction are listed below.

- **SPR** provides a means to investigate *in situ* material interactions with the surface to determine the amount of material adhered to the surface by measuring the change in the angle of reflection.
- **QCM** determines the change in frequency resulting from the piezoelectric effect, and correlates the change in frequency to the mass loading of the quartz crystal.
- **AFM** generates a 3D topographical image of a surface by measuring the force interactions of the probe with the sample surface. The surface topography is determined by various measurements to determine roughness and spacing of the material on the surface.
- **Ellipsometry** allows for monitoring of material thickness by measuring the change in polarization of the light as it interacts with the material.
- **XPS** instrumentation probes the first 10 nm of the surface to determine the elemental composition of the surface, electronic structure, and organization.

In order to prevent biofilm formation, scientists must have the greatest understanding of how the proteins interact with surfaces of interest. Using various instrumental techniques to monitor and gather information about the interactions generates a broader knowledge base. Advantages of using instrumentation that can test multiple parameters on the same surface are of great value and can result in less error, quicker sample preparation, along with decreased resources. The knowledge obtained from these interactions lends to

better propagation of anti-fouling coatings that have the ability to limit biofilm formation when applied to various surfaces in wet environments, which not only add protection but increase longevity of products.

### 1.9. References

- (1) Pavithra, D.; Doble, M. Biofilm Formation, Bacterial Adhesion and Host Response on Polymeric Implants - Issues and Prevention. *Biomed. Mater.* **2008**, *3*, 34003–34015.
- (2) Donlan, R. M. Biofilm Formation: A Clinically Relevant Microbiological Process. *Clin. Infect. Dis.* **2002**, *33*, 1387–1392.
- (3) Cole, N.; Hume, E. B. H.; Vijay, A. K.; Sankaridurg, P.; Kumar, N.; Willcox, M. D. P. In Vivo Performance of Melimine as an Antimicrobial Coating for Contact Lenses in Models of CLARE and CLPU. *Investig. Ophthalmol. Vis. Sci.* **2010**, *51*, 390–395.
- (4) Willcox, M. D. P.; Hume, E. B. H.; Aliwarga, Y.; Kumar, N.; Cole, N. A Novel Cationic-Peptide Coating for the Prevention of Microbial Colonization on Contact Lenses. *J. Appl. Microbiol.* **2008**, *105*, 1817–1825.
- (5) Yao, Y.; Ohko, Y.; Sekiguchi, Y.; Fujishima, A.; Kubota, Y. Self-Sterilization Using Silicone Catheters Coated with Ag and TiO<sub>2</sub> Nanocomposite Thin Film. *J. Biomed. Mater. Res. - Part B Appl. Biomater.* **2008**, *85B*, 453–460.
- (6) Wang, Y. S.; Yau, S.; Chau, L. K.; Mohamed, A.; Huang, C. J. Functional Biointerfaces Based on Mixed Zwitterionic Self-Assembled Monolayers for Biosensing Application. *Langmuir* **2018**, *35*, 1652–1661.

- (7) Ishiyama, E. M.; Paterson, W. R.; Ian Wilson, D. Optimum Cleaning Cycles for Heat Transfer Equipment Undergoing Fouling and Ageing. *Chem. Eng. Sci.* **2011**, *66*, 604–612.
- (8) Liu, W.; Christian, G. K.; Zhang, Z.; Fryer, P. J. Direct Measurement of the Force Required to Disrupt and Remove Fouling Deposits of Whey Protein Concentrate. *Int. Dairy J.* **2006**, *16*, 164–172.
- (9) Flemming, H. C. Biofouling in Water Systems - Cases, Causes and Countermeasures. *Appl. Microbiol. Biotechnol.* **2002**, *59*, 629–640.
- (10) Hellio, C.; Yebra, D. Advances in Marine Antifouling Coatings and Technologies. In *Advances in Marine Antifouling Coatings and Technologies*; CRC Press LLC: Boca Raton, 2009.
- (11) Asuri, P.; Karajanagi, S. S.; Kane, R. S.; Dordick, J. S. Polymer-Nanotube-Enzyme Composites as Active Antifouling Films. *Small* **2007**, *3*, 50–53.
- (12) Chambers, L. D.; Stokes, K. R.; Walsh, F. C.; Wood, R. J. K. Modern Approaches to Marine Antifouling Coatings. *Surf. Coatings Technol.* **2006**, *201*, 3642–3652.
- (13) Cao, S.; Wang, J. D.; Chen, H. S.; Chen, D. R. Progress of Marine Biofouling and Antifouling Technologies. *Chinese Sci. Bull.* **2011**, *56*, 598–612.
- (14) Banerjee, I.; Pangule, R. C.; Kane, R. S. Antifouling Coatings: Recent Developments in the Design of Surfaces That Prevent Fouling by Proteins, Bacteria, and Marine Organisms. *Adv. Mater.* **2011**, *23*, 690–718.
- (15) Harding, J. L.; Reynolds, M. M. Combating Medical Device Fouling. *Trends*

- Biotechnol.* **2014**, *32*, 140–146.
- (16) Mrksich, M.; Whitesides, G. M. Using Self-Assembled Monolayers to Understand the Interactions of Man-Made Surfaces with Proteins and Cells. *Annu. Rev. Biophys. Biomol. Struct.* **2003**, *25*, 55–78.
- (17) Holmlin, R. E.; Chen, X.; Chapman, R. G.; Takayama, S.; Whitesides, G. M. Zwitterionic SAMs That Resist Nonspecific Adsorption of Protein from Aqueous Buffer. *Langmuir* **2001**, *17*, 2841–2850.
- (18) Grainger, D. W.; Stewart, C. W. Fluorinated Coatings and Films: Motivation and Significance. In *Fluorinated Surfaces, Coatings, and Films*; American Chemical Society: Washington, 2009.
- (19) Dalvi, V. H.; Rossky, P. J. Molecular Origins of Fluorocarbon Hydrophobicity. *Proc. Natl. Acad. Sci.* **2010**, *107*, 13603–13607.
- (20) Zenasni, O.; Jamison, A. C.; Lee, T. R. The Impact of Fluorination on the Structure and Properties of Self-Assembled Monolayer Films. *Soft Matter* **2013**, *9*, 6356–6370.
- (21) Zhao, Z.; Ni, H.; Han, Z.; Jiang, T.; Xu, Y.; Lu, X.; Ye, P. Effect of Surface Compositional Heterogeneities and Microphase Segregation of Fluorinated Amphiphilic Copolymers on Antifouling Performance. *ACS Appl. Mater. Interfaces* **2013**, *5*, 7808–7818.
- (22) Li, S.; Yang, D.; Tu, H.; Deng, H.; Du, D.; Zhang, A. Protein Adsorption and Cell Adhesion Controlled by the Surface Chemistry of Binary Perfluoroalkyl/Oligo(Ethylene Glycol) Self-Assembled Monolayers. *J. Colloid*

*Interface Sci.* **2013**, *402*, 284–290.

- (23) Gao, J.; Yan, D.; Ni, H.; Wang, L.; Yang, Y.; Wang, X. Protein-Resistance Performance Enhanced by Formation of Highly-Ordered Perfluorinated Alkyls on Fluorinated Polymer Surfaces. *J. Colloid Interface Sci.* **2013**, *393*, 361–368.
- (24) Lee, H. J.; Jamison, A. C.; Lee, T. R. Two Are Better than One: Bidentate Adsorbates Offer Precise Control of Interfacial Composition and Properties. *Chem. Mater.* **2016**, *28*, 5356–5364.
- (25) Pujari, S. P.; Spruijt, E.; Cohen Stuart, M. A.; Van Rijn, C. J. M.; Paulusse, J. M. J.; Zuilhof, H. Ultralow Adhesion and Friction of Fluoro-Hydro Alkyne-Derived Self-Assembled Monolayers on H-Terminated Si(111). *Langmuir* **2012**, *28*, 17690–17700.
- (26) Zenasni, O.; Jamison, A. C.; Marquez, M. D.; Lee, T. R. Self-Assembled Monolayers on Gold Generated from Terminally Perfluorinated Alkanethiols Bearing Propyl vs. Ethyl Hydrocarbon Spacers. *J. Fluor. Chem.* **2014**, *168*, 128–136.
- (27) Zenasni, O.; Marquez, M. D.; Jamison, A. C.; Lee, H. J.; Czader, A.; Lee, T. R. Inverted Surface Dipoles in Fluorinated Self-Assembled Monolayers. *Chem. Mater.* **2015**, *27*, 7433–7446.
- (28) Graupe, M.; Koini, T.; Wang, V. Y.; Nassif, G. M.; Colorado, R.; Villazana, R. J.; Dong, H.; Miura, Y. F.; Shmakova, O. E.; Lee, T. R. Terminally Perfluorinated Long-Chain Alkanethiols. *J. Fluor. Chem.* **1999**, *93*, 107–115.
- (29) Fukushima, H.; Seki, S.; Nishikawa, T.; Takiguchi, H.; Tamada, K.; Abe, K.;

- Colorado, R.; Graupe, M.; Shmakova, O. E.; Lee, T. R. Microstructure, Wettability, and Thermal Stability of Semifluorinated Self-Assembled Monolayers (SAMs) on Gold. *J. Phys. Chem. B* **2000**, *104*, 7417–7423.
- (30) Lee, S.; Park, J. S.; Lee, T. R. The Wettability of Fluoropolymer Surfaces: Influence of Surface Dipoles. *Langmuir* **2008**, *24*, 4817–4826.
- (31) Chinwangso, P.; Lee, H. J.; Lee, T. R. Self-Assembled Monolayers Generated from Unsymmetrical Partially Fluorinated Spiroalkanedithiols. *Langmuir* **2015**, *31*, 13341–13349.
- (32) Takenaga, M.; Jo, S.; Graupe, M.; Lee, T. R. Effective van Der Waals Surface Energy of Self-Assembled Monolayer Films Having Systematically Varying Degrees of Molecular Fluorination. *J. Colloid Interface Sci.* **2008**, *320*, 264–267.
- (33) Alesi, W. R.; Weinstein, R. D.; Cushnie, E.; Colorado, R.; Patel, M.; Moriarty, J.; Jennings, G. K.; Lee, T. R. Structure, Wettability, and Electrochemical Barrier Properties of Self-Assembled Monolayers Prepared from Partially Fluorinated Hexadecanethiols. *J. Phys. Chem. B* **2003**, *107*, 11626–11632.
- (34) Colorado, R.; Lee, T. R. Wettabilities of Self-Assembled Monolayers on Gold Generated from Progressively Fluorinated Alkanethiols. *Langmuir* **2003**, *19*, 3288–3296.
- (35) Zalipsky, S.; Harris, J. M. Introduction to Chemistry and Biological Applications of Poly(Ethylene Glycol). In *Poly(ethylene glycol)*; American Chemical Society: Washington, 2009.

- (36) Li, Z.; Narouz, M. R.; Munro, K.; Hao, B.; Crudden, C. M.; Horton, J. H.; Hao, H. Carboxymethylated Dextran-Modified N-Heterocyclic Carbene Self-Assembled Monolayers on Gold for Use in Surface Plasmon Resonance Biosensing. *ACS Appl. Mater. Interfaces* **2017**, *9*, 39223–39234.
- (37) Prime, K. L.; Whitesides, G. M. Adsorption of Proteins onto Surfaces Containing End-Attached Oligo(Ethylene Oxide): A Model System Using Self-Assembled Monolayers. *J. Am. Chem. Soc.* **1993**, *115*, 10714–10721.
- (38) Chinwangso, P.; Lee, H. J.; Jamison, A. C.; Marquez, M. D.; Park, C. S.; Lee, T. R. Structure, Wettability, and Thermal Stability of Organic Thin-Films on Gold Generated from the Molecular Self-Assembly of Unsymmetrical Oligo(Ethylene Glycol) Spiroalkanedithiols. *Langmuir* **2017**, *33*, 1751–1762.
- (39) Palazon, F.; Géhin, T.; Ferrah, D.; Garnier, A.; Botella, C.; Grenet, G.; Souteyrand, É.; Cloarec, J. P.; Chevolot, Y. X-Ray-Induced Degradation of OEG-Terminated SAMs on Silica Surfaces during XPS Characterization. *Surf. Interface Anal.* **2015**, *47*, 719–722.
- (40) Chang, Y.; Chu, W. L.; Chen, W. Y.; Zheng, J.; Liu, L.; Ruaan, R. C.; Higuchi, A. A Systematic SPR Study of Human Plasma Protein Adsorption Behavior on the Controlled Surface Packing of Self-Assembled Poly(Ethylene Oxide) Triblock Copolymer Surfaces. *J. Biomed. Mater. Res. - Part A* **2010**, *93*, 400–408.
- (41) Emmenegger, C. R.; Brynda, E.; Riedel, T.; Sedlakova, Z.; Houska, M.; Alles, A. B. Interaction of Blood Plasma with Antifouling Surfaces. *Langmuir* **2009**, *25*, 6328–6333.

- (42) Sun, F.; Ella-Menye, J. R.; Galvan, D. D.; Bai, T.; Hung, H. C.; Chou, Y. N.; Zhang, P.; Jiang, S.; Yu, Q. Stealth Surface Modification of Surface-Enhanced Raman Scattering Substrates for Sensitive and Accurate Detection in Protein Solutions. *ACS Nano* **2015**, *9*, 2668–2676.
- (43) Li, G.; Cheng, G.; Xue, H.; Chen, S.; Zhang, F.; Jiang, S. Ultra Low Fouling Zwitterionic Polymers with a Biomimetic Adhesive Group. *Biomaterials* **2008**, *29*, 4592–4597.
- (44) Lin, P.; Chuang, T.-L.; Chen, P. Z.; Lin, C.-W.; Gu, F. X. Low-Fouling Characteristics of Ultrathin Zwitterionic Cysteine SAMs. *Langmuir* **2018**, *35*, 1756–1767.
- (45) Ederth, T.; Lerm, M.; Orihuela De Diaz, B.; Rittschof, D. The Resistance of Zwitterionic Peptide Monolayers to Biofouling. *Langmuir* **2018**, *35*, 1818–1827.
- (46) Bauer, S.; Alles, M.; Finlay, J. A.; Callow, J. A.; Callow, M. E.; Rosenhahn, A. Influence of Zwitterionic SAMs on Protein Adsorption and the Attachment of Algal Cells. *J. Biomater. Sci. Polym. Ed.* **2014**, *25*, 1530–1539.
- (47) Schlenoff, J. B. Zwitteration: Coating Surfaces with Zwitterionic Functionality to Reduce Nonspecific Adsorption. *Langmuir* **2014**, *30*, 9625–9636.
- (48) Pensa, E.; Cortés, E.; Corthey, G.; Carro, P.; Vericat, C.; Fonticelli, M. H.; Benítez, G.; Rubert, A. A.; Salvarezza, R. C. The Chemistry of the Sulfur-Gold Interface: In Search of a Unified Model. *Acc. Chem. Res.* **2012**, *45*, 1183–1192.
- (49) Phillips, K. S.; Cheng, Q. J. Surface Plasmon Resonance. In *Molecular Biomethods*

*Handbook: Second Edition*; Humana: Totowa, 2008.

- (50) Homola, J.; Yee, S. S.; Gauglitz, G. Surface Plasmon Resonance Sensors: Review. *Sensors Actuators, B Chem.* **1999**, *54*, 3–15.
- (51) Tudos, A. J.; Schasfoort, R. B. M. Chapter 1. Introduction to Surface Plasmon Resonance. In *Handbook of Surface Plasmon Resonance*; Royal Society of Chemistry: Cambridge, 2010.
- (52) Salamon, Z.; Tollin, G. Surface Plasmon Resonance, Theory. In *Encyclopedia of Spectroscopy and Spectrometry*; Academic Press: Cambridge, 2016.
- (53) Nguyen, H. H.; Park, J.; Kang, S.; Kim, M. Surface Plasmon Resonance: A Versatile Technique for Biosensor Applications. *Sensors (Switzerland)* **2015**, *15*, 10481–10510.
- (54) Beseničar, M.; Maček, P.; Lakey, J. H.; Anderluh, G. Surface Plasmon Resonance in Protein-Membrane Interactions. *Chem. Phys. Lipids* **2006**, *141*, 169–178.
- (55) Tudos, A. J.; Schasfoort, R. B. M. Introduction to Surface Plasmon Resonance. In *Handbook of Surface Plasmon Resonance*; Royal Society of Chemistry: Philadelphia, 1968.
- (56) Wu, B.; Mathews, N.; Sum, T. C. Surface Plasmon Resonance. In *SpringerBriefs in Applied Sciences and Technology*; Springer: Singapore, 2017.
- (57) Tang, Y.; Zeng, X.; Liang, J. Surface Plasmon Resonance: An Introduction to a Surface Spectroscopy Technique. *J. Chem. Educ.* **2010**, *87*, 742–746.
- (58) de Mol, N. J.; Fischer, M. J. E. Surface Plasmon Resonance: A General Introduction.

*Methods in Molecular Biology*; Humana: Clifton, 2010.

- (59) Mol, Nico J ; Fischer, M. J. E.; Merwe, P. A. Van Der. *Surface Plasmon Resonance: Methods and Protocol*; Humana: New york, 2010.
- (60) Arwin, H.; Poksinski, M.; Johansen, K. Total Internal Reflection Ellipsometry: Principles and Applications. *Appl. Opt.* **2004**, *43*, 3028–3036.
- (61) Incorporation, N. Overview of Surface Plasmon Resonance. *Order A J. Theory Ordered Sets Its Appl.* **2010**.
- (62) Akimov, Y.; Pam, M. E.; Sun, S. Kretschmann-Raether Configuration: Revision of the Theory of Resonant Interaction. *Phys. Rev. B* **2017**, *96*, 155433–155440.
- (63) Aldred, N.; Ekblad, T.; Andersson, O.; Liedberg, B.; Clare, A. S. Real-Time Quantification of Microscale Bioadhesion Events in Situ Using Imaging Surface Plasmon Resonance (ISPR). *ACS Appl. Mater. Interfaces* **2011**, *3*, 2085–2091.
- (64) Yu, Y.; Frey, H. Controllable Nonspecific Protein Adsorption by Charged Hyperbranched Polyglycerol Thin Films. *Langmuir* **2015**, *31*, 13101–13106.
- (65) Chapman, R. G.; Ostuni, E.; Takayama, S.; Holmlin, R. E.; Yan, L.; Whitesides, G. M. Surveying for Surfaces That Resist the Adsorption of Proteins. **2010**, *122*, 8303–8304.
- (66) Ye, H.; Wang, L.; Huang, R.; Su, R.; Liu, B.; Qi, W.; He, Z. Superior Antifouling Performance of a Zwitterionic Peptide Compared to an Amphiphilic, Non-Ionic Peptide. *ACS Appl. Mater. Interfaces* **2015**, *7*, 22448–22457.
- (67) Luan, Y.; Li, D.; Wang, Y.; Liu, X.; Brash, J. L.; Chen, H. 125I-Radiolabeling,

Surface Plasmon Resonance, and Quartz Crystal Microbalance with Dissipation: Three Tools to Compare Protein Adsorption on Surfaces of Different Wettability. *Langmuir* **2014**, *30*, 1029–1035.

- (68) Li, Z.; Köwitsch, A.; Zhou, G.; Groth, T.; Fuhrmann, B.; Niepel, M.; Amado, E.; Kressler, J. Enantiopure Chiral Poly(Glycerol Methacrylate) Self-Assembled Monolayers Knock down Protein Adsorption and Cell Adhesion. *Adv. Healthc. Mater.* **2013**, *2*, 1377–1387.
- (69) Dubacheva, G. V.; Araya-Callis, C.; Geert Volbeda, A.; Fairhead, M.; Codée, J.; Howarth, M.; Richter, R. P. Controlling Multivalent Binding through Surface Chemistry: Model Study on Streptavidin. *J. Am. Chem. Soc.* **2017**, *139*, 4157–4167.
- (70) Frey, W.; Meyer, D. E.; Chilkoti, A. Thermodynamically Reversible Addressing of a Stimuli Responsive Fusion Protein onto a Patterned Surface Template. *Langmuir* **2003**, *19*, 1641–1653.
- (71) Yang, Z.; Frey, W.; Oliver, T.; Chilkoti, A. Light-Activated Affinity Micropatterning of Proteins on Self-Assembled Monolayers on Gold. *Langmuir* **2000**, *16*, 1751–1758.
- (72) Bhan, C.; Brower, T. L.; Raghavan, D. SPR Studies of the Adsorption of Silver/Bovine Serum Albumin Nanoparticles (Ag/BSA NPs) onto the Model Biological Substrates. *J. Colloid Interface Sci.* **2013**, *402*, 40–49.
- (73) Altintas, Z.; Uludag, Y.; Gurbuz, Y.; Tothill, I. Development of Surface Chemistry for Surface Plasmon Resonance Based Sensors for the Detection of Proteins and DNA Molecules. *Anal. Chim. Acta* **2012**, *712*, 138–144.

- (74) Ataman Sadık, D.; Eksi-Kocak, H.; Ertaş, G.; Boyacı, İ. H.; Mutlu, M. Mixed-Monolayer of N-Hydroxysuccinimide-Terminated Cross-Linker and Short Alkanethiol to Improve the Efficiency of Biomolecule Binding for Biosensing. *Surf. Interface Anal.* **2018**, *50*, 866–878.
- (75) Holzer, B.; Manoli, K.; Ditaranto, N.; Macchia, E.; Tiwari, A.; Di Franco, C.; Scamarcio, G.; Palazzo, G.; Torsi, L. Characterization of Covalently Bound Anti-Human Immunoglobulins on Self-Assembled Monolayer Modified Gold Electrodes. *Adv. Biosyst.* **2017**, *1*, 1700055.
- (76) Smith, A. L. Chapter 5 The Quartz Crystal Microbalance. In *Handbook of Thermal Analysis and Calorimetry*; Elsevier B.V.: London, 2008.
- (77) O’Sullivan, C. K.; Guilbault, G. G. Commercial Quartz Crystal Microbalances - Theory and Applications. *Biosens. Bioelectron.* **1999**, *14*, 663–670.
- (78) Speight, R. E.; Cooper, M. A. A Survey of the 2010 Quartz Crystal Microbalance Literature. *J. Mol. Recognit.* **2012**, *25*, 451–473.
- (79) Ispas, A.; Bund, A. Electrochemical Quartz Crystal Microbalance. In *Encyclopedia of Applied Electrochemistry*; Springer: New York, 2014.
- (80) Lu, C.; Czanderna, A. W.; Townshend, A. *Applications of Piezoelectric Quartz Crystal Microbalances*; Elsevier B.V.: New York, 1984.
- (81) Mansfield, E.; Kar, A.; Quinn, T. P.; Hooker, S. A. Quartz Crystal Microbalances for Microscale Thermogravimetric Analysis. *Anal. Chem.* **2010**, *82*, 9977–9982.
- (82) Buttry, D. A.; Ward, M. D. Measurement of Interfacial Processes at Electrode

- Surfaces with the Electrochemical Quartz Crystal Microbalance. *Chem. Rev.* **1992**, *92*, 1355–1379.
- (83) Gamry Instruments. Basics of a Quartz Crystal Microbalance. *Spectrum* **2012**, *1*, 1–7.
- (84) Keiji Kanazawa, K.; Gordon, J. G. The Oscillation Frequency of a Quartz Resonator in Contact with Liquid. *Anal. Chim. Acta* **1985**, *175*, 99–105.
- (85) Wang, H.; Cheng, F.; Li, M.; Peng, W.; Qu, J. Reactivity and Kinetics of Vinyl Sulfone-Functionalized Self-Assembled Monolayers for Bioactive Ligand Immobilization. *Langmuir* **2015**, *31*, 3413–3421.
- (86) Von Vacano, B.; Xu, R.; Hirth, S.; Herzenstiel, I.; Rückel, M.; Subkowski, T.; Baus, U. Hydrophobin Can Prevent Secondary Protein Adsorption on Hydrophobic Substrates without Exchange. *Anal. Bioanal. Chem.* **2011**, *7*, 2031–2040.
- (87) Fabre, H.; Mercier, D.; Galtayries, A.; Portet, D.; Delorme, N.; Bardeau, J. F. Impact of Hydrophilic and Hydrophobic Functionalization of Flat TiO<sub>2</sub>/Ti Surfaces on Proteins Adsorption. *Appl. Surf. Sci.* **2018**, *432*, 15–21.
- (88) Hook, F.; Brzezinski, P.; Rodahl, M.; Kasemo, B. Structural Changes in Hemoglobin during Adsorption to Solid Surfaces: Effects of PH, Ionic Strength and Ligand Binding. *Proc. Natl. Acad. Sci.* **1997**, *95*, 12271–12276.
- (89) Huang, C.-J.; Wang, L.-C.; Liu, C.-Y.; Chiang, A. S. T.; Chang, Y.-C.; Wang, L.-C.; Huang, C.-J.; Chiang, A. S. T.; Chang, Y.-C. Natural Zwitterionic Organosulfurs as Surface Ligands for Antifouling and Responsive Properties. *Biointerphases* **2014**,

No. 2, 29010.

- (90) Lamberg, P.; Hamit-Eminovski, J.; Toscano, M. D.; Eicher-Lorka, O.; Niaura, G.; Arnebrant, T.; Shleev, S.; Ruzgas, T. Electrical Activity of Cellobiose Dehydrogenase Adsorbed on Thiols: Influence of Charge and Hydrophobicity. *Bioelectrochemistry* **2017**, *115*, 26–32.
- (91) Phan, H. T. M.; Bartelt-Hunt, S.; Rodenhausen, K. B.; Schubert, M.; Bartz, J. C. Investigation of Bovine Serum Albumin (BSA) Attachment onto Self-Assembled Monolayers (SAMs) Using Combinatorial Quartz Crystal Microbalance with Dissipation (QCM-D) and Spectroscopic Ellipsometry (SE). *PLoS One* **2015**, *10*, 1–20.
- (92) Huang, S.; Hou, Q.; Guo, D.; Yang, H.; Chen, T.; Liu, F.; Hu, G.; Zhang, M.; Zhang, J.; Wang, J. Adsorption Mechanism of Mussel-Derived Adhesive Proteins onto Various Self-Assembled Monolayers. *RSC Adv.* **2017**, *7*, 39530–39538.
- (93) Nelson, G. W.; Parker, E. M.; Singh, K.; Blanford, C. F.; Moloney, M. G.; Foord, J. S. Surface Characterization and in Situ Protein Adsorption Studies on Carbene-Modified Polymers. *Langmuir* **2015**, *31*, 11086–11096.
- (94) Leo, N.; Liu, J.; Archbold, I.; Tang, Y.; Zeng, X. Ionic Strength, Surface Charge, and Packing Density Effects on the Properties of Peptide Self-Assembled Monolayers. *Langmuir* **2017**, *33*, 2050–2058.
- (95) Chen, P. C.; Huang, X. J.; Xu, Z. K. Activation and Deformation of Immobilized Lipase on Self-Assembled Monolayers with Tailored Wettability. *Phys. Chem.*

- Chem. Phys.* **2015**, *17*, 13457–13465.
- (96) Srinivasan, K.; Sorci, M.; Sejergaard, L.; Ranjan, S.; Belfort, G.; Cramer, S. M. Protein Binding Kinetics in Multimodal Systems: Implications for Protein Separations. *Anal. Chem.* **2018**, *90*, 2609–2617.
- (97) Lee, H. H.; Gavutis, M.; Ružele, Ž.; Valiokas, R. N.; Liedberg, B. Mixed Self-Assembled Monolayers with Terminal Deuterated Anchors: Characterization and Probing of Model Lipid Membrane Formation. *J. Phys. Chem. B* **2018**, *122*, 8201–8210.
- (98) Engel, A.; Lyubchenko, Y.; Müller, D. Atomic Force Microscopy: A Powerful Tool to Observe Biomolecules at Work. *Trends Cell Biol.* **1999**, *9*, 77–80.
- (99) Variola, F. Atomic Force Microscopy in Biomaterials Surface Science. *Phys. Chem. Chem. Phys.* **2015**, *17*, 2950–2959.
- (100) Allison, D. P.; Mortensen, N. P.; Sullivan, C. J.; Doktycz, M. J. Atomic Force Microscopy of Biological Samples. *Wiley Interdiscip. Rev. Nanomedicine Nanobiotechnology* **2010**, *2*, 618–634.
- (101) Kushmerick, J. G.; Weiss, P. S. Scanning Probe Microscopes. In *Encyclopedia of Spectroscopy and Spectrometry*; Academic Press: Cambridge, 2016.
- (102) Whited, A. M.; Park, P. S. H. Atomic Force Microscopy: A Multifaceted Tool to Study Membrane Proteins and Their Interactions with Ligands. *Biochim. Biophys. Acta - Biomembr.* **2014**, *1838*, 56–68.
- (103) Yablon, D. G. Overview of Atomic Force Microscopy. In *Scanning Probe*

*Microscopy for Industrial Applications: Nanomechanical Characterization*; John Wiley & Sons, Inc.: Hoboken, 2013.

- (104) Schönherr, H.; Vancso, G. J. Atomic Force Microscopy in Practice. In *Scanning Force Microscopy of Polymers*; Springer: Berlin, 2010.
- (105) Jalili, N.; Laxminarayana, K. A Review of Atomic Force Microscopy Imaging Systems: Application to Molecular Metrology and Biological Sciences. *Mechatronics* **2004**, *14*, 907–945.
- (106) Friedbacher, G. Atomic Force Microscopy (AFM). In *Surface and Thin Film Analysis: A Compendium of Principles, Instrumentation, and Applications, Second Edition*; Wiley-VCH: Weinheim, 2011.
- (107) Servoli, E.; Maniglio, D.; Aguilar, M. R.; Motta, A.; San Roman, J.; Belfiore, L. A.; Migliaresi, C. Quantitative Analysis of Protein Adsorption via Atomic Force Microscopy and Surface Plasmon Resonance. *Macromol. Biosci.* **2008**, *8*, 1126–1134.
- (108) Christman, J. A.; Woolcott, R. R.; Kingon, A. I.; Nemanich, R. J. Piezoelectric Measurements with Atomic Force Microscopy. *Appl. Phys. Lett.* **1998**, *73*, 3851–3853.
- (109) Cappella, B.; Dietler, G. Force-Distance Curves by Atomic Force Microscopy. *Surf. Sci. Rep.* **1999**, *34*, 5–104.
- (110) Cruz, T. G. S.; Albuquerque, D. A. C.; De, R. R. L.; Yamaji, F. M.; Leite, F. L. Measurement of the Nanoscale Roughness by Atomic Force Microscopy: Basic

Principles and Applications. In *Atomic Force Microscopy - Imaging, Measuring and Manipulating Surfaces at the Atomic Scale*; IntechOpen: London, 2012.

- (111) Dupont-Gillain, C. C.; Fauroux, C. M. J.; Gardner, D. C. J.; Leggett, G. J. Use of AFM to Probe the Adsorption Strength and Time-Dependent Changes of Albumin on Self-Assembled Monolayers. *J. Biomed. Mater. Res. - Part A* **2003**, *67A*, 548–558.
- (112) Kim, J.; Cho, J.; Seidler, P. M.; Kurland, N. E.; Yadavalli, V. K. Investigations of Chemical Modifications of Amino-Terminated Organic Films on Silicon Substrates and Controlled Protein Immobilization. *Langmuir* **2010**, *26*, 2599–2608.
- (113) Asiaei, S.; Nieva, P.; Vijayan, M. M. Fast Kinetics of Thiolic Self-Assembled Monolayer Adsorption on Gold: Modeling and Confirmation by Protein Binding. *J. Phys. Chem. B* **2014**, *118*, 13697–13703.
- (114) Solano, I.; Parisse, P.; Gramazio, F.; Cavalleri, O.; Bracco, G.; Castronovo, M.; Casalis, L.; Canepa, M. Spectroscopic Ellipsometry Meets AFM Nanolithography: About Hydration of Bio-Inert Oligo(Ethylene Glycol)-Terminated Self Assembled Monolayers on Gold. *Phys. Chem. Chem. Phys.* **2015**, *17*, 28774–28781.
- (115) Solano, I.; Parisse, P.; Gramazio, F.; Ianeselli, L.; Medagli, B.; Cavalleri, O.; Casalis, L.; Canepa, M. Atomic Force Microscopy and Spectroscopic Ellipsometry Combined Analysis of Small Ubiquitin-like Modifier Adsorption on Functional Monolayers. *Appl. Surf. Sci.* **2017**, *421*, 722–727.
- (116) Araki, Y.; Sekine, T.; Chang, R.; Hayashi, T.; Onishi, H. Molecular-Scale Structures

- of the Surface and Hydration Shell of Bioinert Mixed-Charged Self-Assembled Monolayers Investigated by Frequency Modulation Atomic Force Microscopy. *RSC Adv.* **2018**, *8*, 24660–24664.
- (117) Tompkins, H. G.; Tasic, S.; Baker, J.; Convey, D. Spectroscopic Ellipsometry Measurements of Thin Metal Films. *Surf. Interface Anal.* **2000**, *29*, 179–187.
- (118) Tompkins, H. G.; Irene, A. E. Theory of Ellipsometry. In *Handbook of Ellipsometry*; William Andrew Publishing: Norwich, 2005.
- (119) Schubert, M. Theory and Application of Generalized Ellipsometry. In *Handbook of Ellipsometry*; William Andrew Publishing: Norwich, 2005.
- (120) Losurdo, M.; Hingerl, K. *Ellipsometry at the Nanoscale*; Springer: Heidelberg, 2013.
- (121) Al-Azzawi, A. Polarization of Light. In *Light and Optics: Principles and Practices*; CRC Press LLC: Boca Raton, 2010.
- (122) Jellison, G. E. Data Analysis for Spectroscopic Ellipsometry. *Thin Solid Films* **1993**, *234*, 416–422.
- (123) Bordi, F.; Prato, M.; Cavalleri, O.; Cametti, C.; Canepa, M.; Gliozzi, A. Azurin Self-Assembled Monolayers Characterized by Coupling Electrical Impedance Spectroscopy and Spectroscopic Ellipsometry. *J. Phys. Chem. B* **2004**, *108*, 20263–20272.
- (124) Chieh, H. F.; Su, F. C.; Liao, J. Der; Lin, S. C.; Chang, C. W.; Shen, M. R. Attachment and Morphology of Adipose-Derived Stromal Cells and Exposure of Cell-Binding Domains of Adsorbed Proteins on Various Self-Assembled

- Monolayers. *Soft Matter* **2011**, 7, 3808–3817.
- (125) Lestelius, M.; Liedberg, B.; Tengvall, P. *In Vitro* Plasma Protein Adsorption on  $\omega$ -Functionalized Alkanethiolate Self-Assembled Monolayers. *Langmuir* **1997**, 13, 5900–5908.
- (126) Bonnet, N.; O'Hagan, D.; Hähner, G. Protein Adsorption onto CF<sub>3</sub>-Terminated Oligo(Ethylene Glycol) Containing Self-Assembled Monolayers (SAMs): The Influence of Ionic Strength and Electrostatic Forces. *Phys. Chem. Chem. Phys.* **2010**, 12, 4367–4374.
- (127) Vickerman, J. C.; Gilmore, I. S. *Surface Analysis - The Principal Techniques: Second Edition*; John Wiley & Sons, Inc.: Hoboken, 2009.
- (128) Crist, B. V. *Handbook of the Elements and Native Oxides*; Wiley: Hoboken, 1999.
- (129) Crist, V. Binding Energies Lookup Table for Signals from Elements and Common Chemical Species. In *Handbook of Monochromatic XPS Spectra - Elements and Native Oxides*; Wiley: Hoboken, 2000.
- (130) Watts, J. F.; Wolstenholme, J. *An Introduction to Surface Analysis by XPS and AES*; John Wiley & Sons, Ed.; Hoboken, 2005.
- (131) Geng, S.; Zhang, S.; Onishi, H. XPS Applications in Thin Films Research. *Mater. Technol.* **2002**, 17, 234–240.
- (132) Vincent Crist, B. *Handbooks of Monochromatic XPS Spectra Volume 1 - The Elements and Native Oxides*; Wiley: Hoboken, 1999.
- (133) Baer, D. R.; Engelhard, M. H. XPS Analysis of Nanostructured Materials and

- Biological Surfaces. *J. Electron Spectros. Relat. Phenomena* **2010**, *178*, 415–432.
- (134) Seah, M. P. The Quantitative Analysis of Surfaces by XPS: A Review. *Surf. Interface Anal.* **1980**, *2*, 222–239.
- (135) Seah, M. .; Gilmore, I. .; Spencer, S. . Quantitative XPS. *J. Electron Spectros. Relat. Phenomena* **2002**, *120*, 93–111.
- (136) van der Heide, P. *X-Ray Photoelectron Spectroscopy: An Introduction to Principles and Practices*; John Wiley & Sons, Inc.: Hoboken, 2011.
- (137) Chen, Y.; Thayumanavan, S. Amphiphilicity in Homopolymer Surfaces Reduces Nonspecific Protein Adsorption. *Langmuir* **2009**, *25*, 13795–13799.
- (138) Cho, H. M.; Chegal, W.; Kim, Y. P.; Cho, Y. J.; Kim, H. S. Imaging Ellipsometry Combined with Surface Plasmon Resonance for Real-Time Biospecific Interaction Analysis. In *Nanosensing: Materials and Devices II*; 2005; Vol. 6008.
- (139) Reimhult, E.; Larsson, C.; Kasemo, B.; Höök, F. Simultaneous Surface Plasmon Resonance and Quartz Crystal Microbalance with Dissipation Monitoring Measurements of Biomolecular Adsorption Events Involving Structural Transformations and Variations in Coupled Water. *Anal. Chem.* **2004**, *76*, 7211–7220.

## **Chapter 2. Anti-fouling Studies of Partially Fluorinated Spiroalkanedithiol Self-Assembled Monolayers**

### **2.1. Introduction**

Biofouling creates challenges in an array of applications, including biosensors, medical implants, surgical instruments, marine equipment, cookware, protective apparel, and food packaging.<sup>1-3</sup> In medical devices, biocontamination of electronic products can interfere with device performance, product efficiency, and customer safety. Moreover, uncontrolled adhesion of biomaterials (e.g., proteins) on implanted medical devices can diminish the effectiveness of the device and the health of the patient.<sup>1</sup> Research on novel anti-fouling coatings is one of the main active areas of material and interfacial science.<sup>4-7</sup> To this end, organic thin films bearing polyethylene glycol (PEG) termini have been widely used as coatings for biomedical applications. This type of coating exhibits a high degree of biological inertness.<sup>8</sup> However, PEG-based coatings are hindered by the reactivity of the molecules toward atmospheric oxygen.<sup>9</sup> The discovery of polytetrafluoroethylene (PTFE), commonly known as Teflon, has generated attention and has been incorporated into thin film coatings. PTFE is a well-recognized anti-adhesive material with desirable interfacial properties, such as low wettability, low friction, as well as low adhesion.<sup>10-14</sup> Fluorination in nanostructured thin films (1-2 nm thickness) generate materials with unique interfacial chemistry that is desired to reduce fouling of the surface.

Thin film coatings generated using the process of self-assembly present well-defined, highly ordered homogeneous surfaces known as self-assembled monolayers (SAMs).<sup>15</sup> SAMs are easily modified and controlled to generate surfaces employed in studies to understand interactions with various materials at the interface of the

SAM. SAMs of thiolates on gold serve as a versatile system for studying the interfacial properties of films, which subsequently leads to the development of novel anti-fouling surfaces.<sup>11</sup> SAMs have several advantages, such as ease of reproducibility, moderate stability of the films, as well as the ease of adsorbate manipulation by means of organic reactions.<sup>16</sup> Well-established chemistries can be used to generate a variety of surfaces, including those that are PEG-functionalized, fluorinated, charged, or zwitterionic.<sup>17-26</sup> Furthermore, these tools have allowed for the synthesis of partially fluorinated adsorbates to generate thin films with interfacial properties similar to those of PTFE. Thus, similarly to PTFE, fluorinated SAMs (FSAMs) have been shown to exhibit high hydrophobic and oleophobic behavior as well as chemical and thermal stability.<sup>4,10,27-29</sup> The incorporation of fluorinated-termini in the structure of thiolated adsorbates bridges the gaps in applications where the use of fluorinated polymers is inappropriate. Research on fluorinated SAMs has shown that the structure of the film is greatly affected by the hydrocarbon spacer of the adsorbates, whereas the fluorinated segments dictate the interfacial properties and thermal stability of the film.<sup>10,11,16,27,28</sup>

An attractive method used to manipulate the interfacial properties involves the use of multiple adsorbates bearing dissimilar functional groups with the overall goal of tailoring the interfacial properties.<sup>30,31</sup> However, the incorporation of two separate monodentate thiols with chemically dissimilar tailgroups often leads to films comprised of phase separated domains due to their incompatibility.<sup>32-35</sup> Only recently, Chinwangso and co-workers demonstrated the ability to generate films with controlled interfacial heterogeneity by linking two chemically dissimilar chains -- combinations of a hydrocarbon chain with a partially fluorinated chain or an oligo(ethylene

glycol) chain -- on a bidentate spiroalkanedithiol (SADT) headgroup, featured in Figure 2.1.<sup>18,36-38</sup>

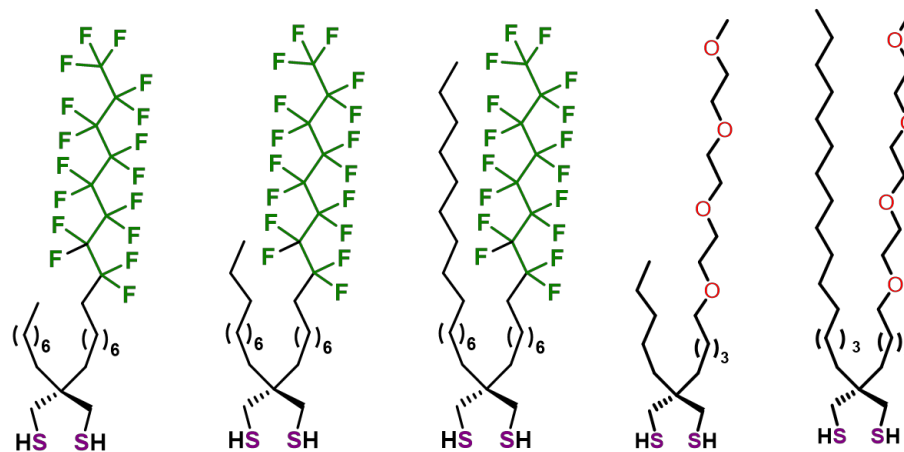


**Figure 2.1.** Molecular structures of unsymmetrical spiroalkanedithiols (SADTs) prepared by the Chinwangso et al.<sup>18,36,37</sup>

The research described herein investigates the interaction of mixed interfaces generated from partially fluorinated spiroalkanedithiols with a variety of common biocontaminants to assess the ability of the SAMs to resist protein adhesion. The outlined strategy of this work is to generate interfacially "conflicted" monolayers on gold surfaces. We use the term "conflicted" to emphasize that the interfaces are comprised of chemically disparate species that are held in close proximity, while preferring to be apart. Specifically, we generated SAMs from unsymmetrical partially fluorinated spiroalkanedithiols (SADTs), **F8H10-C12** and **F8H10-C18**, to study protein adhesion on these unique heterogeneous surfaces (see Figure 2.2 for the molecular structure). The performance of the SADT-based SAMs was compared to SAMs generated from an analogous *n*-alkanethiol (**C16SH**) and a partially fluorinated monodentate adsorbate (**F8H8SH**) to evaluate the effect of adsorbate structure on the anti-adhesive properties of the films. The proteins used

in the study to evaluate the anti-adhesive properties were protamine, lysozyme, bovine serum albumin (BSA), and fibrinogen. We have hypothesized that the chemical heterogeneity introduced at the interfaces of the bis-functionalized spiroalkanedithiolated SAMs would lead to a reduction of favorable interactions between the contacting proteins and the SAM.<sup>39</sup> Simultaneously, the perfluorinated segment should help maintain the structural and thermal stability of the film.<sup>10,11,27,28,36,37</sup> Notably, adsorbate **F8H8-C12** is designed to create SAMs that allow the bulky helical fluorinated chains to pack atop the underlying well-packed trans-extended alkyl chains. We characterized the aforementioned anti-adhesive properties of the generated films using optical ellipsometry, quartz crystal microbalance (QCM), surface plasmon resonance (SPR), and atomic force microscopy (AFM).

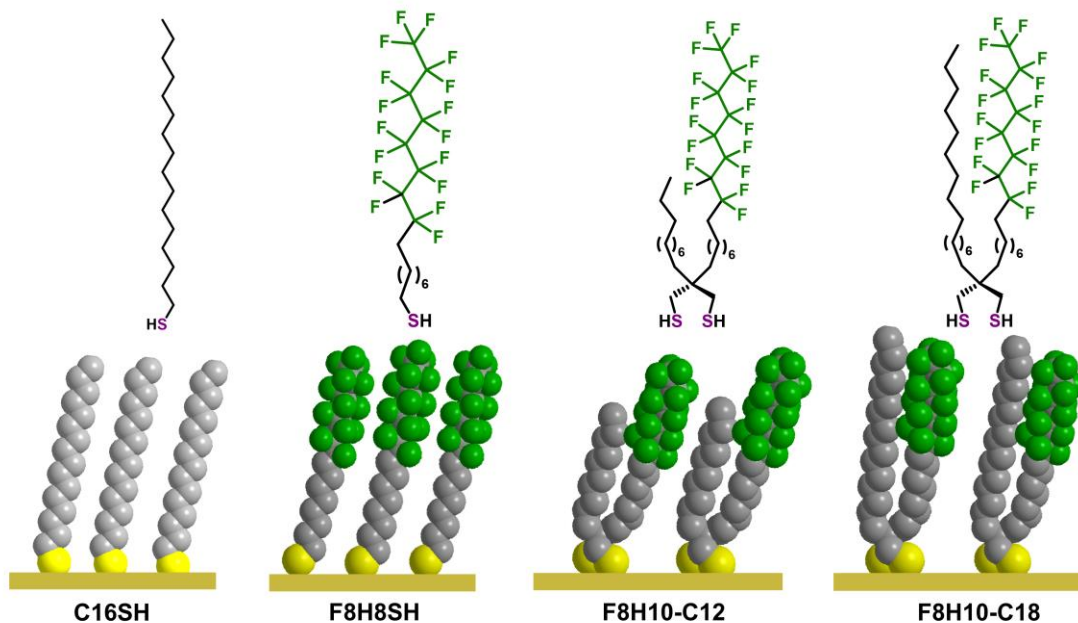


**Figure 2.2.** Molecular structures of the adsorbates and illustration of SAMs derived from the monodentate, **C16SH** and **F8H8SH**, as well as the SADT adsorbates, **F8H10-C12** and **F8H10-C18**, analyzed in this study.

## 2.2. Experimental Section

### 2.2.1. Materials

Absolute Ethanol (200 proof) from Aaper Alcohol and Chemical Co, Tetrahydrofuran (THF), sulfuric acid (H<sub>2</sub>SO<sub>4</sub>) both from Avantor Performance Materials, and hydrogen peroxide (30% H<sub>2</sub>O<sub>2</sub>) from Mallinckrodt Chemicals were all used as received. The adsorbate 1-hexadecanethiol (**C16SH**) was purchased from Sigma-Aldrich. The other adsorbates, 9,9,10,10,11,11,12,12,13,13,14,14,15,15,16,16,16-heptadecafluorohexadecane-1-thiol (**F8H8SH**) 2-decyl-2-(9,9,10,10,11,11,12,12,13,13,14,14,15,15,16,16,16-heptadecafluorohexa-decyl)propane-1,3-dithiol (**F8H10-C12**), and 2-(9,9,10,10,11,11,12,12,13,13,14,14,15,15,16,16,16-heptadecafluorohexadecyl)-2-hexadecylpropane-1,3-dithiol (**F8H10-C18**) were synthesized according to procedures found in the literature.<sup>13,36</sup> Fibrinogen, lysozyme, bovine serum albumin (BSA), and protamine, from Sigma Aldrich, were all used as received. Phosphate buffer solution (PBS) 10x from GenDepot was diluted to 1x using water (H<sub>2</sub>O) generated from a Milli-Q water system with resistance of 18.2 MΩ.

Gold shot (99.999%) was purchased from Kamis, Inc.. Chromium rods (99.9%) were purchased from Kurt J. Lesker Company. Polished single-crystal Si(100) wafers were purchased from University Wafer and rinsed with absolute ethanol before use. SPR sensors composed of 500 Å of Au plated onto Ti-coated silica substrates were purchased from Sofchip. The QCM sensors composed of polished AT-cut quartz crystals oscillating at a 10 MHz frequency coated with Ti and plated with 1000 Å of Au were purchased from International Crystal Manufacturing Company, Inc. NTESPA AFM cantilevers

made from antimony (n)-doped silicon tips with reflective aluminum coating (MPP-11220-10) were obtained from Bruker. Ultra-flat gold, 1000 Å of gold on a silicon wafer, was purchased from Platypus Technology and used as received.

### **2.2.2. Preparation of Substrates**

Gold substrates used in ellipsometric thickness measurements were prepared by thermal evaporation onto Si(100) wafers under vacuum at a pressure  $\leq 6 \times 10^{-5}$  torr. A chromium adhesion layer (100 Å) was initially deposited, followed by a gold layer (1000 Å) at a rate of 0.5 Å/s. Prior to being used, QCM and SPR sensors were cleaned with piranha solution, rinsed with copious amounts of Milli-Q water, then absolute ethanol, and finally dried in a stream of ultra-pure nitrogen gas. *Caution: Piranha solution reacts violently with organic materials and should be handled carefully!*

### **2.2.3. Preparation of SAMs**

All vials were cleaned using piranha solution prior to preparation of the adsorbate solutions. SAMs were prepared by incubating the respective gold samples (evaporated gold, QCM, SPR sensors, or ultra- flat gold on silica) in 1 mM solution of thiol, prepared in absolute ethanol. The SAMs were allowed to equilibrate for 48 h at rt in the dark. Prior to any measurements, all films were rinsed with THF, followed by absolute ethanol, and dried with ultra-pure nitrogen.

### **2.2.4. Protein Preparation/Exposure**

Protein solutions were prepared by dissolving 1 mg of the protein in 1 mL of the PBS solution. All buffers and protein solutions were filtered through a 0.2 µm filter. Following preparation, all solutions were sonicated for 15 min. After SAM formation, the

thermally evaporated Au samples, QCM sensors, and ultra-flat gold were immersed in the protein solutions for 1 h to reach saturation on the surface. Subsequently, samples were rinsed first with PBS buffer followed with Milli-Q water, and then dried with a stream of ultra-pure nitrogen gas. For the SPR sensors, the protein solution was loaded into a Biacore instrument (details below), where the protein solution was injected and then flowed over the surface of the SAM.

### **2.2.5. Ellipsometry Measurements**

Monolayer thicknesses were measured using a Rudolph Auto EL III ellipsometer equipped with a He-Ne laser (632.8 nm) at an incident angle of 70°. The refractive index was set to 1.45. The reported thickness values of the SAMs formed on the evaporated gold substrate are an average of 24 measurements (2 measurements per slide with 4 slides for each adsorbate with 3 independent trials). After SAM formation, the thin films were exposed to protein solutions for 1 h to allow the surface to become saturated, the ellipsometric thickness was measured again to determine changes in thickness due to protein exposure. The change in thickness was obtained by subtracting the initial SAM thickness from the total thickness measurement of the SAM after the protein exposure, which yields the thickness value of the absorbed protein. The reported thickness measurements of the SAMs after protein exposure are an average of 6 measurements from 3 individual trials. SAM formation on the evaporated gold, SPR, QCM and AFM surfaces was characterized using optical ellipsometry. The evaporated gold surface was used to report the ellipsometric values but no distinguishable difference in SAMs thickness or change in thickness after exposure to protein between the evaporated gold, QCM, and AFM surfaces was observed.

### 2.2.6. SPR Procedures

The SPR sensorgrams were obtained using a Biacore 2000. Sensors were initially exposed to PBS buffer at a rate of 30  $\mu\text{L}/\text{min}$ , followed by a 300  $\mu\text{L}$  injection of a protein solution at a concentration of 1 mg/mL. Following the injection of protein, measurements were recorded as the buffer continued to flow over the sensor surface for 2 h. The reported values are an average of 3 separate sets of experiments using freshly prepared SAMs. The response signal arises from changes in the resonance angle of light reflected from the Au surface. As the protein solution flows through the cell, it interacts with the surface through binding and disassociation, leading to a change in the angle of reflection of light from the Au surface. The SPR technique is based on the Kretschmann theory.<sup>40</sup> A sensorgram is then generated as a response to changes in the refractive index at the interface of the surface. After exposing the surface to the protein solution, PBS is allowed to flow again to wash away any unbound or weakly attached protein on the surface. The complete removal of protein solution from the cell is reflected as a decrease in signal in the curve. The difference between the ground response and the final response is represented as  $\Delta\text{RU}$ .

### 2.2.7. QCM Measurements

Frequency measurements ( $f$ ) of functionalized QCM sensors were performed using a Gamry eQCM with a continuous driving voltage to the piezoelectric-crystal oscillator, which simultaneously collects parallel and series measurements on the crystal. Each QCM crystal was allowed to reach equilibrium, once the driving voltage was applied from the oscillator. The frequency change was normalized by taking readings of the bare gold sensor, after SAM formation, and then again after protein exposure. The reported values are an average of the resonant frequency after stabilization. The QCM sensor is a thin

piezoelectric crystal that is sandwiched between two Au plates acting as electrodes. This allows for voltage to be applied, which generates an alternating electric field on each side of the crystal. The alternating electric fields create a mechanical shear wave modulate and a vibrational motion, which is the resonance frequency of the crystal. The piezoelectric quartz crystal in the QCM sensor is excited to oscillate near its resonant frequency. Any mass loss or addition will result in a change of this resonance frequency. A decrease in the resonant frequency ( $\Delta f$ ) is observed when material adheres to the surface of the sensor. The value of  $\Delta f$  is proportional to the change in mass ( $\Delta m$ ) as evaluated using the Sauerbrey equation (Equation 2.1).<sup>41-43</sup>

$$\Delta m = -C_f \Delta f \quad (2.1)$$

The quantification of the mass loading on the surface of the QCM crystal was determined with Equation 2.1, where  $C_f$  (the mass sensitivity constant) is  $-226 \mu\text{g}/(\text{Hz cm}^2)$  for the 10 MHz AT-cut QCM crystal.<sup>43</sup>

### **2.2.8. AFM Imaging and Measurements**

All AFM images were obtained using an Agilent 5000 atomic force microscope. Imaging was performed in air using acoustic (AC) mode and NTESPA cantilevers. All images were processed using the software Gwyddion. Statistical evaluations of the surface were completed using Gwyddion.

## **2.3. Results and Discussion**

Characterizing the performance of SAM's can be approached from many points of view. In the past, common and easily accessible methods such as ellipsometry were often employed and those data reported in publications. However, we were interested

in using other additional biophysical methods to understand the robustness of our characterization and to address potential pitfalls in the confounding of mass absorbance data, for which we were primarily interested in, with other phenomenon driven by light scattering. QCM and SPR both provide access to measurements that are highly correlated to mass absorbance to the surface, and so we report in Figure 2.3 a synopsis of all three data sets; ellipsometry, SPR, and QCM.

We also envisioned an initial, but not exhaustive, selection of environments to test the SAMs. These included proteins with a range of properties and applications. Proteins evaluated in this study were selected using several criteria including isoelectric point, size, molecular weight, hydrophobicity, and applications. The set of proteins include BSA, a widely used, stable, and hydrophobic protein;<sup>44</sup> fibrinogen, a widely used large and sticky protein;<sup>45</sup> lysozyme, a small and positively-charged protein;<sup>46</sup> and protamine, which was selected for its size, applications, and isoelectric point (pI). Table 2.1 provides a description of the properties of the selected proteins. The protein solutions consist of a phosphate buffer solution (PBS), since it is well tolerated by the selected proteins. Further, to remove any anomalies in protein adhesion that might be caused by the buffer system,<sup>47,48</sup> we measured changes associated with the buffer exposed on the film. In addition, we studied the non-specific adsorption of the selected proteins on the surfaces, measured qualitatively the surface coverage, and quantitatively measured the amount of protein on the surface of the SAMs. The analytical techniques selected to obtain the desired information were ellipsometry, surface plasmon resonance (SPR), electrochemical quartz crystal microbalance (QCM), and atomic force microscopy (AFM).

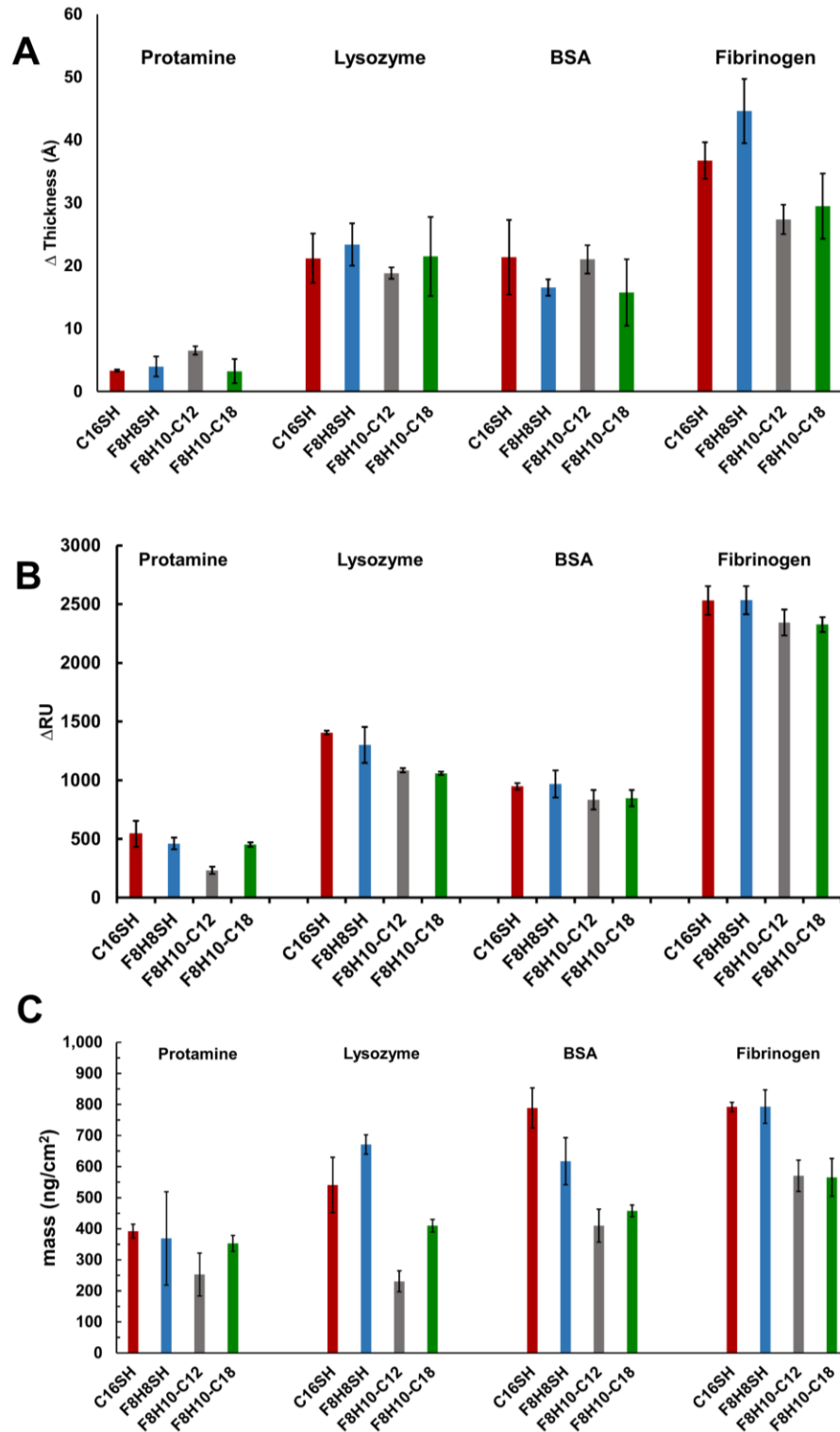


**Figure 2.3.** (A) Inferred changes in the thickness from ellipsometry of the SAMs generated from **C16SH**, **F8H8SH**, **F8H10-C12**, and **F8H10-C18** after exposure to solutions of protamine, lysozyme, BSA, and fibrinogen. (B) SPR data (C) QCM Mass loading calculations.

**Table 2.1.** Physical Properties of Proteins Examined in this Investigation

<b>Protein</b>	<b>Protamine<sup>49</sup></b>	<b>Lysozyme<sup>46</sup></b>	<b>BSA<sup>44</sup></b>	<b>Fibrinogen<sup>45</sup></b>
<b>Molecular Weight</b>	4 KDa	14 KDa	55 KDa	340 KDa
<b>Shape</b>	Spherical	Stubby Prolate Ellipsoid	Prolate Ellipsoid <sup>a</sup>	Cylindrical <sup>b</sup>
<b>Size (dia.)</b>	5 Å	18 Å <sup>c</sup>	140 × 40 × 40 Å	450 × 90 Å
<b>pI</b>	12.1	11.1	4.8	5.7
<b>Application</b>	Insulin	Cell	Blood	Muscle/Tissue

<sup>a</sup> where a=b<c<sup>b</sup> with round ends<sup>c</sup> diameter

An overall picture emerged that indicates that partially fluorinated spiroalkanedithiol adsorbates can reduce the non-specific absorption of proteins. This was most strongly demonstrated in the measurements of fibrinogen across all of the measurement regimes. The largest change in thickness as measured by ellipsometry was obtained from exposure of the SAMs to the largest molecular weight protein, fibrinogen at 340 KDa. The observed changes in thickness values were  $37 \pm 3$ ,  $45 \pm 11$ ,  $27 \pm 2$ , and  $30 \pm 5$  Å for **C16SH**, **F8H8SH**, **F8H10-C12**, and **F8H10-C18**, respectively. These observations were collaborated from both the SPR and QCM data. The SPR data also is consistent for fibrinogen where the data;  $2531 \pm 122$ ,  $2533 \pm 119$  ΔRU for **C16SH** and **F8H8SH** trends downward to  $2327 \pm 63$ ,  $2344 \pm 110$  ΔRU with the **F8H10-C18** and **F8H10-C12** SAM surfaces. Likewise, the calculated QCM values indicated higher values of increased mass after protein exposure for fibrinogen which are  $792 \text{ ng/cm}^2$ ,  $793 \text{ ng/cm}^2$

for **C16SH** and **F8H8SH**, but better performance with only an increased mass of 565 ng/cm<sup>2</sup>, and 571 ng/cm<sup>2</sup> for **F8H10-C18** and **F8H10-C12** respectively.

### 2.3.1. *In situ* Analysis of Protein Adhesion Using SPR Spectroscopy

Surface plasmon resonance spectroscopy (SPR) allows for an effortless means to monitor the *in situ* interaction of proteins with surfaces. Therefore, SPR spectroscopy was used to probe changes in the response units, which correlates to the amount of nonspecific adsorption of proteins to the SAM surfaces. A larger amount of response units indicates more material on the surface. Figure 2.4 displays sensorgrams that report the change in response for the interactions between each of the selected proteins and the SAMs, while Table 2.2 shows the numerical calculation of the change in response units over time ( $\Delta$ RU).

**Table 2.2.** The  $\Delta$ RU for SAMs after Exposure to 300  $\mu$ L Injection of 1 mg/mL Protein Solution

<b>Adsorbate</b>	<b>Protamine <math>\Delta</math>RU</b>	<b>Lysozyme <math>\Delta</math>RU</b>	<b>BSA <math>\Delta</math>RU</b>	<b>Fibrinogen <math>\Delta</math>RU</b>
<b>C16SH</b>	544 $\pm$ 110	1407 $\pm$ 16	948 $\pm$ 28	2531 $\pm$ 122
<b>F8H8SH</b>	461 $\pm$ 49	1302 $\pm$ 153	968 $\pm$ 116	2533 $\pm$ 119
<b>F8H10-C12</b>	233 $\pm$ 30	1084 $\pm$ 18	833 $\pm$ 84	2344 $\pm$ 110
<b>F8H10-C18</b>	453 $\pm$ 19	1059 $\pm$ 14	847 $\pm$ 69	2327 $\pm$ 63

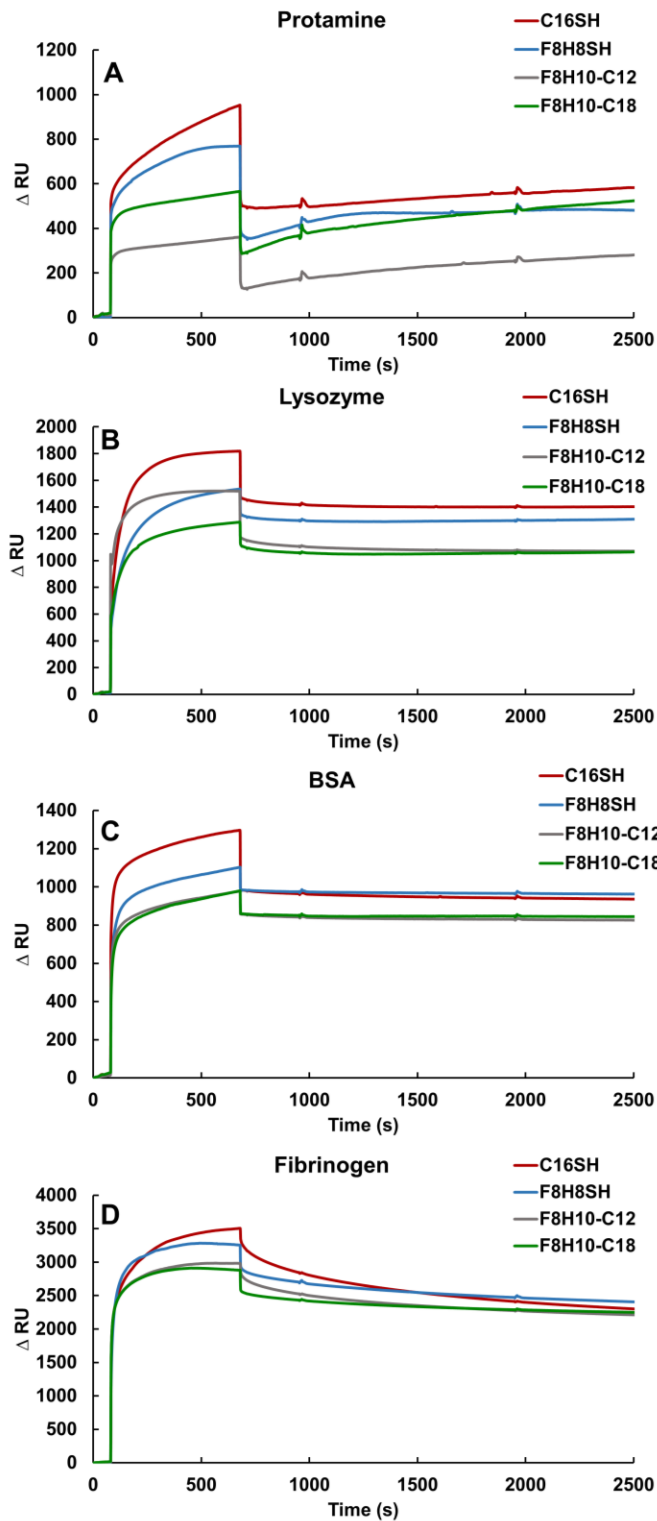


**Figure 2.4.** SPR sensorgrams of the SAMs exposed to (A) protamine, (B) lysozyme, (C) BSA, and (D) fibrinogen. Protein solutions were prepared at a concentration of 1 mg/mL in a PBS buffer solution.

The SAMs derived from **C16SH** and **F8H8SH** consistently absorbed a larger amount of protein, while the SAMs derived from **F8H10-C12** and **F8H10-C18** consistently adsorbed a smaller amount of protein, in each case as measured by SPR. Regardless of the protein interacting with the surface, the **C16SH** adsorbates, containing a hydrophobic surface; and therefore, interacting more with the proteins, generates a larger  $\Delta$ RU.<sup>50</sup> For the **F8H8SH** SAM, the alkane portion of the structure generates a well ordered film, while the partially fluorinated portion decreases the dispersive forces, when the number of fluorocarbons is greater than a five, resulting in hydrophobic surface.<sup>27</sup> Furthermore, fluorinated surfaces also exhibit low surface energies, which renders the surface anti-adhesive towards non-fluorinated materials.<sup>11</sup> The hydrophobicity and low surface energy of the fluorinated surface results in non-favorable interactions with the proteins (i.e., repulsive interaction) when compared to the **C16SH** SAM, as noted with the trend. The only exception to the trend was the charged proteins, protamine and lysozyme. In this case, the charge works in favor of the hydrophobic surface, and since the protein and the surface do not have opposite charges, there is less adsorption compared to the BSA and fibrinogen, which contains a neutral surface.<sup>50</sup>

The trends in the  $\Delta$ RUs of the SAMs derived from the SADT adsorbates correspond to a lower amount of adsorption of the proteins compared to their single-chain counterparts, due to their lower  $\Delta$ RU. Specifically, protamine produced  $\Delta$ RU values of 544, 461, 233, and 453 for SAMs generated from **C16SH**, **F8H8SH**, **F8H10-C12**, and **F8H10-C18**, respectively. With the exception of protamine, the SADT adsorbates, **F8H10-C12** and **F8H10-C18**, responded within the standard deviation for the respective proteins, regardless of adsorbate structure. In the case of protamine, the small size of the

protein in combination with the more loosely packed chains in the **F8H10-C18** adsorbate, compared to the **F8H10-C12**, is likely the reason for a larger difference than the standard deviation values. Overall, the SAMs generated from the SADT adsorbates (**F8H10-C12** and **F8H10-C18**) exhibited greater protein resistance than the monodentate analogs (**C16SH** and **F8H8SH**). In the case of **F8H10-C12**, greater protein adhesion is likely due to the ability of the helical fluorinated chains (van der Waals diameter of  $\sim 5.6\text{\AA}$ ) to pack above the well-packed trans-extended alkyl chains (van der Waals  $\sim 4.2\text{\AA}$ ).<sup>22,51-53</sup>

Inclusion of the secondary alkyl chain in the architecture of the adsorbate does not restrict the fluorinated chains to the packing constraints typically observed in the corresponding monodentate SAM (**F8H8SH**).<sup>36</sup> Furthermore, the branched nature of the SADT adsorbates have been shown to influence the ordering of the films by generating loosely packed SAMs.<sup>36</sup> Typically, for hydrocarbon-based SAMs the crystalline nature of the film increases as the length of the hydrocarbon chain is extended.<sup>54-56</sup> However, for the SADT SAMs, the longer hydrocarbon chain found in the **F8H10-C18** adsorbate was found to be detrimental to film order, due to greater unfavorable interactions between the two phase incompatible groups that resulted in more loosely packed chains compared to the SAMs generated from **F8H10-C12**.<sup>36</sup> Therefore, it is likely that for the SAMs generated from the SADT adsorbates, both the greater lateral spacing provided by the branched architecture of the adsorbate and the loose packing of the film allow for enhanced protein resistance, compared to the monodentate analogs.

The size of the protein used does have an effect on the observed relative change in response. Table 2.2 shows that  $\Delta\text{RU}$  increases from  $\sim 300$  RU in smaller proteins (e.g., protamine) to  $\sim 2500$  RU for larger proteins (e.g., fibrinogen), and this trend is easily

noted in the graphically presented  $\Delta$ RU values found in Figure 2.3. The  $\Delta$ RU correlates to the amount of material interacting and binding to the surface of the SAM attached to the gold substrate. Larger molecular weight proteins would generate a greater response signal, compared to a smaller molecular weight protein, in a molecule to molecule comparison. Thus, an increase in response units is expected with respect to the increase in molecular weight.

Interesting to note is the role the charge of the protein may play in the observed adsorption, aside from the size of the protein, the charge on the protein may lead to areas or patches of hydrophobic and hydrophilic character on the protein surfaces yielding higher adhesion to the SAM surfaces. This phenomenon is most notable with the lower molecular weight lysozyme (14 KDa) compared to the higher molecular weight BSA (55 KDa), and the higher  $\Delta$ RU exhibited by lysozyme over that of BSA. A key difference is the positively charged lysozyme surface over the generally neutral BSA surface.<sup>46,49</sup> It is also important to note that the surface energy of the SAMs is another likely contributing factor to the ability of the SAM to resist protein adhesion. For example, the higher surface energy of the **C16SH** SAM (20.3 mJ/m<sup>2</sup>)<sup>36</sup> compared to the **F8H8SH** SAM (8.88 mJ/m<sup>2</sup>)<sup>36</sup> exemplifies the aforementioned observations. Similarly, the **F8H10-C12** SAM has a lower surface energy (11.5 mJ/m<sup>2</sup>)<sup>36</sup> than the **F8H10-C18** SAM (15.8 mJ/m<sup>2</sup>).<sup>36</sup>

### 2.3.2. *Ex situ* Analysis of Protein Adhesion Using QCM

Taking advantage of the sensitivity of QCM sensors to mass changes allows for the ability to quantify the amount of protein adhered to the surface. Figure 2.5 shows the frequency change,  $-\Delta f$ , as a function of time; note, the data reported is an average of 3

independent trials for each surface. A decrease in frequency, compared to the bare QCM sensor, is indicative of mass adsorbed onto the surface, the SAM, or adhered protein. The QCM technique is used as a complementary study to the SPR *in situ* technique. The QCM study conducted *ex situ* and therefore generates a response known as a dry mass loading of the surface without the hydration layer which should result in lower readings when compared to the hydrated interaction during an *in situ* study but with the same trends as noted with the SPR technique.<sup>57-60</sup> Figure 2.5 shows a greater  $\Delta f$  after exposure to protein solutions for films generated from **C16SH** and **F8H8SH** when compared to the films generated from **F8H10-C12** and **F8H10-C18**, corresponding to a greater mass loading for the crystals coated with the former two adsorbates. The mass loading of each protein on the surfaces was calculated using Equation 2.1 and is shown in Figure 2.3 and Table 2.3.

**Table 2.3.** Calculations of Mass loading for SAMs derived from **C16SH**, **F8H8SH**, **F8H8-C12**, and **F8H8-C18** after 1 h exposure to 1 mg/mL of protein in PBS solution.

Adsorbate	Mass Loading – ng/cm <sup>2</sup>			
	Protamine	Lysozyme	BSA	Fibrinogen
<b>C16SH</b>	392 ± 23	541 ± 89	789± 64	792 ± 10
<b>F8H8SH</b>	369 ± 150	671 ± 31	618± 76	793 ± 54
<b>F8H10-C12</b>	253 ± 69	231 ± 34	410 ± 53	571 ± 50
<b>F8H10-C18</b>	353 ± 25	410 ± 21	458 ± 19	565 ± 61

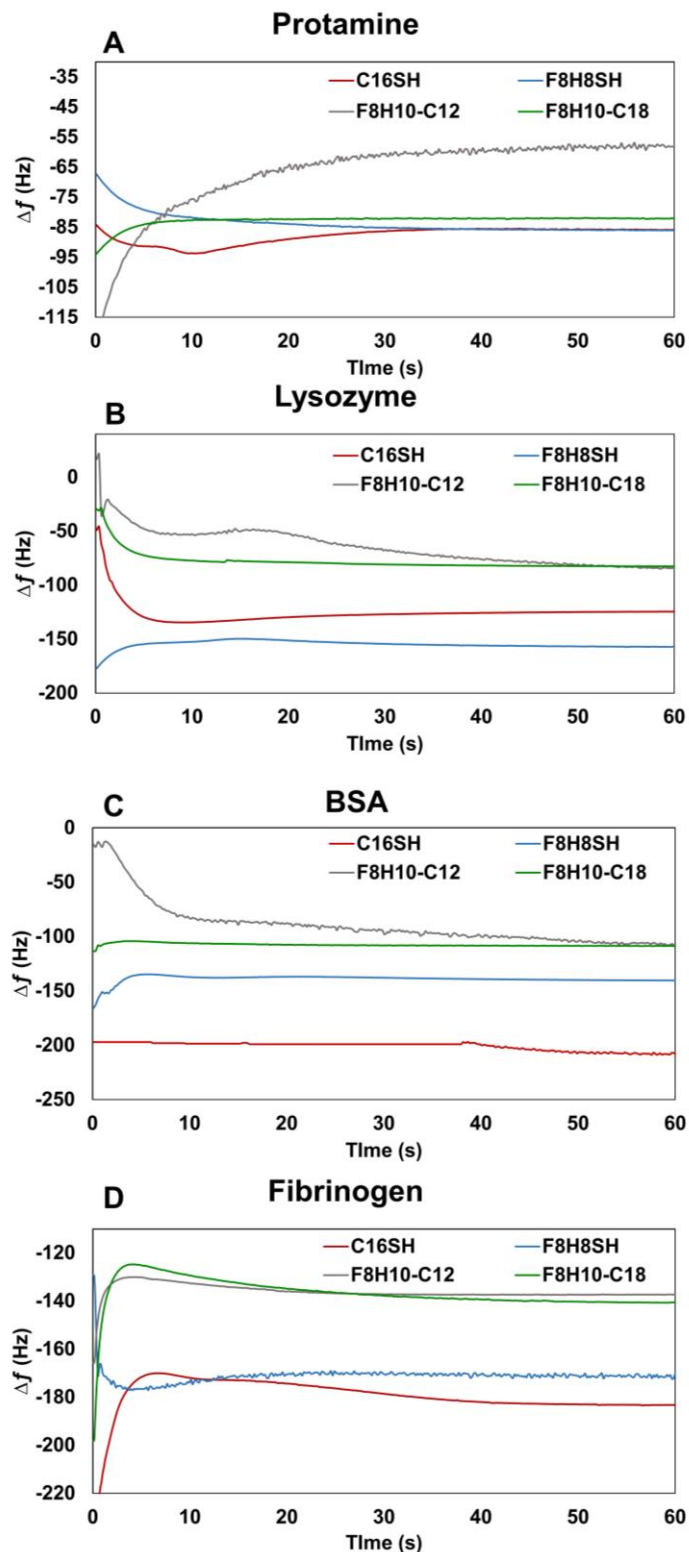


**Figure 2.5.** Change in frequency vs. time for SAMs derived from **C16SH**, **F8H8SH**, and **F8H10-C12**, and **F8H10-C18** after 1 h exposure to 1 mg/mL of protein in PBS solution: (A) protamine, (B) lysosome, (C) BSA, and (D) fibrinogen.

When the adsorbates are exposed to a protein, for example protamine, **C16SH** observed a mass increase of 392 ng/cm<sup>2</sup>, **F8H8SH** was 369 ng/cm<sup>2</sup>, compared to **F8H10-C18** at 353 ng/cm<sup>2</sup>, and **F8H10-C12** with the least amount of 253 ng/cm<sup>2</sup>. As expected, after exposure to the protein the trend indicated more mass loading for the hydrophobic **C16SH**, and the **F8H8SH** monothiol adsorbates, but the **F8H8SH** containing lower surface energy showed a slightly lower amount of protein adhered, with the exception of lysozyme. In the case of lysozyme, the **F8H8SH** adsorbate indicated a larger mass loading of the surface compared to the **C16SH** monothiol due to greater interactions from the charged protein surface that generates areas with greater attraction to the nature of the **F8H8SH** adsorbate when lacking the hydration layer. When the monothiol analogs are compared to the SADT adsorbates, **F8H10-C12** and **F8H10-C18**, the SADTs contained less mass adhered than the monothiol analogs, but **F8H10-C18** contained more mass and is likely due to the more loosely packed chains found in **F8H10-C18**. The overall trend for the mass loading values increase as the size of the protein increases but decreases in adhered mass for the SADTs, **F8H10-C12** and **F8H10-C18**, when it is compared to **C16SH** and **F8H8SH**. This is in correlation with the SPR data.

Figure 2.3 shows that the mass loading is proportional to the size of the proteins, with protamine being the smallest protein having a smaller  $\Delta f$  and fibrinogen being the largest protein, and having the largest  $\Delta f$ . The trend observed shows that regardless of the type of protein, the SADT adsorbates, **F8H10-C12** and **F8H10-C18**, have lower mass loading compared to the **C16SH** and the **F8H8SH** SAMs. Consistently, the SADTs, **F8H10-C12** and **F8H10-C18**, have a smaller change in frequency compared to **C16SH** and **F8H8SH**. Specifically, **F8H10-C12** shows slightly more protein resistance, than

**F8H10-C18**, and this is likely due to the more loosely packed chains found in the **F8H10-C18** adsorbate. QCM measurements for BSA were 798 ng/cm<sup>2</sup>, 618 ng/cm<sup>2</sup>, 458 ng/cm<sup>2</sup> and 410 ng/cm<sup>2</sup> for **C16SH**, **F8H8SH**, **F8H10-C18**, and **F8H10-C12**, respectively. When compared to the SPR data, the change might be expected to be larger, but there is more interaction with the hydration layer for the *in situ* interactions, compared to the dry loading from the *ex situ* interactions of the QCM technique. However, the SADTs, **F8H10-C12** and **F8H10-C18**, still resist more protein than the **F8H8SH** and **C16SH** SAMs, even in the *ex situ* studies.

Regardless, exposure of the SAM coated QCM crystal surfaces to the protein solutions (protamine, lysozyme, BSA, and fibrinogen) indicate a decrease in  $\Delta f$ , thus correlating to the trend observed in the SPR data. The mass loading of the QCM sensor further supports the SADTs, **F8H10-C12** and **F8H10-C18**, as being more protein resistant than the single chain monothiol analogs. The calculated change in mass by the observed change in frequency is indicative that the design of the molecule, where the partially fluorinated helical chain is able to maximize van der Waals forces, and provide greater lateral spacing resulting from the branched architecture of the adsorbate, generating loosely packed films, which better resists protein adhesion.<sup>36</sup>

### 2.3.3. Ellipsometric Thickness Measurements

Formation of the monolayers was confirmed by thickness measurements using ellipsometry on all tested substrates. The thickness of the SAMs, are consistent with those previously reported for all adsorbates and can be found in Table 2.4.<sup>38</sup> Notably, thickness

values obtained on all substrates, prior and after protein exposure, exhibited similar values; the values presented herein are measurements taken on the evaporated gold surfaces. Figure 2.3 graphically presents the changes in thickness after protein exposure while Table 2.5 lists the values. For the smallest protein in the series, protamine, ellipsometry measurements appear to be similar on all of the SAM surfaces --  $3 \pm 1$ ,  $4 \pm 2$ ,  $3 \pm 2$  Å for **C16SH**, **F8H8SH**, and **F8H10-C18**, respectively -- with the exception of **F8H10-C12**,  $7 \pm 1$  Å. AFM investigations discussed later indicate variations in surface roughness which can impact ellipsometric measurements as surface roughness is increased, and it is noted that **F8H10-C12** falls within the standard deviation of the other SAM surfaces. Exposure of the SAMs to lysozyme, a slightly larger protein, also resulted in similar measurements for all of the SAMs:  $21 \pm 4$ ,  $23 \pm 3$ ,  $19 \pm 1$ , and  $22 \pm 6$  Å for the **C16SH**, **F8H8SH**, **F8H10-C12**, and **F8H10-C18**, respectively.

A similar trend was also observed after exposure with BSA motivating further analysis of surface roughness with AFM. The largest change in thickness as indicated by ellipsometry measurements was obtained from exposure of the SAMs to the largest molecular weight protein, fibrinogen (340 KDa), compared to the aforementioned proteins analyzed in the study. In the observed changes in thickness, the values were  $37 \pm 3$ ,  $45 \pm 11$ ,  $27 \pm 2$ , and  $30 \pm 5$  Å for **C16SH**, **F8H8SH**, **F8H10-C12**, and **F8H10-C18**, respectively. Important to note is the scattering of the SAM surfaces exhibited after protein exposure; this is noted with the large error exhibited in the data. The greater scatter can be attributed to an increase in surface roughness from the protein adhered to the surface, which was confirmed by AFM measurements (*vide infra*). Ellipsometric measurements with

respect to the SAMs exposed to fibrinogen are indicative of a possible improvement of the **F8H10-C12** and the **F8H10-C18** SAMs over the **F8H8SH** and the **C16SH** SAMs. Fibrinogen is a large molecular weight protein with a pI of 5.7, which is a neutral protein (i.e., not charged). The protein lacks a charge; therefore, having less interaction with the surface, which can lead to low protein adsorption on the surface, but the increased molecular weight would increase the thickness in comparison to the other smaller molecular weight proteins.

**Table 2.4.** Ellipsometric Thickness Values of SAMs Used to Confirm SAMs Formation

<b>Adsorbate</b>	<b>Thickness (Å)</b>
<b>C16SH</b>	$20 \pm 1$
<b>F8H8SH</b>	$17 \pm 1$
<b>F8H10-C12</b>	$16 \pm 1$
<b>F8H10-C18</b>	$21 \pm 1$

**Table 2.5.** Change in Ellipsometric Thickness Values of the SAMs after Exposure to 1mg/mL of Protein Solution in PBS Buffer

<b>Δ Thickness (Å)</b>	<b>C16SH</b>	<b>F8H8SH</b>	<b>F8H10-C12</b>	<b>F8H10-C18</b>
<b>Protamine</b>	$3 \pm 1$	$4 \pm 2$	$7 \pm 1$	$3 \pm 2$
<b>Lysozyme</b>	$21 \pm 4$	$23 \pm 3$	$19 \pm 1$	$22 \pm 6$
<b>BSA</b>	$21 \pm 6$	$17 \pm 1$	$21 \pm 2$	$16 \pm 5$
<b>Fibrinogen</b>	$37 \pm 3$	$45 \pm 11$	$27 \pm 2$	$30 \pm 5$

#### 2.3.4. Evaluation of Surface Topography Using AFM

Atomic force microscopy has been used extensively to image biological materials and SAMs to determine surface topography resulting from interactions.<sup>61-67</sup> Therefore, AFM was employed to image surface topography of each surface to determine if there are any distinct differences in the surface patterning after exposure to the protein solution. The AFM results of the topography imaging of the **C16SH**, **F8H8SH**, **F8H10-C18**, and **F8H10-C12** surfaces are shown for protamine in Figure 2.6, lysozyme in Figure 2.7, BSA in Figure 2.8, and fibrinogen in Figure 2.9. Each figure is a  $5\ \mu\text{m} \times 5\ \mu\text{m}$  and a  $1\ \mu\text{m} \times 1\ \mu\text{m}$  of the SAMs exposed to the specified protein. The AFM imaging of these samples indicates that the protein adsorbed to the sensor might be distinguishably identified on the surface as indicative of the different patterns displayed.<sup>63,66,68,69</sup> For instance, the images of **F8H8SH** exposed to protamine (Figure 2.6B), lysozyme (Figure 2.7B), BSA (Figure 2.8B), and fibrinogen (Figure 2.9B) exhibit different patterns. By simple comparison, surface patterns exposed to protamine have less material and increases with protein size where surfaces exposed to fibrinogen have more material on the surfaces. Additional statistical evaluation of the patterning on the surface may result in quantitative measurements to confirm more material attached to the surfaces to correlate with the previous analytical techniques and provide additional insight into the interactions of the proteins with the adsorbates.

Further analysis of the surface images using Gwyddion allowed for the arithmetic average ( $R_a$ ) and the root mean square (RMS) of the surface roughness to be determined, which are the simplest calculations to complete; therefore, they are the most commonly used values with respect to surface roughness measurements. Analysis of the

surface roughness, which considers the heights of the peaks and valleys across the area of the surface being imaged, supplies information about the patterning of the material attached to the surface and would likely increase as more material is attached to the surface. The values are graphically presented in Figure 2.10 giving additional insight into the surface topography distinctions. Table 2.6 and Table 2.7 contains the numerical values with the standard deviation for  $R_a$  and  $R_{ms}$ , respectively.

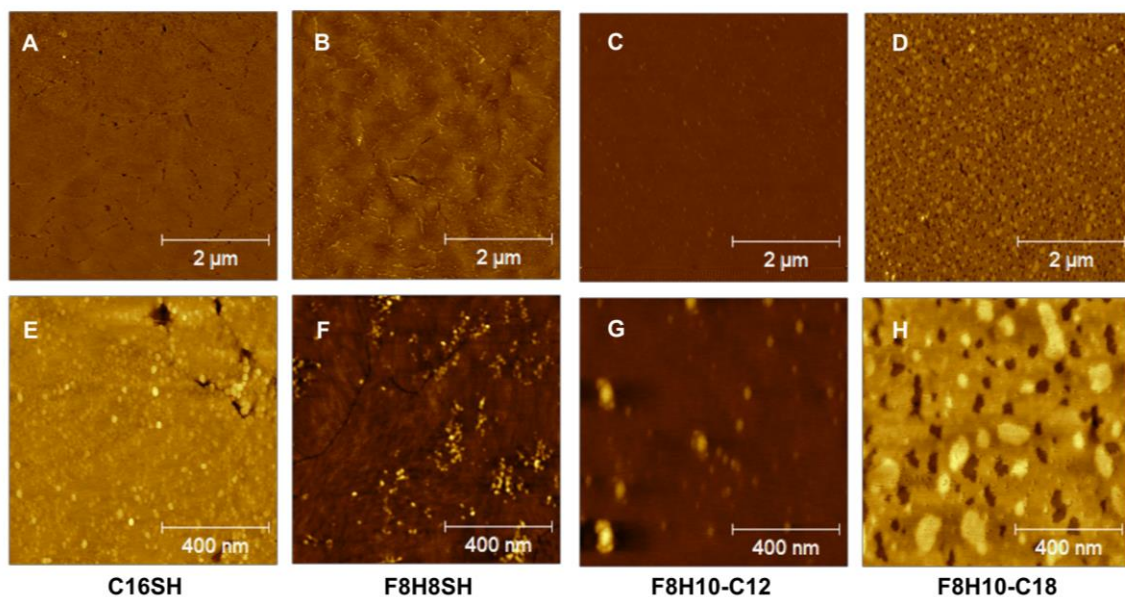


**Figure 2.6.** Topography after exposure to protamine for (A, E) **C16SH**, (B, F) **F8H8SH**, (C, G) **F8H10-C12**, and (D, H) **F8H10-C18** at  $5\ \mu\text{m} \times 5\ \mu\text{m}$  (top) and  $1\ \mu\text{m} \times 1\ \mu\text{m}$  (bottom).

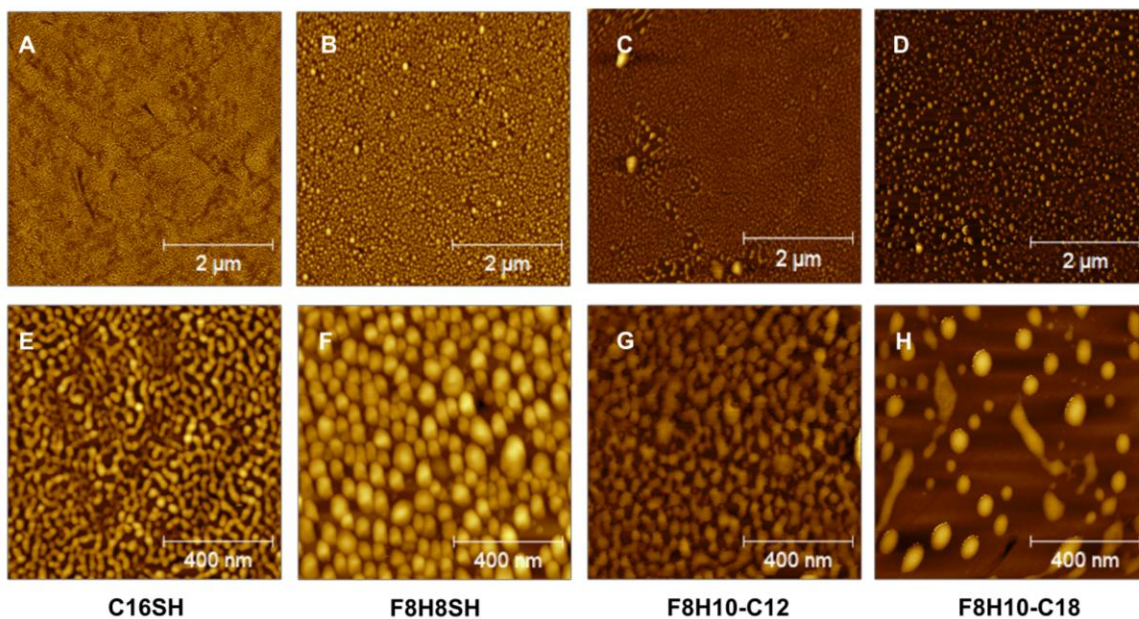


**Figure 2.7.** Topography after exposure to lysozyme for (A, E) **C16SH**, (B, F) **F8H8SH**, (C, G) **F8H10-C12**, and (D, H) **F8H10-C18** at  $5\ \mu\text{m} \times 5\ \mu\text{m}$  (top) and  $1\ \mu\text{m} \times 1\ \mu\text{m}$  (bottom).

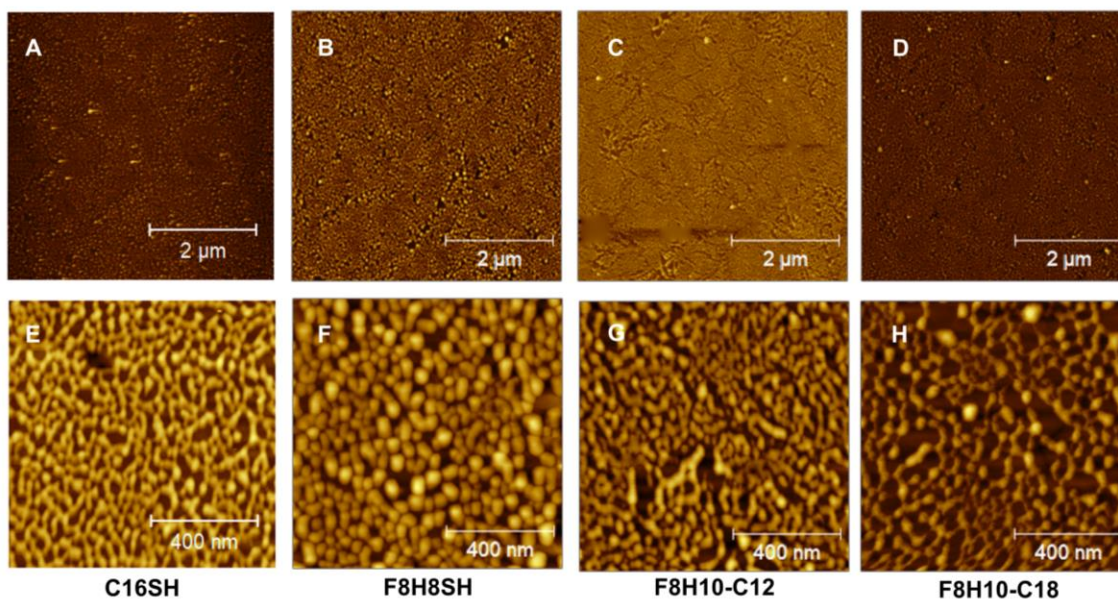


**Figure 2.8.** Topography after exposure to BSA for (A, E) **C16SH**, (B, F) **F8H8SH**, (C, G) **F8H10-C12**, and (D, H) **F8H10-C18** at  $5\ \mu\text{m} \times 5\ \mu\text{m}$  (top) and  $1\ \mu\text{m} \times 1\ \mu\text{m}$  (bottom).

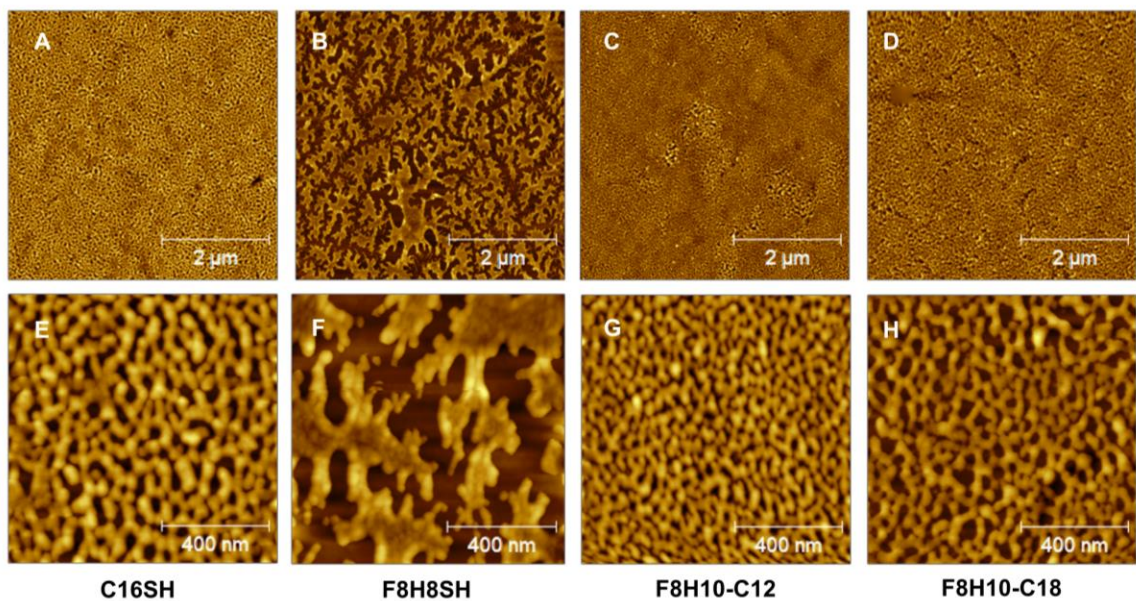


**Figure 2.9.** Topography after exposure to fibrinogen for (A, E) **C16SH**, (B, F) **F8H8SH**, (C, G) **F8H10-C12**, and (D, H) **F8H10-C18** at  $5 \mu\text{m} \times 5 \mu\text{m}$  (top) and  $1 \mu\text{m} \times 1 \mu\text{m}$  (bottom).

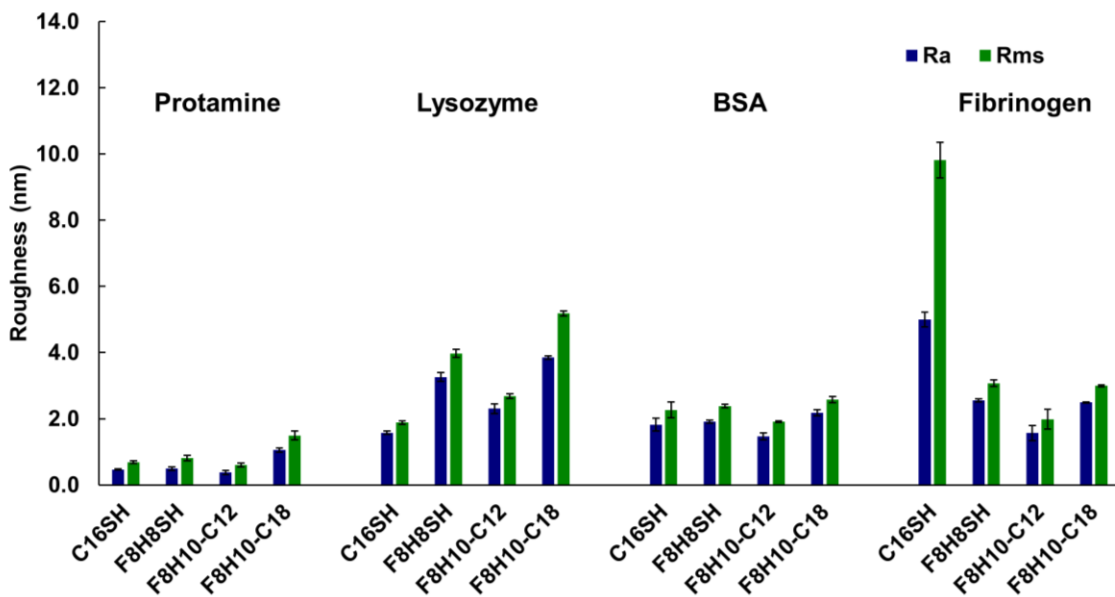


**Figure 2.10.** Comparison of average roughness ( $R_a$ ) and root mean square ( $R_{ms}$ ) values for each of the SAMs (**C16SH**, **F8H8SH**, **F8H10-C12**, and **F8H10-C18**) after exposure to protamine, lysozyme, BSA, and fibrinogen, respectively.

Apparent from Figure 2.10, the larger proteins produce a rougher surface, compared to the smaller proteins. As expected, the surface roughness increases with the larger proteins. It is not clear, however, that roughness correlates to the amount of material on the surface, since Figure 2.10 does not directly reveal that **C16SH** and **F8H8SH** have a greater roughness compared to the **F8H10-C12** and **F8H10-C18** SAMs. However, **F8H10-C18** is higher than **F8H10-C12**, which is expected, indicating more material adhered to the **F8H10-C18** surface compared to the **F8H10-C12** and is likely due to the more loosely packed chains of the **F8H10-C18** adsorbate. Since the surface roughness measurement is an average value of the height maximum and minimum values, multiple distinct surfaces can provide the same values, yet have different patterning on the surface; further analysis of the statistical information of the surface might prove beneficial. Additional analysis of height distribution density plots gives insightful clarification of the topographies of the surfaces, as it provides a histogram of the surface heights across the imaged area, which can then be compared from surface to surface to determine material adhered to the surface; the height density distributions provide clarification to the differences observed in the  $R_a$  and  $R_{ms}$  values.

**Table 2.6.** Calculated  $R_a$  Values for the Surfaces in this Study

<b>Protein</b>	<b><math>R_a</math> (nm)</b>			
	<b>C16SH</b>	<b>F8H8SH</b>	<b>F8H10-C12</b>	<b>F8H10-C18</b>
<b>Protamine</b>	$1.47 \pm 0.42$	$0.48 \pm 0.07$	$1.08 \pm 0.19$	$1.62 \pm 0.14$
<b>Lysozyme</b>	$1.30 \pm 0.04$	$0.90 \pm 0.31$	$0.99 \pm 0.13$	$2.73 \pm 0.29$
<b>BSA</b>	$1.87 \pm 0.01$	$0.97 \pm 0.15$	$1.21 \pm 0.27$	$3.38 \pm 0.36$
<b>Fibrinogen</b>	$3.88 \pm 0.36$	$1.85 \pm 0.62$	$0.70 \pm 0.23$	$0.91 \pm 0.43$

**Table 2.7.** Calculated Rms Values for the Surfaces in this Study

Protein	Rms (nm)			
	C16SH	F8H8SH	F8H10-C12	F8H10-C18
Protamine	2.24 ± 0.66	0.88 ± 0.10	1.95 ± 0.49	2.17 ± 0.19
Lysozyme	1.65 ± 0.07	1.77 ± 0.65	1.33 ± 0.17	3.69 ± 0.48
BSA	2.20 ± 0.02	1.72 ± 0.30	1.93 ± 0.85	4.30 ± 0.68
Fibrinogen	4.74 ± 0.74	2.98 ± 0.10	1.05 ± 0.64	4.47 ± 0.62

The height distribution density plot for protamine (Figure 2.11A) indicates that **F8H8SH** and **C16SH** both have a higher degree of surface coverage, but the heights are ~10-20 nm and ~15 nm, respectively, which are slightly shorter than those of the **F8H10-C18**, ranging from ~15-20 nm, and **F8H10-C12**, ~18 nm. The increased  $R_a$  and Rms values for **F8H10-C18** result from the great variation in the height differences on the surface, ranging from ~10 nm to ~25 nm. The height distribution density plot for lysozyme (Figure 12.11B) helps to correlate the  $R_a$  and Rms values to the observed trends seen with the QCM and SPR studies. The **C16SH** surface has a range of 10-30 nm, but all heights have similar density coverage and less variation in the height change due to the broad curve. Comparatively, **F8H8SH** also has a higher height, but, since the curve is narrower, this leads to more areas having peaks at ~15 nm and not as many at the extremes of the distribution, which results in higher surface roughness. The curve for **F8H10-C18** has a very sharp peak at the ~10 nm range, with a low-density plot stretching to almost 20 nm.

The large difference in heights across the surface leads to an increase in roughness measurements, as observed in the  $R_a$  and Rms values in Figure 2.10. The peak heights are ~5 nm-15 nm for **F8H10-C12**, but it is again a broad peak which would result in lower

surface roughness measurements. The  $R_a$  and  $R_{ms}$  values for BSA were as expected. The height distribution density plot for BSA (Figure 2.11C) indicates that **F8H8SH** had a large range, ~8 nm- 25 nm, with 2 distinct heights at ~10 nm and ~17 nm. The large variation and greater height indicate more material adhered to the surface. **C16SH** also has a greater height, but the curve is narrower, leading to more areas having peaks around 18 nm and not as many at the extremes of the distribution, resulting in similar surface roughness, yet it is indicative of a great amount of material adhered to the surface. The **F8H10-C18** has the lowest surface density and shortest height ~12 nm for most of the surface density, but it continues to extend to 20 nm, compared to **F8H10-C12** which has a narrow peak ~5 nm-15 nm resulting in slightly lower  $R_a$  and  $R_{ms}$  values.

Lastly, fibrinogen height density plots indicate that there is a large range (~8 nm-30 nm) with a broad curve around ~20 nm for **C16SH**. **F8H8SH** holds two distinct height peaks around 10 nm and 20 nm, which is indicative of the image with the fractal pattern observed in the AFM surface topography, Figure 2.9B. The large variation in height would produce a higher surface roughness for both **C16SH** and **F8H8SH**. **F8H10-C18** yields a peak ~10 nm, yet it extends from ~5 nm-20 nm resulting in similar roughness to the **F8H8SH** SAM. The  $R_a$  and  $R_{ms}$  values for **F8H10-C12** produce a slightly similar yet smaller roughness, since the height is about 17 nm but is not as broad as the other surfaces when interacting with fibrinogen.

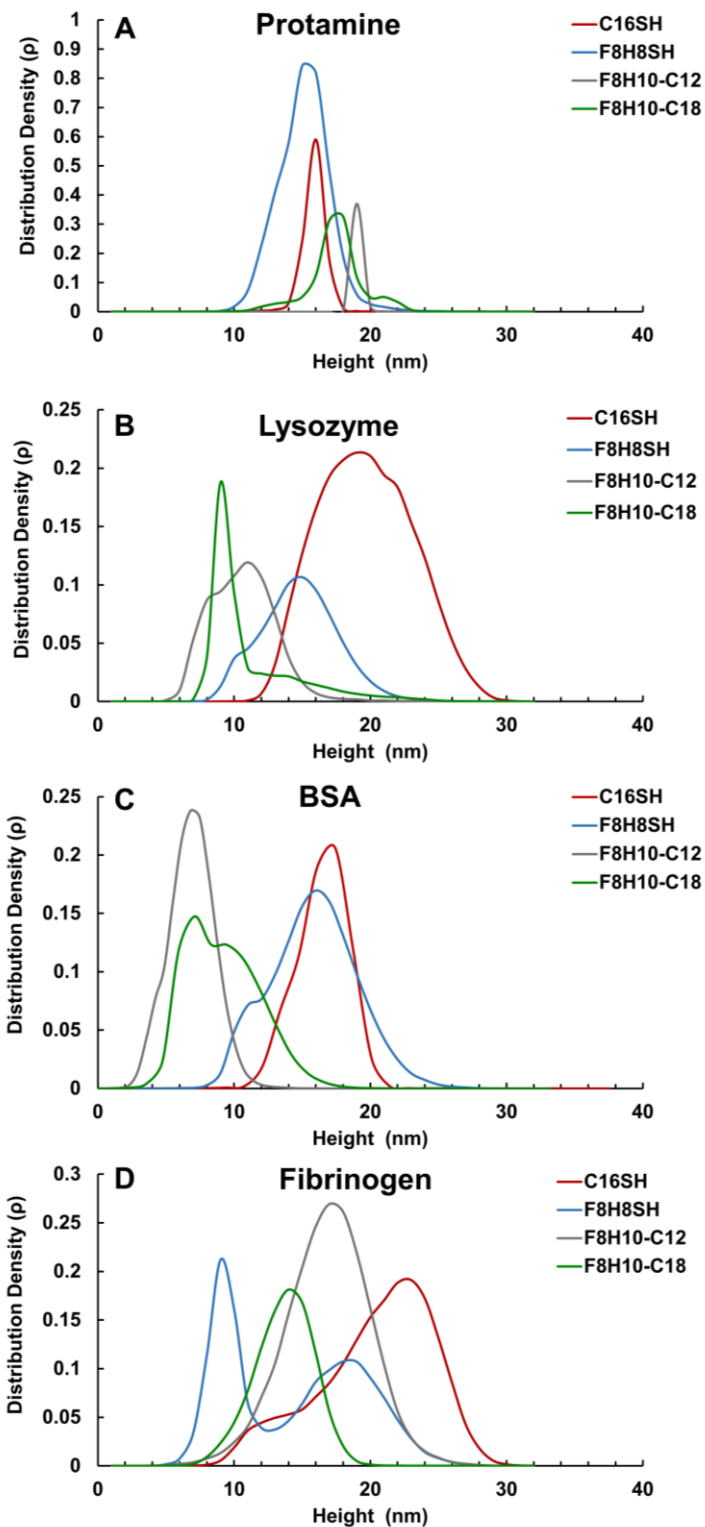


**Figure 2.11.** Distribution density plots for **C16SH**, **F8H8SH**, **F8H10-C12**, and **F8H10-C18** after exposure to (A) protamine, (B) lysozyme, (C) BSA, and (D) Fibrinogen determined from AFM images.

The resulting AFM images are indicative that surface topography is distinguishable among the various surfaces with the various proteins studied herein. Height distribution density plots are used to explain the variations observed in the  $R_a$  and  $R_{ms}$  values, and correlate with the observed topographies. The statistical analysis of the AFM imaging indicates that the **C16SH** and the **F8H8SH** monothiol analogs adhere more protein on their surfaces when compared to the SADTs, **F8H10-C12** and **F8H10-C18**, which is consistent with the trends observed with the other analytical techniques, except ellipsometry which was within standard deviations due to increased surface roughness. This further confirms that the structural design of the SADT adsorbates provides increased protein resistance by allowing for maximized van der Waals interactions between the chains of the dithiol adsorbates.

#### **2.4. Conclusions**

The anti-adhesive performance of SAMs generated from partially fluorinated spiroalkanedithols, **F8H10-C12** and **F8H10-C18**, as well as their monodentate analogs **C16SH** and **F8H8SH** was measured using a wide range of characterization techniques with proteins exhibiting a diverse range of properties. Protein properties such as size, charge, hydrophobicity, and biological fluid composition, and origin were used to provide a more holistic understanding of the resistance of the SAMs to protein adhesion. The experiments presented herein encompass typical standards for the evaluation of biofilm formation in anticipation of future application of these surface technologies. These might include systems ranging from medical devices used with different fluids or tissues, applications in food processing, marine implementations, as well as water handling systems in isolated

environments, such as space stations or off-shore ocean operations. These studies confirmed that biofilms are less prone to form on the **F8H10-C12** and **F8H10-C18** SAMs compared to SAMs derived from **C16SH** and the **F8H8SH**. The **F8H10-C12** and **F8H10-C18** SAMs exhibited greater protein resistance, likely due to the inclusion of the secondary alkyl chain in the structural design of the molecules that allows for loosely packed chains, when compared to the monothiol counterparts. SPR data consistently demonstrated improved performance for the **F8H10-C12** and **F8H10-C18** coated surfaces with a  $\Delta RU$  average of 210 which represents percent changes from 8% to 133% less protein, when compared to the monodentate analogs. Similarly the changes in  $ng/cm^2$  in QCM data averaged to 222, which represents an 11% to 134% less mass loading.

AFM studies suggest a means to image and quantify biofilm formation, which in our case the results were complimentary to the SPR and QCM data. Variation in measurement accuracy, using optical ellipsometry confounded some of the observed trends between the **F8H10-C12** and **F8H10-C18** surface when tested with BSA. A similar discrepancy was observed between the **F8H8SH** as compared to the **C16SH** surface when tested with fibrinogen, but overall it confirmed the general trends in BSA and fibrinogen. Protamine and lysozyme have smaller signals and may interact with the surfaces differently based on size and charge. These developed protocols using independent experimental measures from ellipsometry, QCM, SPR, and AFM provide robust characterization of biofilm formation on mixed SAMs interfaces, which indicates that SADT SAMs have better anti-fouling properties than SAMs derived from monodentate analogs.

## 2.5. References

- (1) Vaisocherová, H.; Zhang, Z.; Yang, W.; Cao, Z.; Cheng, G.; Taylor, A. D.; Piliarik, M.; Homola, J.; Jiang, S. Functionalizable Surface Platform with Reduced Nonspecific Protein Adsorption from Full Blood Plasma-Material Selection and Protein Immobilization Optimization. *Biosens. Bioelectron.* **2009**, *24*, 1924–1930.
- (2) Yebra, D. M.; Kiil, S.; Dam-Johansen, K. Antifouling Technology - Past, Present and Future Steps towards Efficient and Environmentally Friendly Antifouling Coatings. *Prog. Org. Coatings* **2004**, *50*, 75–104.
- (3) Park, K. D.; Kim, Y. S.; Han, D. K.; Kim, Y. H.; Lee, E. H. B.; Suh, H.; Choi, K. S. Bacterial Adhesion on PEG Modified Polyurethane Surfaces. *Biomaterials* **1998**, *19*, 851–859.
- (4) Banerjee, I.; Pangule, R. C.; Kane, R. S. Antifouling Coatings: Recent Developments in the Design of Surfaces That Prevent Fouling by Proteins, Bacteria, and Marine Organisms. *Adv. Mater.* **2011**, *23*, 690–718.
- (5) Schlenoff, J. B. Zwitteration: Coating Surfaces with Zwitterionic Functionality to Reduce Nonspecific Adsorption. *Langmuir* **2014**, *30*, 9625–9636.
- (6) De Nys, R.; Guenther, J. *The Impact and Control of Biofouling in Marine Finfish Aquaculture*; Woodhead Publishing Limited: Sawston, 2009.
- (7) Bacha, A.; Méghabar, R. Development of Coatings Marine Antifouling Based on Perfluorinated Surfactants Synthesis and Physicochemical Study. *J. Surf. Eng. Mater.*

*Adv. Technol.* **2014**, *4*, 87–97.

- (8) Jeon, S. I.; Lee, J. H.; Andrade, J. D.; De Gennes, P. G. Protein-Surface Interactions in the Presence of Polyethylene Oxide. I. Simplified Theory. *J. Colloid Interface Sci.* **1991**, *142*, 149–158.
- (9) Prime, K. L.; Whitesides, G. M. Self-Assembled Organic Monolayers: Model Systems for Studying Adsorption of Proteins at Surfaces. *Science (80-. )*. **1991**, *252*, 1164–1167.
- (10) Pujari, S. P.; Spruijt, E.; Cohen Stuart, M. A.; Van Rijn, C. J. M.; Paulusse, J. M. J.; Zuilhof, H. Ultralow Adhesion and Friction of Fluoro-Hydro Alkyne-Derived Self-Assembled Monolayers on H-Terminated Si(111). *Langmuir* **2012**, *28*, 17690–17700.
- (11) Zenasni, O.; Jamison, A. C.; Lee, T. R. The Impact of Fluorination on the Structure and Properties of Self-Assembled Monolayer Films. *Soft Matter* **2013**, *9*, 6356–6370.
- (12) Takenaga, M.; Jo, S.; Graupe, M.; Lee, T. R. Effective van Der Waals Surface Energy of Self-Assembled Monolayer Films Having Systematically Varying Degrees of Molecular Fluorination. *J. Colloid Interface Sci.* **2008**, *320*, 264–267.
- (13) Graupe, M.; Koini, T.; Wang, V. Y.; Nassif, G. M.; Colorado, R.; Villazana, R. J.; Dong, H.; Miura, Y. F.; Shmakova, O. E.; Lee, T. R. Terminally Perfluorinated Long-Chain Alkanethiols. *J. Fluor. Chem.* **1999**, *93*, 107–115.
- (14) Colorado, R.; Lee, T. R. Physical Organic Probes of Interfacial Wettability Reveal the Importance of Surface Dipole Effects. *J. Phys. Org. Chem.* **2000**, *13*, 796–807.

- (15) Pensa, E.; Cortés, E.; Corthey, G.; Carro, P.; Vericat, C.; Fonticelli, M. H.; Benítez, G.; Rubert, A. A.; Salvarezza, R. C. The Chemistry of the Sulfur-Gold Interface: In Search of a Unified Model. *Acc. Chem. Res.* **2012**, *45*, 1183–1192.
- (16) Whitesides, G. M.; Kriebel, J. K.; Love, J. C. Molecular Engineering of Surfaces Using Self-Assembled Monolayers. *Sci. Prog.* **2005**, *88*, 17–48.
- (17) Guo, Z.; Meng, S.; Zhong, W.; Du, Q.; Chou, L. L. Self-Assembly of Silanated Poly(Ethylene Glycol) on Silicon and Glass Surfaces for Improved Haemocompatibility. *Appl. Surf. Sci.* **2009**, *255*, 6771–6780.
- (18) Chinwangso, P.; Lee, H. J.; Jamison, A. C.; Marquez, M. D.; Park, C. S.; Lee, T. R. Structure, Wettability, and Thermal Stability of Organic Thin-Films on Gold Generated from the Molecular Self-Assembly of Unsymmetrical Oligo(Ethylene Glycol) Spiroalkanedithiols. *Langmuir* **2017**, *33*, 1751–1762.
- (19) Li, G.; Cheng, G.; Xue, H.; Chen, S.; Zhang, F.; Jiang, S. Ultra Low Fouling Zwitterionic Polymers with a Biomimetic Adhesive Group. *Biomaterials* **2008**, *29*, 4592–4597.
- (20) Wang, Y.-S. S.; Yau, S.; Chau, L.-K. K.; Mohamed, A.; Huang, C.-J. J.; Chau, L.-K. K.; Wang, Y.-S. S.; Huang, C.-J. J.; Yau, S.; Chau, L.-K. K.; et al. Functional Biointerfaces Based on Mixed Zwitterionic Self-Assembled Monolayers for Biosensing Applications. *Langmuir* **2018**, *35*, 1652–1661.
- (21) Lee, B. S.; Chi, Y. S.; Lee, K. B.; Kim, Y. G.; Choi, I. S. Functionalization of

- Poly(Oligo(Ethylene Glycol) Methacrylate) Films on Gold and Si/SiO<sub>2</sub> for Immobilization of Proteins and Cells: SPR and QCM Studies. *Biomacromolecules* **2007**, *8*, 3922–3929.
- (22) Barriet, D.; Lee, T. R. Fluorinated Self-Assembled Monolayers: Composition, Structure and Interfacial Properties. *Curr. Opin. Colloid Interface Sci.* **2003**, *8*, 236–242.
- (23) Lee, H. H.; Gavutis, M.; Ružele, Ž.; Valiokas, R. N.; Liedberg, B. Mixed Self-Assembled Monolayers with Terminal Deuterated Anchors: Characterization and Probing of Model Lipid Membrane Formation. *J. Phys. Chem. B* **2018**, *122*, 8201–8210.
- (24) Lee, H. J.; Jamison, A. C.; Lee, T. R. Two Are Better than One: Bidentate Adsorbates Offer Precise Control of Interfacial Composition and Properties. *Chem. Mater.* **2016**, *28*, 5356–5364.
- (25) Love, J. C.; Estroff, L. A.; Kriebel, J. K.; Nuzzo, R. G.; Whitesides, G. M. Self-Assembled Monolayers of Thiolates on Metals as a Form of Nanotechnology. *Chem. Rev.* **2005**, *105*, 1103–1170.
- (26) Vericat, C.; Vela, M. E.; Corthey, G.; Pensa, E.; Cortés, E.; Fonticelli, M. H.; Ibañez, F.; Benitez, G. E.; Carro, P.; Salvarezza, R. C. Self-Assembled Monolayers of Thiolates on Metals: A Review Article on Sulfur-Metal Chemistry and Surface Structures. *RSC Adv.* **2014**, *4*, 27730–27754.

- (27) Colorado, R.; Lee, T. R. Wettabilities of Self-Assembled Monolayers on Gold Generated from Progressively Fluorinated Alkanethiols. *Langmuir* **2003**, *19*, 3288–3296.
- (28) Fukushima, H.; Seki, S.; Nishikawa, T.; Takiguchi, H.; Tamada, K.; Abe, K.; Colorado, R.; Graupe, M.; Shmakova, O. E.; Lee, T. R. Microstructure, Wettability, and Thermal Stability of Semifluorinated Self-Assembled Monolayers (SAMs) on Gold. *J. Phys. Chem. B* **2000**, *104*, 7417–7423.
- (29) Yuan, Y.; Yam, C. M.; Shmakova, O. E.; Colorado, R.; Graupe, M.; Fukushima, H.; Moore, H. J.; Lee, T. R. Solution-Phase Desorption of Self-Assembled Monolayers on Gold Derived from Terminally Perfluorinated Alkanethiols. *J. Phys. Chem. C* **2011**, *115*, 19749–19760.
- (30) Shon, Y. S.; Lee, S.; Perry, S. S.; Lee, T. R. The Adsorption of Unsymmetrical Spiroalkanedithiols onto Gold Affords Multi-Component Interfaces That Are Homogeneously Mixed at the Molecular Level. *J. Am. Chem. Soc.* **2000**, *122*, 1278–1281.
- (31) Shon, Y. S.; Lee, S.; Colorado, R.; Perry, S. S.; Lee, T. R. Spiroalkanedithiol-Based SAMs Reveal Unique Insight into the Wettabilities and Frictional Properties of Organic Thin Films. *J. Am. Chem. Soc.* **2000**, *122*, 7556–7563.
- (32) Smith, R. K.; Reed, S. M.; Lewis, P. A.; Monnell, J. D.; Clegg, R. S.; Kelly, K. F.; Bumm, L. A.; Hutchison, J. E.; Weiss, P. S. Phase Separation within a Binary Self-Assembled Monolayer on Au{111} Driven by an Amide-Containing

- Alkanethiol. *J. Phys. Chem. B* **2001**, *105*, 1119–1122.
- (33) Jackson, A. M.; Myerson, J. W.; Stellacci, F. Spontaneous Assembly of Subnanometre-Ordered Domains in the Ligand Shell of Monolayer-Protected Nanoparticles. *Nat. Mater.* **2004**, *3*, 330–336.
- (34) Yaliraki, S. N.; Longo, G.; Gale, E.; Szleifer, I.; Ratner, M. A. Stability and Phase Separation in Mixed Self-Assembled Monolayers. *J. Chem. Phys.* **2006**, *125*, 74708.
- (35) Fetisov, E. O.; Siepmann, J. I. Structure and Phase Behavior of Mixed Self-Assembled Alkanethiolate Monolayers on Gold Nanoparticles: A Monte Carlo Study. *J. Phys. Chem. B* **2016**, *120*, 1972–1978.
- (36) Chinwangso, P.; St. Hill, L. R.; Marquez, M. D.; Randall Lee, T. Unsymmetrical Spiroalkanedithiols Having Mixed Fluorinated and Alkyl Tailgroups of Varying Length: Film Structure and Interfacial Properties. *Molecules* **2018**, *23*, 2632.
- (37) Chinwangso, P.; Lee, H. J.; Lee, T. R. Self-Assembled Monolayers Generated from Unsymmetrical Partially Fluorinated Spiroalkanedithiols. *Langmuir* **2015**, *31*, 13341–13349.
- (38) Chinwangso, P.; Jamison, A. C.; Lee, T. R. Multidentate Adsorbates for Self-Assembled Monolayer Films. *Acc. Chem. Res.* **2011**, *44*, 511–519.
- (39) Frey, S.; Heister, K.; Zharnikov, M.; Grunze, M.; Tamada, K.; Colorado, R.; Graupe, M.; Shmakova, O. E.; Lee, T. R. Structure of Self-Assembled Monolayers of Semifluorinated Alkanethiols on Gold and Silver Substrates. *Isr. J. Chem.* **2000**,

40, 81–97.

- (40) Akimov, Y.; Pam, M. E.; Sun, S. Kretschmann-Raether Configuration: Revision of the Theory of Resonant Interaction. *Phys. Rev. B* **2017**, *96*, 155433–155440.
- (41) Buttry, D. A.; Ward, M. D. Measurement of Interfacial Processes at Electrode Surfaces with the Electrochemical Quartz Crystal Microbalance. *Chem. Rev.* **1992**, *92*, 1355–1379.
- (42) Sauerbrey, G. Verwendung von Schwingquarzen Zur Wägung Dünner Schichten Und Zur Mikrowägung. *Zeitschrift für Phys.* **1959**, *155*, 206–222.
- (43) Gamry Instruments. Basics of a Quartz Crystal Microbalance. *Spectrum* **2012**, *1*, 1–7.
- (44) Tsai, D. H.; Delrio, F. W.; Keene, A. M.; Tyner, K. M.; MacCuspie, R. I.; Cho, T. J.; Zachariah, M. R.; Hackley, V. A. Adsorption and Conformation of Serum Albumin Protein on Gold Nanoparticles Investigated Using Dimensional Measurements and in Situ Spectroscopic Methods. *Langmuir* **2011**, *27*, 2464–2477.
- (45) Bachmann, L.; Schmitt-Fumain, W. W.; Hammel, R.; Lederer, K. Size and Shape of Fibrinogen, 1. Electron Microscopy of the Hydrated Molecule. *Die Makromol. Chemie* **1975**, *176*, 2603–2618.
- (46) Colvin, J. R. The Size and Shape of Lysozyme. *Can. J. Chem.* **1952**, *30*, 831–834.
- (47) Marucco, A.; Catalano, F.; Fenoglio, I.; Turci, F.; Martra, G.; Fubini, B. Possible Chemical Source of Discrepancy between in Vitro and in Vivo Tests in

- Nanotoxicology Caused by Strong Adsorption of Buffer Components. *Chem. Res. Toxicol.* **2015**, *28*, 87–91.
- (48) Parkes, M.; Myant, C.; Cann, P. M.; Wong, J. S. S. The Effect of Buffer Solution Choice on Protein Adsorption and Lubrication. *Tribol. Int.* **2014**, *72*, 108–117.
- (49) Bolan, C. D.; Klein, H. G. Blood Component and Pharmacologic Therapy for Hemostatic Disorders. In *Consultative Hemostasis and Thrombosis: Third Edition*; Saunders: Philadelphia, 2013.
- (50) Attwood, S.; Kershaw, R.; Udin, S.; Bishop, S.; Welland, M. Understanding Globular Protein Adsorption to Alkanethiol and Material Surfaces. *J. Mater. Chem. B Under Rev.* **2019**, *7*, 2349–2361.
- (51) Pflaum, J.; Bracco, G.; Schreiber, F.; Colorado, R.; Shmakova, O. E.; Lee, T. R.; Scoles, G.; Kahn, A. Structure and Electronic Properties of CH<sub>3</sub>- and CF<sub>3</sub>-Terminated Alkanethiol Monolayers on Au(1 1 1): A Scanning Tunneling Microscopy, Surface X-Ray and Helium Scattering Study. *Surf. Sci.* **2002**, *498*, 89–104.
- (52) Chidsey, C. E. D.; Loiacono, D. N. Chemical Functionality in Self-Assembled Monolayers: Structural and Electrochemical Properties. *Langmuir* **1990**, *6*, 682–691.
- (53) Ulman, A.; Eilers, J. E.; Tillman, N. Packing and Molecular Orientation of Alkanethiol Monolayers on Gold Surfaces. *Langmuir* **1989**, *5*, 1147–1152.
- (54) Zhao, X. M.; Wilbur, J. L.; Whitesides, G. M. Using Two-Stage Chemical Amplification To Determine the Density of Defects in Self-Assembled

Monolayers of Alkanethiolates on Gold. *Langmuir* **1996**, *12*, 3257–3264.

- (55) Lio, A.; Charych, D. H.; Salmeron, M. Comparative Atomic Force Microscopy Study of the Chain Length Dependence of Frictional Properties of Alkanethiols on Gold and Alkylsilanes on Mica. *J. Phys. Chem. B* **2002**, *101*, 3800–3805.
- (56) Overney, R. M.; Meyer, E.; Frommer, J.; Brodbeck, D.; Lüthi, R.; Howald, L.; Güntherodt, H. J.; Fujihira, M.; Takano, H.; Gotoh, Y. Friction Measurements on Phase-Separated Thin Films with a Modified Atomic Force Microscope. *Nature* **1992**, *359*, 133–135.
- (57) Rickert, J.; Brecht, A.; Göpel, W. Quartz Crystal Microbalances for Quantitative Biosensing and Characterizing Protein Multilayers. *Biosens. Bioelectron.* **1997**, *12*, 567–575.
- (58) Levi, M. D.; Daikhin, L.; Aurbach, D.; Presser, V. Quartz Crystal Microbalance with Dissipation Monitoring (EQCM-D) for in-Situ Studies of Electrodes for Supercapacitors and Batteries: A Mini-Review. *Electrochem. commun.* **2016**, *67*, 16–21.
- (59) Ispas, A.; Bund, A. Electrochemical Quartz Crystal Microbalance. In *Encyclopedia of Applied Electrochemistry*; Springer: New York, 2014.
- (60) Allan, L. S.; Smith, A. L. The Quartz Crystal Microbalance. *Handb. Therm. Anal. Calorim.* **2008**, *5*, 133–169.
- (61) Kushmerick, J. G.; Weiss, P. S. Scanning Probe Microscopes. In

*Encyclopedia of Spectroscopy and Spectrometry*; Academic Press: Cambridge, 2016.

- (62) Dupont-Gillain, C. C.; Fauroux, C. M. J.; Gardner, D. C. J.; Leggett, G. J. Use of AFM to Probe the Adsorption Strength and Time-Dependent Changes of Albumin on Self-Assembled Monolayers. *J. Biomed. Mater. Res. - Part A* **2003**, *67A*, 548–558.
- (63) Jalili, N.; Laxminarayana, K. A Review of Atomic Force Microscopy Imaging Systems: Application to Molecular Metrology and Biological Sciences. *Mechatronics* **2004**, *14*, 907–945.
- (64) Variola, F. Atomic Force Microscopy in Biomaterials Surface Science. *Phys. Chem. Chem. Phys.* **2015**, *17*, 2950–2959.
- (65) Engel, A.; Lyubchenko, Y.; Müller, D. Atomic Force Microscopy: A Powerful Tool to Observe Biomolecules at Work. *Trends Cell Biol.* **1999**, *9*, 77–80.
- (66) Schönherr, H.; Vancso, G. J. Atomic Force Microscopy in Practice. In *Scanning Force Microscopy of Polymers*; Springer: Berlin, 2010.
- (67) Friedbacher, G. Atomic Force Microscopy (AFM). In *Surface and Thin Film Analysis: A Compendium of Principles, Instrumentation, and Applications, Second Edition*; Wiley-VCH: Weinheim, 2011.
- (68) Yablou, D. G. Overview of Atomic Force Microscopy. In *Scanning Probe Microscopy for Industrial Applications: Nanomechanical Characterization*; John Wiley & Sons, Inc.: Hoboken, 2013.

- (69) Cruz, T. G. S.; Albuquerque, D. A. C.; De, R. R. L.; Yamaji, F. M.; Leite, F. L. Measurement of the Nanoscale Roughness by Atomic Force Microscopy: Basic Principles and Applications. In *Atomic Force Microscopy - Imaging, Measuring and Manipulating Surfaces at the Atomic Scale*; IntechOpen: London, 2012.

## **Chapter 3. Biofouling Studies of Unsymmetrical Oligo(ethylene glycol) Spiroalkanedithiols**

### **3.1. Introduction**

Many biological applications use poly(ethylene glycol) (PEG) or poly(ethylene oxide) (PEO), which is a biocompatible polymer.<sup>1,2</sup> Surfaces modified with PEG coatings exhibit outstanding protein-resistant properties, and consequently have been incorporated widely into biomaterials to impart resistance to proteins and larger macromolecules, such as cells.<sup>2-5</sup> Protein resistance is an important feature for materials, such as biosensors and biological devices which have interfacial contact with biological environments.<sup>6,7</sup> Since polymer surfaces are rough and typically non-uniform, there is some difficulty in obtaining accurate and reproducible characterization data.<sup>8</sup> Since the protein resistant properties of PEG have proven effective even in surfaces presenting oligo(ethylene glycol) (OEG) moieties containing only 2-6 monomer units,<sup>9-12</sup> self-assembled monolayers (SAMs) containing OEG-terminated alkanethiols on gold have been used as model systems to obtain well-defined films that can generate accurate and reproducible characterization data.<sup>13-20</sup> Organic synthesis allows for the easy modification of the terminal groups to tailor the SAM surfaces, and the gold substrate is practical with its high biocompatibility with biological applications.<sup>13</sup>

Studies have shown that tri(ethylene glycol)-terminated alkanethiols on gold exhibit protein resistant properties.<sup>11,15,21</sup> Similar protein resistance was observed in OEG chains containing methoxy- or hydroxyl- termination, eliminating the need for a hydrophilic hydroxyl terminated interface.<sup>11</sup> A major concern and limiting factor in the

use of these SAMs is the stability of the films as a result from a single point attachment between the monothiol adsorbates and the gold substrate.<sup>16</sup> Decomposition of *n*-alkanethiol SAMs occurs at ~70 °C,<sup>16,20</sup> thus an advantage of a bidentate adsorbate is the ability to create multiple attachment points between the adsorbate and the gold substrate, which enhances the film stability.<sup>22–29</sup> Another advantage of bidentate adsorbates is the ability to incorporate two different terminal groups into the same molecule, which offers greater flexibility in film composition and the generation of homogeneously mixed interfaces.<sup>22,23</sup>

Our group has used the bidentate synthetic procedure to generate "conflicted" interfaces comprised of chemically disparate species held in close proximity when preferring to separate.<sup>22,23,29–31</sup> The synthesis of bidentate adsorbates containing a combination of mixed chain character, possessing methoxy-terminated tri(ethylene glycol) and *n*-alkanethiol chains, identified as **EG3C7-C7** and **EG3C7-C18** are found in Figure 3.1.<sup>32</sup> The generation of SAMs from these adsorbates permits studies to determine the behavior and properties of species that typically would phase separate, resulting in surfaces with patches of single component domains.<sup>33–37</sup>

The present study examines the interaction of two bidentate adsorbates possessing mixed interfaces generated from the combination of *n*-alkane and methoxy-terminated tri(ethylene glycol) chains with multiple proteins to assess the antifouling properties of the surfaces, where phase separation is restricted or eliminated in this well-defined unnatural system that is held in close proximity when preferring to be apart. Specifically, we generated SAMs from the unsymmetrical oligo(ethylene glycol) spiroalkanedithiols

(SADTs) **EG3C7-C7** and **EG3C7-18** to investigate protein interactions on these homogeneously mixed interfaces (see Figure 3.1). The SAMs were prepared alongside an analogous *n*-alkanethiol (**C18SH**) and an OEG-terminated monothiol (**EG3C7SH**) to compare the performance of the SADT-based SAMs with the monodentate analogs and to evaluate the impact of adsorbate structure on protein resistance. Protamine, lysozyme, bovine serum albumin (BSA), and fibrinogen were selected for this investigation due to the range in properties. We hypothesized that the dual chemical heterogeneity of the interfaces comprised of chemically disparate species held in close proximity, while preferring to be apart would generate interactions resulting in a combination of the dual nature of the interface species. The incorporation of the hydrocarbon chain may act as a spacer for the OEG chain, resulting in better packing in the lower chain portion of the SAM and more freedom to move at the interface, generating better hydration layers. The shorter hydrocarbon chain may allow for the OEG portion to sit atop the hydrocarbon portion, decreasing the interactions from the hydrocarbon chain at the interface. The bidentate adsorbate should produce better stability compared to the monodentate adsorbates, due to the increased attachment points with the substrates.

Since ethylene glycol units are used in various biological applications, the properties found may render these surfaces useful for additional biological applications. A methoxy terminal group is used for the OEG chains to prevent complications resulting from hydrogen bonds between chains that might be afforded with a hydroxyl terminal group.<sup>32</sup> Notably, the bidentate adsorbate **EG3C7-C7** is designed with a shorter chained alkanethiol, compared to **EG3C7-C18** that contains a longer chain in order to compare the influence of

chain length on the protein resistance properties of the resulting SAMs. We characterized the protein resistance properties of the generated films using optical ellipsometry, surface plasmon resonance (SPR), quartz crystal microbalance (QCM), and atomic force microscopy (AFM).

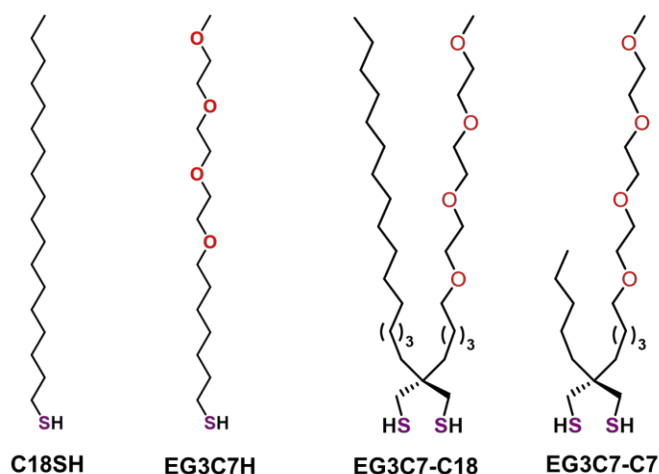


**Figure 3.1.** Molecular structures of the monodentate, **C18SH** and **EG3C7SH**, as well as the bidentate, **EG3C7-C18** and **EG3C7-C7**, adsorbates analyzed in this study.

## 3.2. Experimental Section

### 3.2.1 Materials

All chemicals were used as received unless otherwise noted: ethanol from AAPER Alcohol and Chemical Co, tetrahydrofuran (THF), sulfuric acid (H<sub>2</sub>SO<sub>4</sub>), and hydrogen peroxide (30% H<sub>2</sub>O<sub>2</sub>) all from Avantor Performance Materials. Fibrinogen, lysozyme, bovine serum albumin, protamine, and the adsorbate 1-octadecanethiol (**C18SH**) was purchased from Sigma-Aldrich. The other adsorbates, 2,5,8,11-tetraoxaoctadecane-18-thiol (**EG3C7SH**), 2-(2,5,8,11-tetraoxahexadecane-16-yl)-2-hexadecylpropane-1,3-dithiol (**EG3C7-C18**), and 2-(2,5,8,11-tetraoxahexadecane-16-yl)-2-pentylpropane-1,3-

dithiol (**EG3C7-C7**) were synthesized according to procedures found in the literature.<sup>32</sup> Phosphate Buffer Solution (PBS) 10x from GenDepot was diluted to 1x using water (H<sub>2</sub>O), generated from a Milli-Q Water System with resistance of 18.2 M $\Omega$ .

Gold shot (99.99%) was purchased from Kamis, Inc. and chromium rods (99.9%) were purchased from Kurt J. Lesker Company and used as received. Polished single-crystal Si(100) wafers purchased from Silicon Sense, Inc. were rinsed with absolute ethanol before use. SPR sensors composed of 500 Å of Au plated on Ti-coated silica substrates were purchased from Sofchip. The QCM sensors composed of polished AT cut quartz crystals oscillating at a 10 MHz frequency coated with Ti and plated with 1000 Å of gold were purchased from Novatech. NTESPA AFM cantilevers made from antimony (n)-doped silicon tips with reflective aluminum coating (MPP-11220-10) were obtained from Bruker and used as received. Ultra-flat gold, 1000 Å of gold on a silicon wafer, was purchased from Platypus technology and used as received.

### **3.2.2 Preparation of Substrates**

Thermal evaporation of gold onto Si(100) wafers at a vacuum pressure  $\leq 6 \times 10^{-5}$  torr was used to prepare gold substrates used in ellipsometric thickness measurements. Initially a 100 Å chromium adhesion layer was deposited, followed by a 1000 Å gold layer depositing at a rate of 0.5 Å/s. SPR and QCM sensors required submersion in piranha solution, then rinsed with copious amounts of water (H<sub>2</sub>O), followed by a rinse with absolute ethanol, then dried in a stream of ultra-pure nitrogen gas immediately prior to preparation of the SAMs. *Caution: Piranha solution reacts violently with organic materials and should be handled carefully!*

### **3.2.3. Preparation of the SAMs**

Prior to preparation of solution, all vials were cleaned using piranha solution, then rinsed with copious amounts of deionized water followed by absolute ethanol. Each respective gold substrate (evaporated gold, QCM sensors, SPR sensors, or ultra- flat gold on silica) was prepared by submersion in a 1 mM solution of the respective thiols in ethanoic solution. The SAMs were placed in a dark environment at rt for 48 h to equilibrate. All SAMs were rinsed with THF, followed by absolute ethanol, and then dried with a stream of ultra-pure nitrogen before any measurements were obtained.

### **3.2.4. Protein Preparation/Exposure.**

Protein solutions consisting of a 1 mg/mL concentration were prepared by dissolving 1 mg of the protein in 1 mL of the PBS solution and then sonicated for 15 mins. Prior to use, all protein solutions and buffers were filtered using a 0.2  $\mu\text{m}$  filter. The SPR sensors were exposed to the protein solution through an automated injection using a Biacore 2000 instrument, and an automated protocol to measure *in situ* interactions with the protein solutions. The remaining substrates (thermally evaporated Au samples, QCM sensors and ultra-flat gold) were submerged into the protein solutions for 1 h to allow the SAMs to reach saturation of the protein on the surface. Upon removal, the substrate samples were rinsed first with PBS buffer followed with water ( $\text{H}_2\text{O}$ ), and then dried with a stream of ultra-pure nitrogen gas.

### **3.2.5. Ellipsometry Measurements**

A Rudolph Auto EL III ellipsometer equipped with a He-Ne laser (632.8 nm) at an incident angle set of  $70^\circ$ , and a refractive index set to 1.45 was used to obtain the monolayer

thickness for each substrate sample. The thickness values reported are an average of 24 measurements (4 slides for each adsorbate having 2 measurements per slide and 3 independent trials). After the SAMs were immersed in ethanolic solution at rt for 48 h to equilibrate, the thickness of the SAMs was measured. After the formation of SAMs, each slide was immersed in the protein solutions for 1 h, separately, to allow the surface to become saturated with the protein. The substrates were rinsed with PBS and water, then dried with a stream of ultra-pure nitrogen gas prior to measuring the ellipsometric thickness a second time to determine changes in thickness due to protein exposure. The change in thickness is calculated by subtracting optical thickness of the initial SAM, from the total optical thickness measurement of the SAM after exposure to the protein. The reported optical thickness measurements of the SAMs after protein exposure are an average of 6 measurements (2 measurements per slide with 3 individual trials per adsorbate and protein). All surfaces (Evaporated gold, SPR, QCM sensors, and flat gold) were characterized for formation of the SAM using optical ellipsometry. Ellipsometric values are reported from the evaporated gold surface, but no distinguishable differences in SAMs' thickness or in thickness after protein exposure were observed between the evaporated gold, ultra-flat gold, the SPR, or QCM gold sensor surface.

### **3.2.6. SPR Procedures**

A Biacore 2000 was used to obtain the SPR sensorgrams. The SPR sensors containing the SAMs were inserted into the Biacore 2000 and exposed to a running PBS buffer at a rate of 30  $\mu\text{L}/\text{min}$ . Through an automated program, 300  $\mu\text{L}$  injections of each protein solution at a concentration of 1 mg/mL were injected into each respective channel.

Buffer continued to flow over each channel and measurements were recorded for an additional 2 h following each injection on each channel. Allowing the PBS buffer to flow over the surface after exposure to the protein solution permits any unbound or weakly attached protein to be washed away. Application of the Kretschmann theory in this SPR technique allows for the generation of sensorgrams.<sup>38</sup> A sensorgram is generated as a result of a change in the resonance angle of light reflected from the Au surface. The change in mass associated with the interaction of the protein with the surface through binding and disassociation results in a change in the angle of reflection of the light from the surface of the sensor. A signal is generated in the sensorgram that reflects an increase in signal for protein interaction and a decrease for protein removal as a response to the change in the refractive index at the interface of the surface. Each new generated surface was exposed to each protein solution on the respective channel, and the reported values are an average of 3 trials and include the standard deviation. The reported value of  $\Delta$ RU is the difference between the ground response and the final response after protein exposure and the flow of buffer.

### **3.2.7. QCM Measurements**

A Gamry eQCM was used to simultaneously measure the parallel and series frequency measurements ( $f$ ) of functionalized QCM sensors at the bare gold state, SAMs layer, and again after exposure to protein. The eQCM maintains a continuous driving voltage to the piezoelectric crystal, and the reported values are an average of the resonant frequency after stabilization. The resonant frequency is generated once a voltage is applied to a thin AT-cut piezoelectric crystal that is sandwiched between two Au plates. The

applied voltage produces an alternating electric field on each side of the crystal which results in the generation of a mechanical shear wave modulate and a vibrational motion, thus producing the resonant frequency for the crystal. A change in resonant frequency is observed with even a small amount of mass loss or gain. An increase in mass will result in a decrease of frequency, and a loss of mass will result in an increase in frequency. The Sauerbrey equation (Equation 3.1) is used to evaluate the proportional relationship between the values of the change in frequency  $\Delta f$  to the value of the change in mass ( $\Delta m$ ).<sup>39-41</sup>

$$\Delta m = -C_f \Delta f \quad (3.1)$$

The mass loading of the 10 MHz AT-cut quartz crystal microbalance sensor surfaces after protein exposure can be quantified using Equation 3.1, where  $C_f$  (the mass sensitivity constant) is  $-226 \mu\text{g Hz}^{-1} \text{cm}^{-2}$ .<sup>41</sup>

### **3.2.8. AFM Imaging and Measurements**

The ultra-flat gold on silica was prepared with each SAM and exposed to the protein solution. Upon rinsing and drying, each surface was imaged with an Agilent 5000 atomic force microscope. All images were recorded at rt in air and within 2 h of removing from the protein solution. Imaging was performed in air using acoustic (AC) mode and NTESPA AFM cantilevers made from antimony (n)-doped silicon tips with reflective aluminum coating cantilevers. All images were processed using Gwyddion to obtain arithmetic average (Ra), root mean square (RMS), and height density plot distributions. Each surface was imaged 6 times, and the calculations include the standard deviation.

### 3.3. Results and Discussion

In order to evaluate protein adhesion, SAMs surfaces were monitored before, during, and after protein exposure. A variety of proteins were selected in this study to determine how their properties may influence adhesion to the various surfaces. Proteins were selected based on molecular weight, size, isoelectric point (pI), and application. Commonly used proteins such as bovine serum albumin (BSA), a stable moderate sized protein,<sup>42</sup> and fibrinogen, a large molecular weight protein with a neutral isoelectric point, were two of the proteins selected.<sup>43</sup> Additionally, lysozyme, a smaller molecular weight protein containing a positive charge,<sup>44</sup> and protamine, containing a low molecular weight, with a pI of 12.1,<sup>45</sup> are two more proteins selected in this study. The selection of proteins allows for a more explorative approach to protein interactions with the SAM surfaces.

Table 3.1 supplies a more comprehensive list of the properties of the selected proteins. Since the selected proteins are well suited in a phosphate buffer solution (PBS), the protein solutions are made in PBS. To ensure no aberrations resulting from the buffer exposure to the SAMs surface interfere with the analysis, changes associated with the buffer exposure to the film were monitored; no noted changes were observed.<sup>46,47</sup> The non-specific adsorption of the selected proteins to the SAM surfaces was measured qualitatively, and the amount of protein adhered to the surface quantitatively using the selected analytical techniques of ellipsometry, surface plasmon resonance spectroscopy (SPR), quartz crystal microbalance (QCM), and atomic force microscopy (AFM).

**Table 3.1.** Physical Properties of Proteins Examined in this Investigation

<b>Protein</b>	<b>Molecular Weight</b>	<b>Size</b>	<b>PI</b>	<b>Shape</b>	<b>Application</b>
<b>Protamine</b> <sup>45</sup>	4 KDa	5 Å	12.1	Spheres	Insulin
<b>Lysozyme</b> <sup>44</sup>	14 KDa	18 Å <sup>c</sup>	11.1	Stubby Prolate Ellipsoid	Cell
<b>BSA</b> <sup>42</sup>	55 KDa	140 x 40 x 40 Å	4.8	Prolate ellipsoid <sup>a</sup>	Blood
<b>Fibrinogen</b> <sup>43</sup>	340 KDa	450 x 90 Å	5.7	Cylindrical <sup>b</sup>	Muscle/ Tissue

<sup>a</sup> where a=b<c<sup>b</sup> with round ends<sup>c</sup> diameter

### 3.3.1. *In situ* Analysis of Protein Adhesion Using SPR Spectroscopy

Surface plasmon resonance spectroscopy provided a way to probe and monitor *in situ* interactions of the proteins interacting with the surface. This technique generated a sensorgram resulting from the change of response units that correlates to the amount of nonspecific protein adsorption on the surface of the SAM. The sensorgrams reporting the change in response to the interactions between each of the selected proteins and the SAMs surfaces are displayed in Figure 3.2. The calculated change in response units ( $\Delta RU$ ) was obtained by subtracting the final response unit value from the baseline, and the numerical calculation of the resulting  $\Delta RU$  values are found in Table 3.2 and is graphically represented in Figure 3.3.

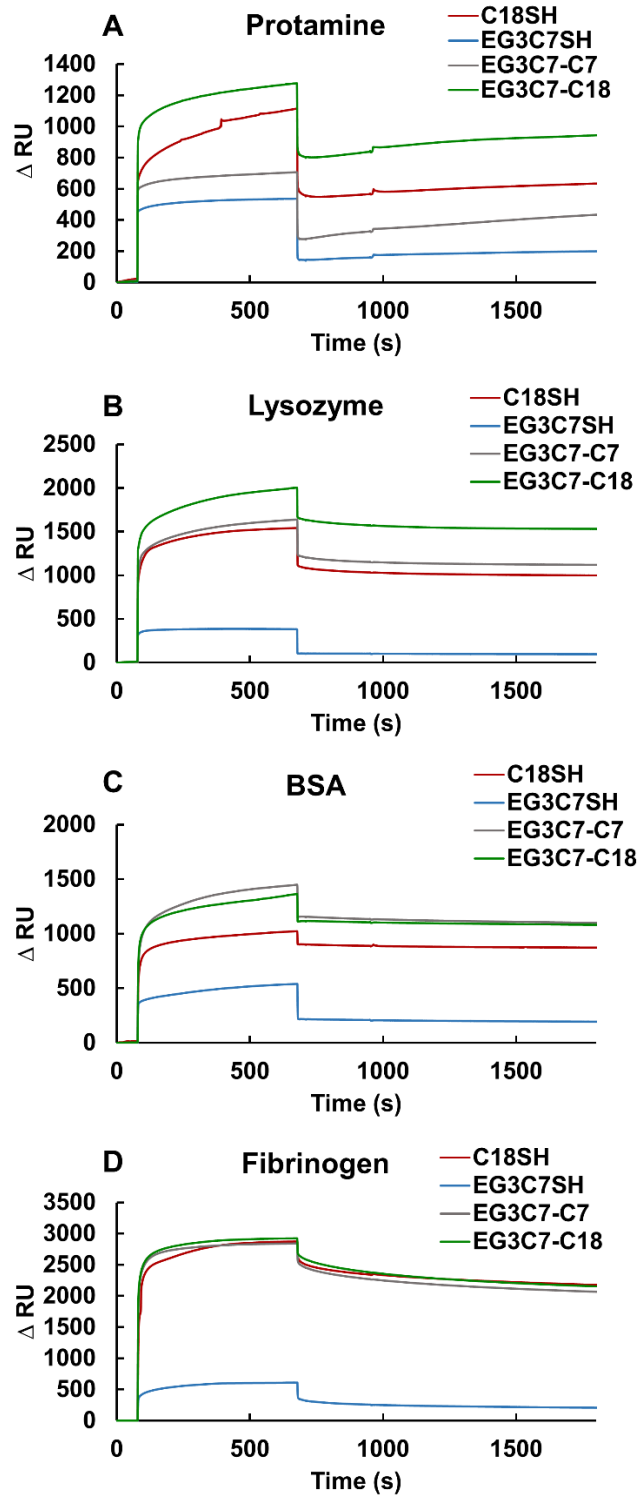


**Figure 3.2.** SPR sensorgrams of the SAMs (C18SH, EG3C7SH, EG3C7-C7, and EG3C7-C18) exposed to (A) protamine, (B) lysozyme, (C) BSA, and (D) fibrinogen. Protein solutions were prepared at a concentration of 1 mg/mL in a PBS buffer.

The **EG3C7SH** adsorbate consistently resisted protein adsorption more when compared to **C18SH**, and the SADTs (**EG3C7-C7** and **EG3C7-C18**). For example, fibrinogen produced  $\Delta$ RU values of 2285, 201, 2194 and 2295 for SAMs generated from **C18SH**, **EG3C7SH**, **EG3C7-C7**, and **EG3C7-C18**, respectively. The **EG3C7SH** is an oligo(ethylene glycol)-terminated (OEG) SAM, and it has been shown that OEG-terminated SAMs exhibit high protein resistance due to several characteristics of the adsorbate structure.<sup>2,11,14,48-51</sup> The strong polarity results in hydrophilic properties, which aid in the ability to generate repulsive forces to depress protein adhesion.<sup>2,11,14,48-51</sup> The helical conformation of the OEG SAMs provides a template for water nucleation which depicts the amphiphilic behavior. The high degree of freedom provides a favorable free energy, so when the OEG chain is confined, an entropic effect is observed, resulting from the unfavorable change in free energy, decreasing protein resistance.<sup>14,49,51,52</sup> Also, hydrogen bonding plays a vital role in the stabilization of the ethylene glycol chains.<sup>2,11,48,52</sup> The electrostatic interactions dominate the energetics of water adsorption, therefore, the presence of OEG alters the electrical nature of the surface at the interface, generating an electrically neutral environment.<sup>2,48</sup> On the other hand, the **C18SH** adsorbate is hydrophobic in nature, resulting in more favorable interactions with the proteins at the interface<sup>53</sup> and generates a larger  $\Delta$ RU when compared to the **EG3C7SH** adsorbate.

**Table 3.2.** The  $\Delta$ RU Values for SAMs after Exposure to 300  $\mu$ L Injection of 1 mg/mL Protein Solution

Adsorbate	$\Delta$ RU			
	Protamine	Lysozyme	BSA	Fibrinogen
<b>C18SH</b>	599 $\pm$ 3	1029 $\pm$ 42	899 $\pm$ 63	2285 $\pm$ 222
<b>EG3C7SH</b>	173 $\pm$ 11	108 $\pm$ 20	195 $\pm$ 53	201 $\pm$ 46
<b>EG3C7-C7</b>	368 $\pm$ 87	1163 $\pm$ 77	1121 $\pm$ 145	2194 $\pm$ 122
<b>EG3C7-C18</b>	936 $\pm$ 48	1524 $\pm$ 80	1051 $\pm$ 96	2295 $\pm$ 24

In the case of the SADT adsorbates (**EG3C7-C7** and **EG3C7-C18**), the divergence of the two types of adsorbates into a double chain dithiol influences the film structure and/or chain orientation for each adsorbate, resulting from the unfavorable interactions between the hydrophobic hydrocarbon chain and the hydrophilic OEG-terminated chain.<sup>32</sup> With respect to **EG3C7-C18** adsorbate, although the film is disordered, the **C18-** chain may limit the degrees of freedom for the **EG3C7-** chain, producing an entropic effect and unfavorable interactions, which lead to a decrease in the protein resistant properties of the **EG3C7-** moiety. In comparison, the **EG3C7-C7** adsorbate, the shorter alkyl chain may interfere less with the degrees of freedom in the conformation of the **EG3C7-** chain as the **C7-** segment plausibly lies beneath the OEG-terminated component.<sup>32</sup> This is noted especially in the small and positively charged proteins, like protamine, where the  $\Delta$ RU values were 599, 173, 368, and 936 for SAMs generated from **C18SH**, **EG3C7SH**, **EG3C7-C7**, **EG3C7-C18**, respectively. With lysozyme, an increase in  $\Delta$ RU was observed after exposure to protein solution for all of the SAMs with **EG3C7SH** having the lowest

values for  $\Delta$ RU. When the  $\Delta$ RU value for **EG3C7SH** is compared to the other  $\Delta$ RU values for the other proteins, a slight decrease in the amount of response is observed, and this is indicative of the electrostatic interactions that are altered with the presence of the OEG segment. In the case of lysozyme, the **EG3C7-C7** and **EG3C7-C18** SAMs with 1524  $\Delta$ RU and 1163  $\Delta$ RU, respectively, denotes a greater  $\Delta$ RU when interacting with a small positive protein when compared to **C18SH** at 1029  $\Delta$ RU, and it shows an even lower response in the **EG3C7SH** at 108  $\Delta$ RU. When in the presence of BSA, a relatively neutral and greater molecular weight protein, a decrease in response for all adsorbates after exposure to the protein solution was observed, indicating less interactions with the material at the interface. However, the trends still holds where **EG3C7-C18** (1051) and **EG3C7-C7** (1121) have a greater  $\Delta$ RU compared to **C18SH** (899), and **EG3C7SH** (195) by having the lowest  $\Delta$ RU. The addition of the hydrocarbon chain in the **EG3C7-C7** and the **EG3C7-C18** adsorbates is found to be detrimental to the protein resistant properties of the OEG chain due to the greater unfavorable interactions between the two phase incompatible groups, leading to a greater amount of protein adhesion on the surface of the adsorbate.

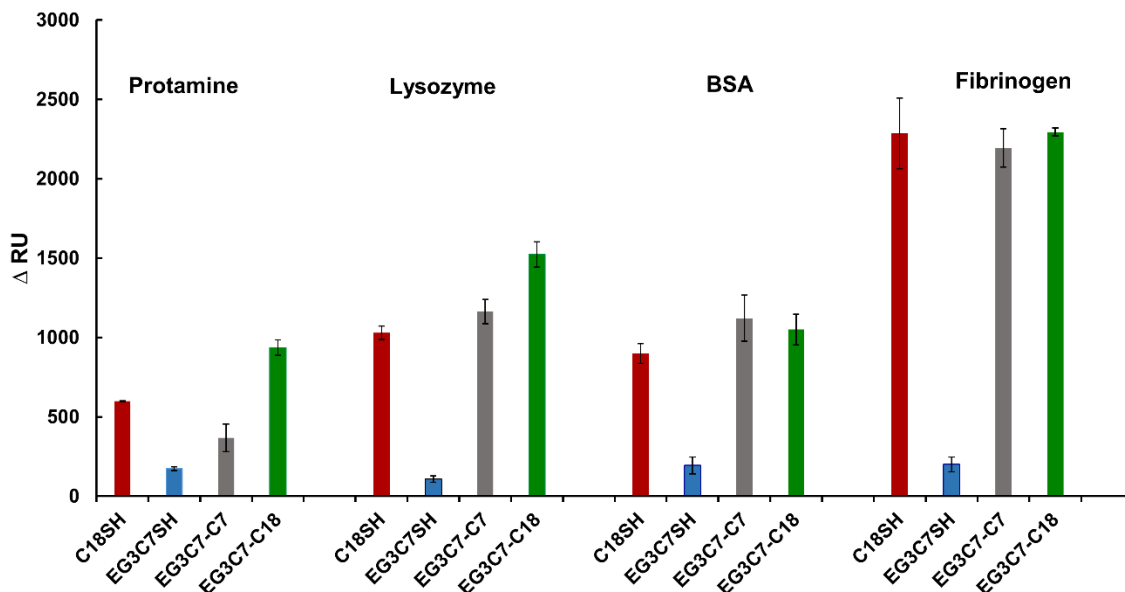


**Figure 3.3.** Graphical representation of the  $\Delta$ RU values for the SAMs after exposure to a 300  $\mu$ L injection of 1 mg/mL protein solution.

### 3.3.2. Ellipsometric Thickness Measurements

Thickness measurements to confirm the formation of the monolayers were obtained using optical ellipsometry for all substrates. The thickness measurements for all SAMs were consistent with previously reported values found in literature<sup>32</sup> and can be found in Table 3.3. All substrates exhibited similar thickness values prior and after protein exposure, but the measured values reported herein are for the evaporated gold surfaces. Table 3.4 lists the numerical values in the changes in thickness after protein exposure, while Figure 3.4 graphically presents the values. Insight into the protein resistant properties of the SAMs can be evaluated by measuring the change in the thickness after protein exposure to provide a rough estimate of the amount of protein adhered to the surface. Exposure of the adsorbates to the various proteins lead to the same trend, where **C18SH** and **EG3C7-C18** have similar values, while **EG3C7-C7** is smaller, but **EG3C7SH**

has the least amount of change in thickness. For example, protamine:  $11 \pm 5$ ,  $2 \pm 2$ ,  $3 \pm 3$ , and  $9 \pm 4$  Å for the **C18SH**, **EG3C7SH**, **EG3C7-C7**, and **EG3C7-C18**, respectively. A similar trend was observed after exposure with lysozyme:  $20 \pm 2$ ,  $2 \pm 1$ ,  $20 \pm 7$ , and  $19 \pm 2$  Å for **C18SH**, **EG3C7SH**, **EG3C7-C7**, and **EG3C7-C18**, respectively. With the exception of **EG3C7SH**, the thickness values after protein exposure increased as the molecular weight of the protein increased, as noted with BSA where  $13 \pm 8$ ,  $2 \pm 3$ ,  $16 \pm 4$ , and  $8 \pm 2$  Å for **C18SH**, **EG3C7SH**, **EG3C7-C7**, and **EG3C7-C18**, respectively. The largest change in thickness was obtained after exposure of the adsorbates to fibrinogen at 340 KDa, the largest molecular weight protein. The observed changes in thickness values were  $43 \pm 2$ ,  $3 \pm 1$ ,  $39 \pm 2$ , and  $27 \pm 1$  Å for **C18SH**, **EG3C7SH**, **EG3C7-C7**, and **EG3C7-C18**, respectively. An increase in surface roughness can impact ellipsometric measurements, therefore AFM investigations discussed later indicate surface roughness evaluations.

**Table 3.3.** Ellipsometric Thickness Values of the SAMs Prior to Exposure to Proteins

<b>Adsorbate</b>	<b>C18SH</b>	<b>EG3C7SH</b>	<b>EG3C7 – C7</b>	<b>EG3C7 – C18</b>
<b>Thickness (Å)</b>	$23 \pm 1$	$17 \pm 1$	$10 \pm 1$	$12 \pm 1$

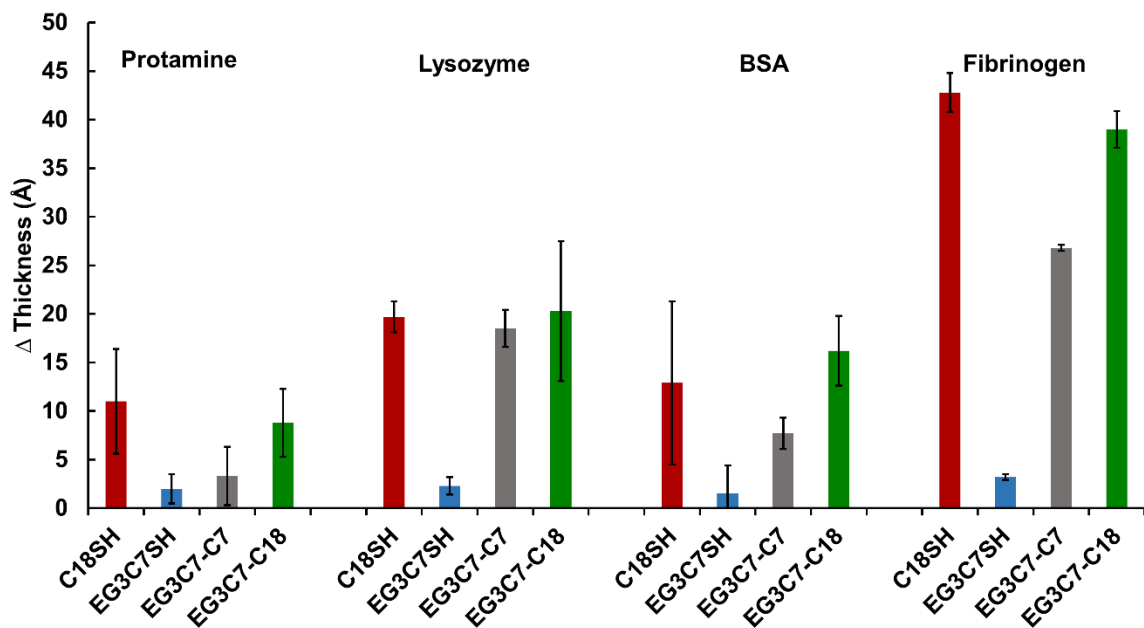


**Figure 3.4.** Changes in the thickness of the SAMs generated from **C18SH**, **EG3C7SH**, **EG3C7-C7**, and **EG3C7-C18** after exposure to solutions of protamine, lysozyme, BSA, and fibrinogen.

The changes in thickness after exposure to the various proteins, graphically presented in Figure 3.4, indicate an increase in thickness measurements as the molecular weight of the protein increases (e.g. protamine < lysozyme < BSA < fibrinogen) with the exception of **EG3C7SH**, which indicates the same change in thickness regardless of protein. The SAMs exhibit a large error after protein exposure, which can be attributed to the greater scatter resulting from an increase in surface roughness. The increase in surface roughness was confirmed by AFM measurements (*vide infra*). The thickness measurements obtained using optical ellipsometry indicate that **C18SH** and **EG3C7-C18** behave similarly in the presence of the respective proteins, and **EG3C7-C7** adheres slightly less material to the surface, but **EG3C7SH** contains the least amount of adhered material on the surface after exposure. This data further supports the SPR results where the addition

of the hydrocarbon segment in the dual chain molecules **EG3C7-C7** and **EG3C7-C18** generate adsorbates where the "conflicted" nature of the hydrocarbon chain and the OEG chain have greater unfavorable interactions between incompatible groups resulting in greater protein adhesion to the surface.<sup>32</sup> However, the shorter chain, which is likely below the helical OEG chain, disrupts the degree of freedom needed in the OEG chain slightly less, resulting in the **EG3C7-C7** SAM to adhere slightly less material at the interface of the adsorbate.<sup>14,48,49</sup>

**Table 3.4.** Changes in Ellipsometric Measurement Values after Exposure to 1 mg/ml in PBS Protein Solutions of Protamine, Lysozyme, BSA, and Fibrinogen for **C18SH**, **EG3C7SH**, **EG3C7-C7**, and **EG3C7-C18** Adsorbates

$\Delta$ Thickness (Å)	<b>C18SH</b>	<b>EG3C7SH</b>	<b>EG3C7-C7</b>	<b>EG3C7-C18</b>
<b>Protamine</b>	11 ± 5	2 ± 2	3 ± 3	9 ± 4
<b>Lysozyme</b>	20 ± 2	2 ± 1	19 ± 2	20 ± 7
<b>BSA</b>	13 ± 8	2 ± 3	8 ± 2	16 ± 4
<b>Fibrinogen</b>	43 ± 2	3 ± 1	27 ± 1	39 ± 2

### 3.3.3. *Ex situ* Analysis of Protein Adhesion Using QCM

QCM provides an analytical technique with great sensitivity to monitor mass changes to allow for the quantification of the amount of material adhered to the surface of the sensor. The change in frequency ( $-\Delta f$ ) reported as a function of time is found in Figure 3.5 and is an average of 3 independent trials for each surface. Once mass is adsorbed onto the surface, for either the SAM or adhered protein, the bare gold sensor experiences a decrease in observed frequency. The QCM technique is conducted *ex situ*, which generates

a signal absent the hydration layer and is known as dry mass loading; and it is used as a comparative study to the *in situ* method of SPR, which includes the interaction with the hydration layer.<sup>54-57</sup> The absence of the hydration layer should result in mass loading values lower than with the presence of the hydration layer. Regardless of technique, the same trends are observed in both *in situ* and *ex situ* studies. The mass loading for each of the selected proteins for each of the adsorbates was calculated using Equation 3.1 and displayed in Table 3.5 and shown graphically in Figure 3.6.

**Table 3.5.** Calculated Values for Mass Loading of the SAMs after 1 h Exposure to 1 mg/mL of Protein in PBS Solution

Adsorbate	Mass (ng/cm <sup>2</sup> )			
	Protamine	Lysozyme	BSA	Fibrinogen
<b>C18SH</b>	329 ± 34	409 ± 67	493 ± 76	854 ± 80
<b>EG3C7SH</b>	218 ± 94	264 ± 12	223 ± 75	119 ± 30
<b>EG3C7-C7</b>	308 ± 40	314 ± 62	621 ± 72	471 ± 52
<b>EG3C7-C18</b>	398 ± 45	442 ± 76	644 ± 99	943 ± 83

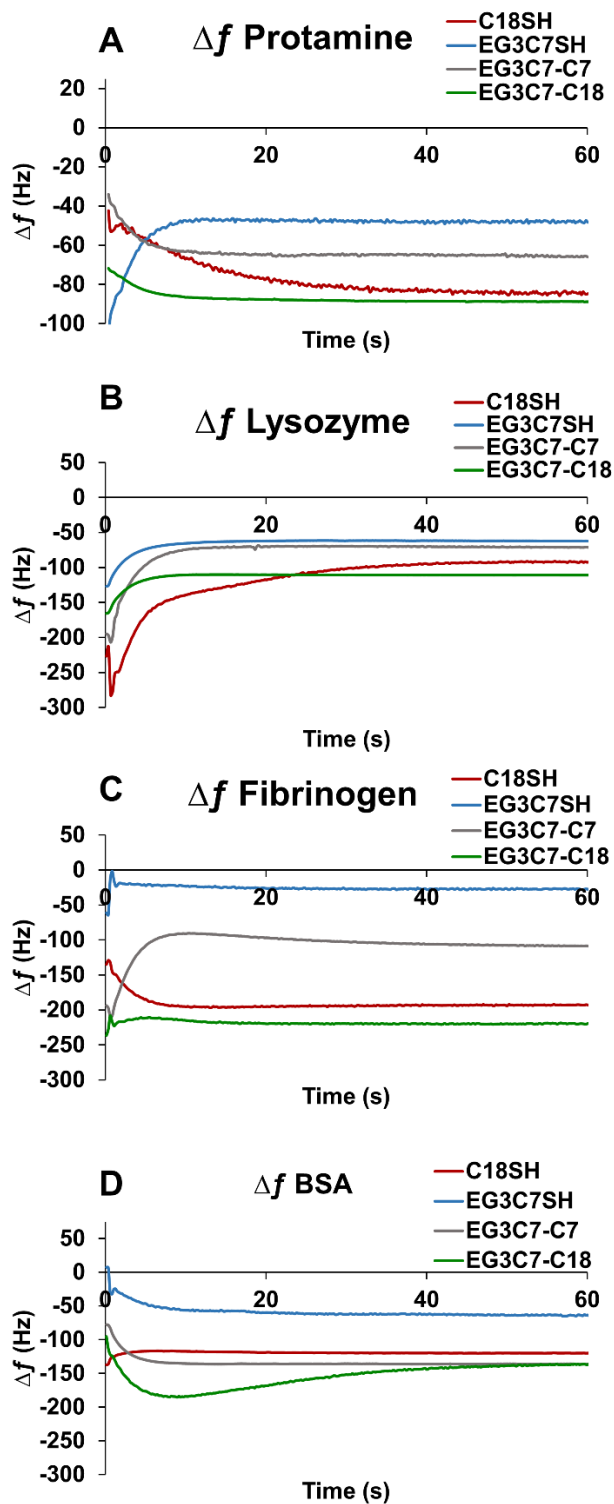


**Figure 3.5.** Change in frequency vs. time for SAMs derived from **C18SH**, **EG3C7SH**, and **EG3C7-C7**, and **EG3C7-C18** after 1 h exposure to 1 mg/mL of protein in PBS solution: (A) protamine, (B) lysosome, (C) BSA, and (D) fibrinogen.

After protein exposure to protamine, the adsorbates showed an increase in mass of 329 ng/cm<sup>2</sup>, 218 ng/cm<sup>2</sup>, 308 ng/cm<sup>2</sup>, and 398 ng/cm<sup>2</sup> for **C18SH**, **EG3C7SH**, **EG3C7-C7**, and **EG3C7-C18**, respectively. As expected, the **EG3C7SH** showed a lower mass loading when compared to the hydrophobic **C18SH** and the dual character bidentate dithiols, **EG3C7-C7** and **EG3C7-C18**. However, **EG3C7-C18** showed a greater mass loading when compared to **C18SH**, where **EG3C7-C7** had less mass loading than the **C18SH**. The overall trend was consistent regardless of the protein used, as represented with lysozyme having 409 ng/cm<sup>2</sup>, 264 ng/cm<sup>2</sup>, 314 ng/cm<sup>2</sup>, and 442 ng/cm<sup>2</sup> for **C18SH**, **EG3C7SH**, **EG3C7-C7**, and **EG3C7-C18**, and fibrinogen having 854 ng/cm<sup>2</sup>, 119 ng/cm<sup>2</sup>, 471 ng/cm<sup>2</sup>, and 943 ng/cm<sup>2</sup> for **C18SH**, **EG3C7SH**, **EG3C7-C7**, and **EG3C7-C18** respectively. The exposure to BSA is an exception where both of the SADTs (**EG3C7-C7** and **EG3C7-C18**) adhere more protein to the surface than the **C18SH** adsorbate, which is also noted in the SPR data and found to be 493 ng/cm<sup>2</sup>, 223 ng/cm<sup>2</sup>, 621 ng/cm<sup>2</sup>, and 644 ng/cm<sup>2</sup> for **C18SH**, **EG3C7SH**, **EG3C7-C7**, and **EG3C7-C18** respectively. This is likely a result of the charge interaction in combination with the hydrophobic areas or patches found on the protein surface leading to more favorable interactions with the protein resulting in 409 ng/cm<sup>2</sup>, 264 ng/cm<sup>2</sup>, 314 ng/cm<sup>2</sup>, and 442 ng/cm<sup>2</sup> for **C18SH**, **EG3C7SH**, **EG3C7-C7**, and **EG3C7-C18**, respectively, resulting in more adhesion to the surface of the adsorbate.

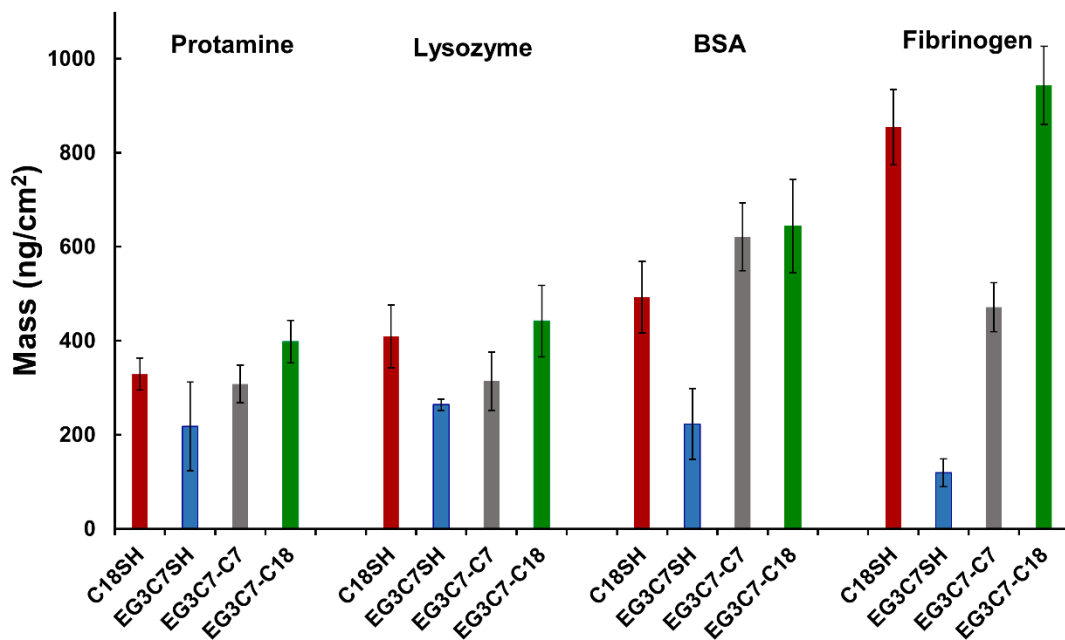


**Figure 3.6.** Graphical presentation of the calculated values for the mass loading of proteins onto the SAMs derived from **C18SH**, **EG3C7SH**, **EG3C7-C7**, and **EG3C7-C18** after exposure to 1mg/mL protein solution in PBS for 1 h.

The overall trend, where **EG3C7SH** < **C18SH** < **EG3C7-C7** < **EG3C7-C18** is confirmed by the mass loading, which is proportional to the  $\Delta f$  of the adsorbates after protein exposure and found in Figure 3.5. There is a smaller  $\Delta f$  for the SAMs exposed to the smaller molecular weight protein (e.g. protamine) and a greater  $\Delta f$  for the SAMs exposed to larger proteins (e.g. fibrinogen). This trend further supports the previous analysis and is indicative that the dual chemical heterogeneity of the interfaces of **EG3C7-C7** and **EG3C7-C18**, which generate interactions that confine the degree of freedom of the OEG chain, resulting in unfavorable interactions and the increase of protein adhesion. However, the shorter hydrocarbon chain dithiol **EG3C7-C7**, where the hydrocarbon chain plausibly lies below the helical OEG chain, lends to less restrictions resulting in lower protein adhesion when compared to **C18SH**.<sup>32,53</sup>

### 3.3.4. Evaluation of Surface Topography Using AFM

Imaging of biological materials and SAMs in order to determine surface topography of the resulting interactions has been done with the use of atomic force microscopy (AFM).<sup>58-65</sup> Herein, AFM was used to image the surface topography of each adsorbate after exposure to each protein to determine if any distinct differences in surface patterning can be identified.<sup>61,63,64,66</sup> The results of the AFM images for **C18SH**, **EG3C7SH**, **EG3C7-C7**, and **EG3C7-C18** surfaces are displayed in Figure 3.7 for protamine, Figure 3.8 for lysozyme, Figure 3.9 for BSA, and Figure 3.10 for fibrinogen. Each figure contains the image of the surface after exposure to each respective protein in a  $5\ \mu\text{m} \times 5\ \mu\text{m}$  and a  $1\ \mu\text{m} \times 1\ \mu\text{m}$  for the **C18SH**, **EG3C7SH**, **EG3C7-C7**, and **EG3C7-C18** SAMs.

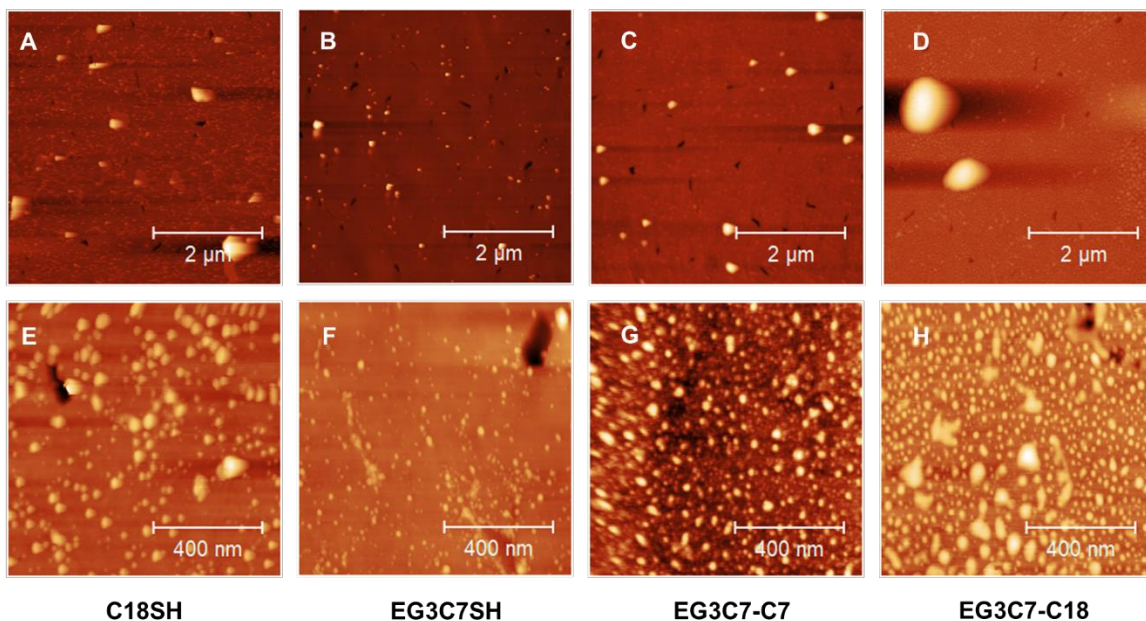


**Figure 3.7.** Topography after exposure to protamine for (A, E) **C18SH**, (B, F) **EG3C7SH**, (C, G) **EG3C7-C7**, and (D, H) **EG3C7-C18** at  $5\ \mu\text{m} \times 5\ \mu\text{m}$  (top) and at  $1\ \mu\text{m} \times 1\ \mu\text{m}$  (bottom).

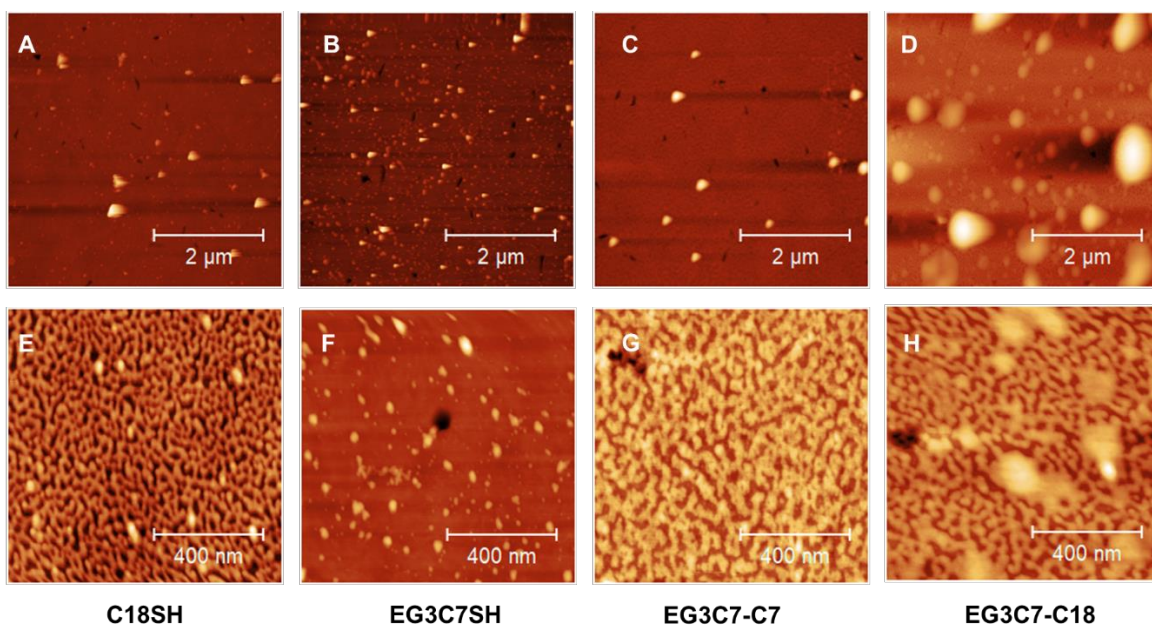


**Figure 3.8.** Topography after exposure to lysozyme for (A, E) **C18SH**, (B, F) **EG3C7SH**, (C, G) **EG3C7-C7**, and (D, H) **EG3C7-C18** at  $5\ \mu\text{m} \times 5\ \mu\text{m}$  (top) and at  $1\ \mu\text{m} \times 1\ \mu\text{m}$  (bottom).

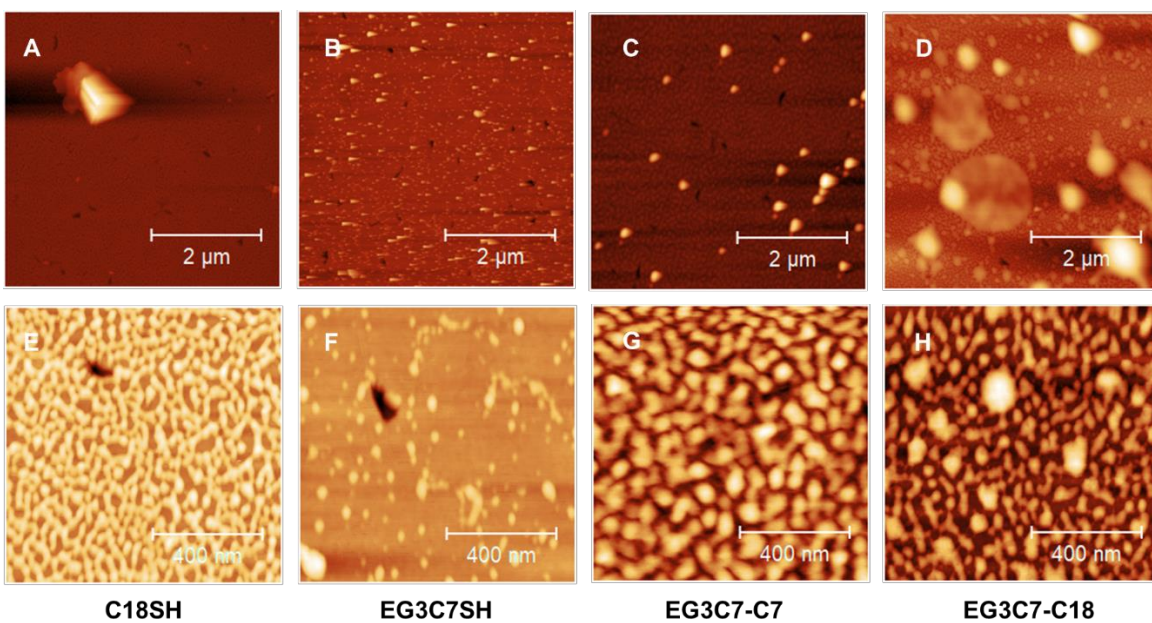


**Figure 3.9.** Topography after exposure to BSA for (A, E) **C18SH**, (B, F) **EG3C7SH**, (C, G) **EG3C7-C7**, and (D, H) **EG3C7-C18** at  $5\ \mu\text{m} \times 5\ \mu\text{m}$  (top) and at  $1\ \mu\text{m} \times 1\ \mu\text{m}$  (bottom).

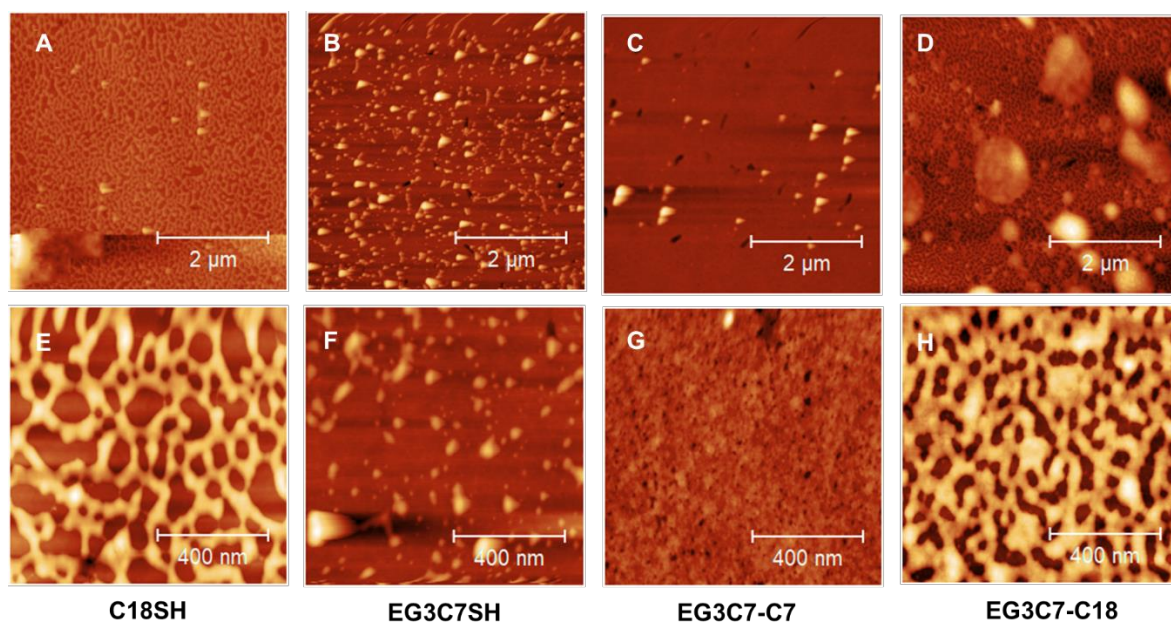


**Figure 3.10.** Topography after exposure to fibrinogen for (A, E) **C18SH**, (B, F) **EG3C7SH**, (C, G) **EG3C7-C7**, and (D, H) **EG3C7-C18** at  $5\ \mu\text{m} \times 5\ \mu\text{m}$  (top) and at  $1\ \mu\text{m} \times 1\ \mu\text{m}$  (bottom).

The results of the AFM imaging indicate different patterning on the surface of the adsorbate after exposure to the protein solutions.<sup>61-64,67</sup> For example, the **C18SH** surface has a lattice like patterning for the proteins lysozyme (Figure 3.8E), BSA (Figure 3.9E) and fibrinogen (Figure 3.10E) compared to the **EG3C7SH** surface, which lacks a lattice patterning on the surface for lysozyme (Figure 3.8F), BSA (Figure 3.9F), and fibrinogen (Figure 3.10F). The AFM images also indicate globular spots as seen with the brighter colored spots on the images indicating higher patches and likely more material on the surface of the **EG3C7-C18** SAM for each of the proteins, protamine (Figure 3.7H), lysozyme (Figure 3.8H), BSA (Figure 3.9H), and fibrinogen (Figure 3.10H). By simple comparison, it may be possible to distinguish qualitatively the amount of material adhered to the surface based on the patterning of the surface after protein exposure, but further statistical analysis and evaluation of the patterning of the surface may result in a means to

quantitatively determine the amount of material adhered to the adsorbate surface and identify a correlation to the previous analytical techniques and provide additional insight into the adsorbate-protein interaction.

Statistical analysis of the surface was performed using Gwyddion in order to determine the arithmetic average ( $R_a$ ) and the root mean square (Rms) of the peaks and valleys across the surface of the sample being imaged to determine the surface roughness.  $R_a$  and Rms are the most commonly used measurement values for surface roughness, as they are the easiest to obtain. Table 3.6 and Table 3.7 contains the surface roughness measurements for each adsorbate and protein with standard deviation for the  $R_a$  and Rms values, respectively. The  $R_a$  and Rms values are an average of 6 measurements for each surface and protein. The  $R_a$  and Rms values account for the peak and valley heights across the imaged surface and supplies information with respect to the patterning of the material on the surface of the adsorbate and is likely to increase as more material is adhered to the surface.

**Table 3.6.** The  $R_a$  Values of the Surface Roughness of the SAMs after Exposure to Proteins

Protein	$R_a$ (nm)			
	C18SH	EG3C7SH	EG3C7-C7	EG3C7-C18
<b>Protamine</b>	$1.47 \pm 0.42$	$0.48 \pm 0.07$	$1.08 \pm 0.19$	$1.62 \pm 0.14$
<b>Lysozyme</b>	$1.30 \pm 0.04$	$0.90 \pm 0.31$	$0.99 \pm 0.13$	$2.73 \pm 0.29$
<b>BSA</b>	$1.87 \pm 0.01$	$0.97 \pm 0.15$	$1.21 \pm 0.27$	$3.38 \pm 0.36$
<b>Fibrinogen</b>	$3.88 \pm 0.36$	$1.85 \pm 0.62$	$0.70 \pm 0.23$	$0.91 \pm 0.43$

**Table 3.7.** The Rms Values of the Surface Roughness of the SAMs after Exposure to Proteins

Protein	Rms (nm)			
	C18SH	EG3C7SH	EG3C7-C7	EG3C7-C18
Protamine	2.24 ± 0.66	0.88 ± 0.10	1.95 ± 0.49	2.17 ± 0.19
Lysozyme	1.65 ± 0.07	1.77 ± 0.65	1.33 ± 0.17	3.69 ± 0.48
BSA	2.20 ± 0.02	1.72 ± 0.30	1.93 ± 0.85	4.30 ± 0.68
Fibrinogen	4.74 ± 0.74	2.98 ± 0.10	1.05 ± 0.64	4.47 ± 0.62

Figure 3.11 graphically presents the  $R_a$  and Rms values and provides additional insight into the protein-adsorbate interface. The values for **EG3C7SH** in Table 3.6 show the roughness increases as the size of the protein increases. This trend is also noted with the **EG3C7-C18** adsorbate with Rms values of 2.17 nm, 3.69 nm, 4.30 nm, and 4.47 nm for protamine, lysozyme, BSA and fibrinogen, respectively. When **EG3C7SH** is compared to **EG3C7-C18**, it appears that **EG3C7SH** has lower surface roughness compared to **EG3C7-C18**, which is consistent with the previous analytical techniques. However, the trend is not as noticeable with the **C18SH** and the **EG3C7-C7** adsorbates. The surface roughness is a statistical average of the height maximums and height minimums, so it is possible that two surfaces can have different profiles and patterning with the same  $R_a$  and Rms values. Further evaluation of the surface statistical data to determine the height distribution density, essentially a histogram of the surface height profile, proves insightful in determining how the protein adheres to the adsorbate surface by providing clarification for the  $R_a$  and Rms values and is found in Figure 3.12.

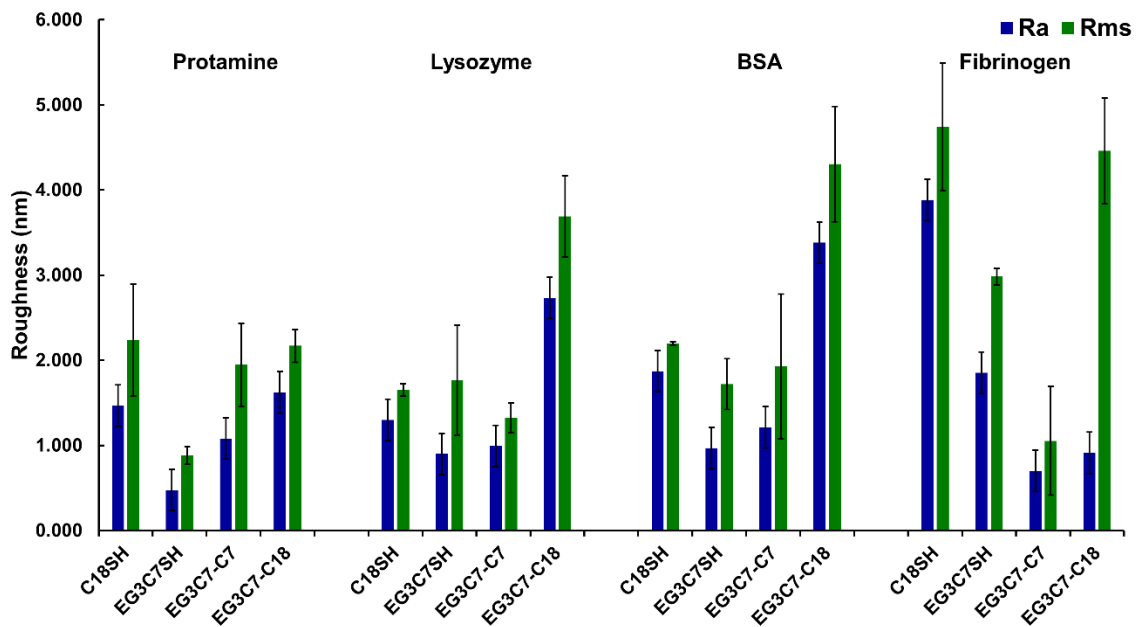


**Figure 3.11.** Average roughness ( $R_a$ ) and root mean square ( $R_{ms}$ ) values for each of the SAM surfaces (C18SH, EG3C7SH, EG3C7-C7, and EG3C7-C18) after exposure to protamine, lysozyme, BSA, and fibrinogen.

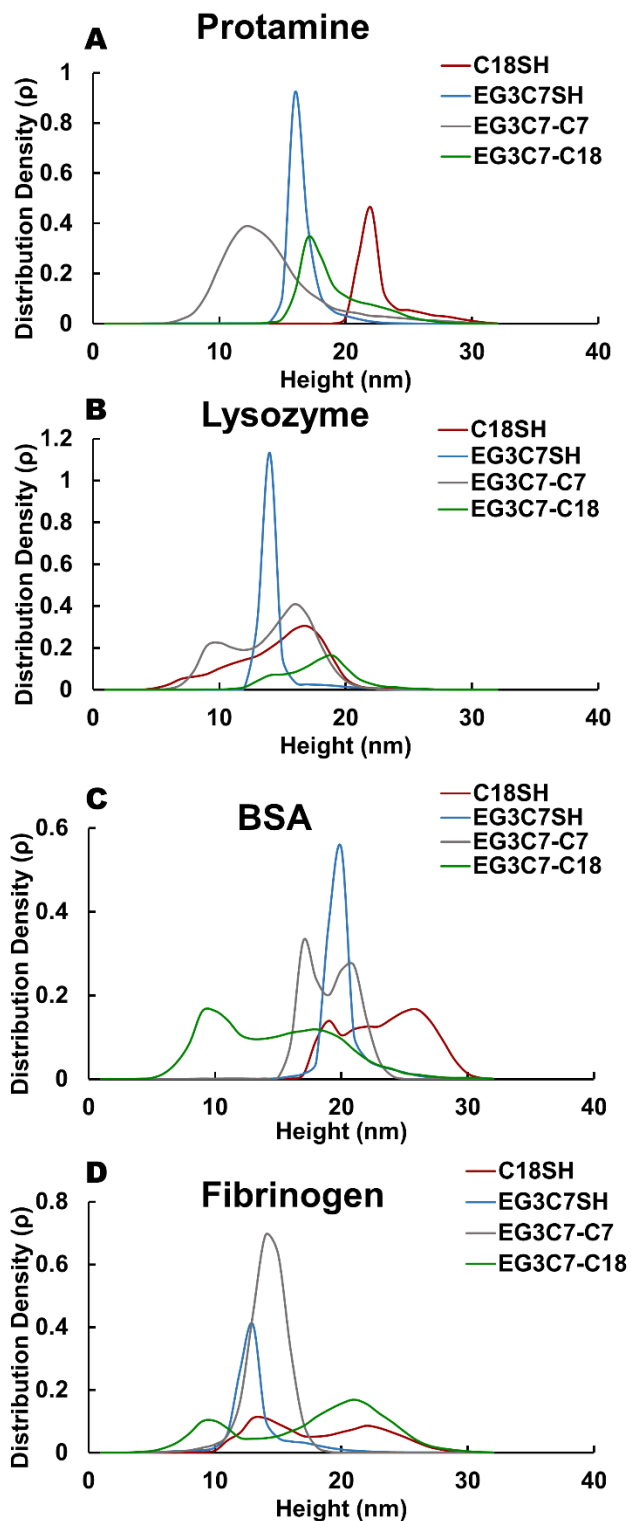


**Figure 3.12.** Height density distributions for each of the SAM surfaces (C18SH, EG3C7SH, EG3C7-C7, and EG3C7-C18) after exposure to (A) protamine, (B) lysozyme, (C) BSA, and (D) fibrinogen.

The height distribution density plots, with respect to the interactions with protamine (Figure 3.12A) indicate that the **EG3C7SH** adsorbate has a very narrow peak with a high density at ~17 nm, compared to **C18SH**, which has a lower density but a broader range, producing higher roughness values from 20-30 nm with the peak ~23 nm. The SADTs (**EG3C7-C7** and **EG3C7-C18**) have a similar peak shape which is very broad, ~15 nm, except **EG3C7-C7** has the greater density ~ 12 nm compared to **EG3C7-C18**, which has its greatest density, ~19 nm. With protamine, the density distribution plots indicate taller peaks for the **C18SH** and the **EG3C7-C18** surfaces, and are indicative of more material adhered to the surface compared to the **EG3C7-C7** and **EG3C7SH** SAMs. Lysozyme (Figure 3.12B) also indicates a sharp peak with high density at ~15 nm, compared to **C18SH**, **EG3C7-C7**, and **EG3C7-C18**, which all have broad distribution with two distinct peaks. For the **C18SH** and the **EG3C7-C7** SAM, the peaks pretty much overlap in distribution; however, the **EG3C7-C7** has two distinct peaks that are more prevalent and has slightly more density. This correlates to the  $R_a$  and  $R_{ms}$  values being similar. With the dual peaks for **EG3C7-C18**, the peaks are ~15 and ~ 20 nm compared to **EG3C7-C7** and **C18SH** which are ~10 and ~15 nm.

For the adsorbates and the interaction with BSA (Figure 3.12C), again **EG3C7SH** contains a sharp high distribution peak at about 20 nm, which would be expected for a larger molecular weight protein like BSA (55 KDa). **EG3C7-C18** has broad distribution ranging from a few nm to ~35nm, which would be indicative of the high  $R_a$  and  $R_{ms}$  values found in Figure 3.11. The **C18SH** SAM has higher peaks with a lower density distribution, compared to **EG3C7-C7**, yet the **EG3C7-C7** has a slightly lower peak range from ~15-25 nm but with almost double the density. Lastly, the **EG3C7SH** adsorbate shows another

narrow peak  $\sim 12$  nm with a small tail increasing the roughness slightly after the exposure to fibrinogen (Figure 3.12D). Again, the **EG3C7-C18** has a broad density distribution spanning from a few nm to  $\sim 35$  nm containing two distinct heights at  $\sim 10$  and 20 nm which is similar to **C18SH** adsorbate which has a slightly smaller span from  $\sim 5$  nm to 30 nm also displaying two distinct peak heights at  $\sim 15$  nm and  $\sim 24$  nm. This correlates to the similar  $R_a$  and  $R_{ms}$  values observed in Figure 3.11 and also more material adhered to the surface. However, **EG3C7-C7** SAM showed a single peak with a high density distribution at  $\sim 15$  nm, which would correlate to the surface roughness being lower for the **EG3C7-C7** with respect to the protein fibrinogen but still containing a similar amount of material compared to the **C18SH** and **EG3C7-C18** SAMs. The height density distributions explain the variations observed with surface roughness and also correlates to the previous observed trends. For **EG3C7SH**, the SPR and QCM techniques indicate similar amount of material adhered to the surface and the density distributions display a similar plot regardless of protein interaction which further supports this data.

The imaging of the surfaces after a variety of protein exposure using AFM to determine surface topography depict a means to distinguish differences in surfaces. The  $R_a$  and  $R_{ms}$  value differences can be explained by evaluation of the height density distributions and correlate to the observed trends seen with the other analytical techniques. AFM imaging and statistical evaluation further explains how the design of the molecular structure of the SADTs (**EG3C7-C7** and **EG3C7-C18**) with the introduction of the hydrocarbon chain segment in the confined space with the OEG chain segment decreases the protein resistant properties, as it restricts the degree of freedom of the OEG chain, resulting in more protein adhesion to the surface of the adsorbate. Although the **EG3C7-**

**C7** adsorbate, contains a shorter hydrocarbon chain segment which may lie underneath the helical OEG chain segment, additional protein adhesion is observed but in a fewer amount when compared to the **EG3C7-C18** adsorbate.

### 3.4. Conclusions

Surfaces coated with the adsorbates **C18SH**, a long chain hydrocarbon monothiol, **EG3C7SH**, a tri oligo (ethylene glycol) hydrocarbon chain monothiol, and the SADTs **EG3C7-C7** and **EG3C7-C18**, unsymmetrical dithiol structures containing both a hydrocarbon and OEG chains, were exposed to a diverse range of proteins to characterize the performance of the surfaces at the protein-adsorbate interface. Ellipsometry, SPR, QCM and AFM were used as complementary techniques to obtain a greater understanding of the antifouling properties of the SAMs with proteins. Proteins were selected with a range of properties to include: size, charge, hydrophobicity. As expected, due to the hydrophobic nature of the **C18SH** SAM, this surface adhered a large amount of protein when compared to the **EG3C7SH** SAM, which is known for its protein resistant properties. However, the dithiol **EG3C7-C18** with the addition of the long hydrocarbon chain restrained the degrees of freedom for the OEG chain which decreased the protein resistant properties and led to greater adhesion of proteins when compared to the **C18SH** SAM. Similar effects were also seen in the shorter chained dithiol **EG3C7-C7**, although with the possibility of the helical OEG segment residing over the shorter chain, the protein adhesion was lower than what was observed with the **EG3C7-C18** SAM.

The various analytical techniques utilized in this study were complimentary to each other, where the dithiol-based SAMs exhibited increased protein adhesion when compared

to the **EG3C7SH** adsorbate. However, the **EG3C7-C7** adsorbate adheres less than the **EG3C7-C18**. This is shown with the  $\Delta RU$  values in SPR and the decrease in the  $\Delta f$ , correlating to the mass loading of material on the surface. Imaging of the surface, with AFM, suggests a means to determine surface topography and roughness measurements to quantify the amount of protein adhered to the surface of the adsorbates. AFM data also correlates with the SPR and QCM results when analysis of height distribution densities are evaluated. The SPR data consistently show a greater  $\Delta RU$  for the **EG3C7-C18** over the **C18SH** adsorbate with an average increase of 249  $\Delta RU$  with almost 50% greater for protamine and lysozyme. The QCM shows a greater increase in mass loading of the **EG3C7-C18** adsorbate over the **C18SH** with an average value of 86  $g/cm^2$  ranging from 8%-31%.

Ellipsometry further confirmed the trend that **EG3C7-C18** maintains a greater change in thickness after protein exposure and is similar to **C18SH**, compared to the **EG3C7-C7** adsorbates which have lower thickness measurements. BSA showed aberrations to this trend by having a greater  $\Delta RU$  and mass loading for the **EG3C7-C7** adsorbate, and lower mass loading values for **EG3C7SH** and **EG3C7-C7** adsorbates for fibrinogen. This may be an indication of how charges on the surfaces of the proteins can interact with the adsorbate surface and alter the protein resistance properties. The developed protocols to provide a robust characterization of the properties for adsorbates with the interactions of proteins through the use of ellipsometry, SPR, QCM, and AFM. Applying the protocols to the unsymmetrical oligo (ethylene glycol) adsorbates have found that **EG3C7-C18** and **EG3C7-C7** have a disruption in the molecular structure that results in greater protein adhesion when compared to the monothiol **EG3C7SH**. This data implies

that the **EG3C7-C18** adsorbate could be further evaluated for possible sensor applications to test for the presence of small protein concentrations. Also, a dithiol molecule composed of two OEG chains on the same molecule can be synthesized and tested in comparison to the **C18SH** and the **EG3C7SH** to determine how the attachment of a like molecule may alter the properties after removing the conflicted interfaces but maintains the multiple attachment point with the dithiol molecule.

### 3.5. References

- (1) Brannon-Peppas, L. Poly(Ethylene Glycol): Chemistry and Biological Applications. *J. Control. Release* **2002**, *66*, 321–323.
- (2) Zalipsky, S.; Harris, J. M. Introduction to Chemistry and Biological Applications of Poly(Ethylene Glycol). In *Poly(ethylene glycol)*; American Chemical Society: Washington, 2009; pp 1–13.
- (3) Jeon, S. I.; Lee, J. H.; Andrade, J. D.; De Gennes, P. G. Protein-Surface Interactions in the Presence of Polyethylene Oxide. I. Simplified Theory. *J. Colloid Interface Sci.* **1991**, *142*, 149–158.
- (4) Taunton, H. J.; Toprakcioglu, C.; Fetters, L. J.; Klein, J. Forces between Surfaces Bearing Terminally Anchored Polymer Chains in Good Solvents. *Nature* **1988**, *332*, 712–714.
- (5) Banerjee, I.; Pangule, R. C.; Kane, R. S. Antifouling Coatings: Recent Developments in the Design of Surfaces That Prevent Fouling by Proteins, Bacteria, and Marine Organisms. *Adv. Mater.* **2011**, *23*, 690–718.

- (6) Yang, W.; Hamers, R. J. Fabrication and Characterization of a Biologically Sensitive Field-Effect Transistor Using a Nanocrystalline Diamond Thin Film. *Appl. Phys. Lett.* **2004**, *85*, 3626–3628.
- (7) Zhang, F.; Kang, E. T.; Neoh, K. G.; Huang, W. Modification of Gold Surface by Grafting of Poly(Ethylene Glycol) for Reduction in Protein Adsorption and Platelet Adhesion. *J Biomater Sci Polym Ed* **2001**, *12*, 515–531.
- (8) Sofia, S. J.; Premnath, V.; Merrill, E. W. Poly(Ethylene Oxide) Grafted to Silicon Surfaces: Grafting Density and Protein Adsorption. *Macromolecules* **1998**, *31*, 5059–5070.
- (9) Luk, Y. Y.; Tingey, M. L.; Hall, D. J.; Israel, B. A.; Murphy, C. J.; Bertics, P. J.; Abbott, N. L. Using Liquid Crystals to Amplify Protein-Receptor Interactions: Design of Surfaces with Nanometer-Scale Topography That Present Histidine-Tagged Protein Receptors. *Langmuir* **2003**, *19*, 1671–1680.
- (10) Prime, K. L.; Whitesides, G. M. Self-Assembled Organic Monolayers: Model Systems for Studying Adsorption of Proteins at Surfaces. *Science (80-. )*. **1991**, *252*, 1164–1167.
- (11) Prime, K. L.; Whitesides, G. M. Adsorption of Proteins onto Surfaces Containing End-Attached Oligo(Ethylene Oxide): A Model System Using Self-Assembled Monolayers. *J. Am. Chem. Soc.* **1993**, *115*, 10714–10721.
- (12) Clare, T. L.; Clare, B. H.; Nichols, B. M.; Abbott, N. L.; Hamers, R. J. Functional Monolayers for Improved Resistance to Protein Adsorption: Oligo(Ethylene Glycol)-

- Modified Silicon and Diamond Surfaces. *Langmuir* **2005**, *21*, 6344–6355.
- (13) Love, J. C.; Estroff, L. A.; Kriebel, J. K.; Nuzzo, R. G.; Whitesides, G. M. Self-Assembled Monolayers of Thiolates on Metals as a Form of Nanotechnology. *Chem. Rev.* **2005**, *105*, 1103–1170.
- (14) Wang, R. L. C.; Kreuzer, H. J.; Grunze, M. Molecular Conformation and Solvation of Oligo(Ethylene Glycol)-Terminated Self-Assembled Monolayers and Their Resistance to Protein Adsorption. *J. Phys. Chem. B* **2002**, *101*, 9767–9773.
- (15) Feldman, K.; Hähner, G.; Spencer, N. D.; Harder, P.; Grunze, M. Probing Resistance to Protein Adsorption of Oligo(Ethylene Glycol)-Terminated Self-Assembled Monolayers by Scanning Force Microscopy. *J. Am. Chem. Soc.* **1999**, *121*, 10134–10141.
- (16) Bain, C. D.; Troughton, E. B.; Tao, Y. T.; Evall, J.; Whitesides, G. M.; Nuzzo, R. G. Formation of Monolayer Films by the Spontaneous Assembly of Organic Thiols from Solution onto Gold. *J. Am. Chem. Soc.* **1989**, *111*, 321–335.
- (17) Li, L.; Chen, S.; Zheng, J.; Ratner, B. D.; Jiang, S. Protein Adsorption on Oligo(Ethylene Glycol)-Terminated Alkanethiolate Self-Assembled Monolayers: The Molecular Basis for Nonfouling Behavior. *J. Phys. Chem. B* **2005**, *109*, 2934–2941.
- (18) Sun, K.; Song, L.; Xie, Y.; Liu, D.; Wang, D.; Wang, Z.; Ma, W.; Zhu, J.; Jiang, X. Using Self-Polymerized Dopamine to Modify the Antifouling Property of Oligo(Ethylene Glycol) Self-Assembled Monolayers and Its Application in Cell Patterning. *Langmuir* **2011**, *27*, 5709–5712.

- (19) Krakert, S.; Ballav, N.; Zharnikov, M.; Terfort, A. Adjustment of the Bioresistivity by Electron Irradiation: Self-Assembled Monolayers of Oligo(Ethyleneglycol)-Terminated Alkanethiols with Embedded Cleavable Group. *Phys. Chem. Chem. Phys.* **2010**, *12*, 507–515.
- (20) Zorn, S.; Skoda, M. W. A.; Gerlach, A.; Jacobs, R. M. J.; Schreiber, F. On the Stability of Oligo(Ethylene Glycol) (C11EG 6OMe) SAMs on Gold: Behavior at Elevated Temperature in Contact with Water. *Langmuir* **2011**, *27*, 2237–2243.
- (21) Harder, P.; Grunze, M.; Dahint, R.; Whitesides, G. M.; Laibinis, P. E. Molecular Conformation in Oligo(Ethylene Glycol)-Terminated Self-Assembled Monolayers on Gold and Silver Surfaces Determines Their Ability To Resist Protein Adsorption. *J. Phys. Chem. B* **2002**, *102*, 426–436.
- (22) Shon, Y. S.; Lee, S.; Perry, S. S.; Lee, T. R. The Adsorption of Unsymmetrical Spiroalkanedithiols onto Gold Affords Multi-Component Interfaces That Are Homogeneously Mixed at the Molecular Level. *J. Am. Chem. Soc.* **2000**, *122*, 1278–1281.
- (23) Shon, Y. S.; Lee, S.; Colorado, R.; Perry, S. S.; Lee, T. R. Spiroalkanedithiol-Based SAMs Reveal Unique Insight into the Wettabilities and Frictional Properties of Organic Thin Films. *J. Am. Chem. Soc.* **2000**, *122*, 7556–7563.
- (24) Garg, N.; Carrasquillo-Molina, E.; Lee, T. R. Self-Assembled Monolayers Composed of Aromatic Thiols on Gold: Structural Characterization and Thermal Stability in Solution. *Langmuir* **2002**, *18*, 2717–2726.

- (25) Shon, Y.-S.; Lee, T. R. Chelating Self-Assembled Monolayers on Gold Generated from Spiroalkanedithiols. *Langmuir* **2002**, *15*, 1136–1140.
- (26) Shon, Y.-S.; Lee, T. R. A Steady-State Kinetic Model Can Be Used to Describe the Growth of Self-Assembled Monolayers (SAMs) on Gold. *J. Phys. Chem. B* **2002**, *104*, 8182–8291.
- (27) Shon, Y.-S.; Lee, T. R. Desorption and Exchange of Self-Assembled Monolayers (SAMs) on Gold Generated from Chelating Alkanedithiols. *J. Phys. Chem. B* **2002**, *104*, 8192–8200.
- (28) Lee, H. J.; Jamison, A. C.; Lee, T. R. Boc-Protected  $\omega$ -Amino Alkanedithiols Provide Chemically and Thermally Stable Amine-Terminated Monolayers on Gold. *Langmuir* **2015**, *31*, 2136–2146.
- (29) Chinwangso, P.; Jamison, A. C.; Lee, T. R. Multidentate Adsorbates for Self-Assembled Monolayer Films. *Acc. Chem. Res.* **2011**, *44*, 511–519.
- (30) Chinwangso, P.; Lee, H. J.; Lee, T. R. Self-Assembled Monolayers Generated from Unsymmetrical Partially Fluorinated Spiroalkanedithiols. *Langmuir* **2015**, *31*, 13341–13349.
- (31) Chinwangso, P.; St. Hill, L. R.; Marquez, M. D.; Randall Lee, T. Unsymmetrical Spiroalkanedithiols Having Mixed Fluorinated and Alkyl Tailgroups of Varying Length: Film Structure and Interfacial Properties. *Molecules* **2018**, *23*, 2632.
- (32) Chinwangso, P.; Lee, H. J.; Jamison, A. C.; Marquez, M. D.; Park, C. S.; Lee, T. R. Structure, Wettability, and Thermal Stability of Organic Thin-Films on Gold

Generated from the Molecular Self-Assembly of Unsymmetrical Oligo(Ethylene Glycol) Spiroalkanedithiols. *Langmuir* **2017**, *33* (8), 1751–1762.

- (33) Smith, R. K.; Reed, S. M.; Lewis, P. A.; Monnell, J. D.; Clegg, R. S.; Kelly, K. F.; Bumm, L. A.; Hutchison, J. E.; Weiss, P. S. Phase Separation within a Binary Self-Assembled Monolayer on Au{111} Driven by an Amide-Containing Alkanethiol. *J. Phys. Chem. B* **2001**, *105*, 1119–1122.
- (34) Jackson, A. M.; Myerson, J. W.; Stellacci, F. Spontaneous Assembly of Subnanometre-Ordered Domains in the Ligand Shell of Monolayer-Protected Nanoparticles. *Nat. Mater.* **2004**, *3*, 330–336.
- (35) Yaliraki, S. N.; Longo, G.; Gale, E.; Szleifer, I.; Ratner, M. A. Stability and Phase Separation in Mixed Self-Assembled Monolayers. *J. Chem. Phys.* **2006**, *125*, 74708.
- (36) Fetisov, E. O.; Siepmann, J. I. Structure and Phase Behavior of Mixed Self-Assembled Alkanethiolate Monolayers on Gold Nanoparticles: A Monte Carlo Study. *J. Phys. Chem. B* **2016**, *120*, 1972–1978.
- (37) Shevade, A. V.; Zhou, J.; Zin, M. T.; Jiang, S. Phase Behavior of Mixed Self-Assembled Monolayers of Alkanethiols on Au(111): A Configurational-Bias Monte Carlo Simulation Study. *Langmuir* **2001**, *17*, 7566–7572.
- (38) Akimov, Y.; Pam, M. E.; Sun, S. Kretschmann-Raether Configuration: Revision of the Theory of Resonant Interaction. *Phys. Rev. B* **2017**, *96*, 155433–155440.
- (39) Buttry, D. A.; Ward, M. D. Measurement of Interfacial Processes at Electrode Surfaces with the Electrochemical Quartz Crystal Microbalance. *Chem. Rev.* **1992**, *92*, 1355–

1379.

- (40) Sauerbrey, G. Verwendung von Schwingquarzen Zur Wägung Dünner Schichten Und Zur Mikrowägung. *Zeitschrift für Phys.* **1959**, *155*, 206–222.
- (41) Gamry Instruments. Basics of a Quartz Crystal Microbalance. *Spectrum* **2012**, *1*, 1–7.
- (42) Tsai, D. H.; Delrio, F. W.; Keene, A. M.; Tyner, K. M.; MacCuspie, R. I.; Cho, T. J.; Zachariah, M. R.; Hackley, V. A. Adsorption and Conformation of Serum Albumin Protein on Gold Nanoparticles Investigated Using Dimensional Measurements and in Situ Spectroscopic Methods. *Langmuir* **2011**, *27*, 2464–2477.
- (43) Bachmann, L.; Schmitt-Fumain, W. W.; Hammel, R.; Lederer, K. Size and Shape of Fibrinogen, 1. Electron Microscopy of the Hydrated Molecule. *Die Makromol. Chemie* **1975**, *176*, 2603–2618.
- (44) Colvin, J. R. The Size and Shape of Lysozyme. *Can. J. Chem.* **1952**, *30*, 831–834.
- (45) Bolan, C. D.; Klein, H. G. Blood Component and Pharmacologic Therapy for Hemostatic Disorders. In *Consultative Hemostasis and Thrombosis: Third Edition*; Saunders: Philadelphia, 2013.
- (46) Marucco, A.; Catalano, F.; Fenoglio, I.; Turci, F.; Martra, G.; Fubini, B. Possible Chemical Source of Discrepancy between in Vitro and in Vivo Tests in Nanotoxicology Caused by Strong Adsorption of Buffer Components. *Chem. Res. Toxicol.* **2015**, *28*, 87–91.
- (47) Parkes, M.; Myant, C.; Cann, P. M.; Wong, J. S. S. The Effect of Buffer Solution

Choice on Protein Adsorption and Lubrication. *Tribol. Int.* **2014**, *72*, 108–117.

- (48) Herrwerth, S.; Eck, W.; Reinhardt, S.; Grunze, M. Factors That Determine the Protein Resistance of Oligoether Self-Assembled Monolayers - Internal Hydrophilicity, Terminal Hydrophilicity, and Lateral Packing Density. *J. Am. Chem. Soc.* **2003**, *125*, 9359–9366.
- (49) Zwahlen, M.; Herrwerth, S.; Eck, W.; Grunze, M.; Hähner, G. Conformational Order in Oligo(Ethylene Glycol)-Terminated Self-Assembled Monolayers on Gold Determined by Soft X-Ray Absorption. *Langmuir* **2003**, *19*, 9305–9310.
- (50) Xiao, X. F.; Jiang, X. Q.; Zhou, L. J. Surface Modification of Poly Ethylene Glycol to Resist Nonspecific Adsorption of Proteins. *Fenxi Huaxue/ Chinese J. Anal. Chem.* **2013**, *41*, 445–453.
- (51) Michel, R.; Pasche, S.; Textor, M.; Castner, D. G. Influence of PEG Architecture on Protein Adsorption and Conformation. *Langmuir* **2005**, *21*, 12327–12332.
- (52) Bernhard, C.; Roeters, S. J.; Franz, J.; Weidner, T.; Bonn, M.; Gonella, G. Repelling and Ordering: The Influence of Poly(Ethylene Glycol) on Protein Adsorption. *Phys. Chem. Chem. Phys.* **2017**, *19*, 28182–28188.
- (53) Attwood, S.; Kershaw, R.; Udin, S.; Bishop, S.; Welland, M. Understanding Globular Protein Adsorption to Alkanethiol and Material Surfaces. *J. Mater. Chem. B Under Rev.* **2019**, *7*, 2349–2361.
- (54) Rickert, J.; Brecht, A.; Göpel, W. Quartz Crystal Microbalances for Quantitative Biosensing and Characterizing Protein Multilayers. *Biosens. Bioelectron.* **1997**, *12*,

567–575.

- (55) Levi, M. D.; Daikhin, L.; Aurbach, D.; Presser, V. Quartz Crystal Microbalance with Dissipation Monitoring (EQCM-D) for in-Situ Studies of Electrodes for Supercapacitors and Batteries: A Mini-Review. *Electrochem. commun.* **2016**, *67*, 16–21.
- (56) Ispas, A.; Bund, A. Electrochemical Quartz Crystal Microbalance. In *Encyclopedia of Applied Electrochemistry*; Springer: New York, 2014.
- (57) Smith, A. L. Chapter 5 The Quartz Crystal Microbalance. In *Handbook of Thermal Analysis and Calorimetry*; Elsevier B.V.: London, 2008.
- (58) Kushmerick, J. G.; Weiss, P. S. Scanning Probe Microscopes. In *Encyclopedia of Spectroscopy and Spectrometry*; Academic Press: Cambridge, 2016.
- (59) Dupont-Gillain, C. C.; Fauroux, C. M. J.; Gardner, D. C. J.; Leggett, G. J. Use of AFM to Probe the Adsorption Strength and Time-Dependent Changes of Albumin on Self-Assembled Monolayers. *J. Biomed. Mater. Res. - Part A* **2003**, *67A*, 548–558.
- (60) Allison, D. P.; Mortensen, N. P.; Sullivan, C. J.; Doktycz, M. J. Atomic Force Microscopy of Biological Samples. *Wiley Interdiscip. Rev. Nanomedicine Nanobiotechnology* **2010**, *2*, 618–634.
- (61) Jalili, N.; Laxminarayana, K. A Review of Atomic Force Microscopy Imaging Systems: Application to Molecular Metrology and Biological Sciences. *Mechatronics* **2004**, *14*, 907–945.

- (62) Variola, F. Atomic Force Microscopy in Biomaterials Surface Science. *Phys. Chem. Chem. Phys.* **2015**, *17*, 2950–2959.
- (63) Engel, A.; Lyubchenko, Y.; Müller, D. Atomic Force Microscopy: A Powerful Tool to Observe Biomolecules at Work. *Trends Cell Biol.* **1999**, *9*, 77–80.
- (64) Schönherr, H.; Vancso, G. J. Atomic Force Microscopy in Practice. In *Scanning Force Microscopy of Polymers*; Springer: Berlin, 2010.
- (65) Friedbacher, G. Atomic Force Microscopy (AFM). In *Surface and Thin Film Analysis: A Compendium of Principles, Instrumentation, and Applications, Second Edition*; Wiley-VCH: Weinheim, 2011.
- (66) Servoli, E.; Maniglio, D.; Aguilar, M. R.; Motta, A.; San Roman, J.; Belfiore, L. A.; Migliaresi, C. Quantitative Analysis of Protein Adsorption via Atomic Force Microscopy and Surface Plasmon Resonance. *Macromol. Biosci.* **2008**, *8* (12), 1126–1134.
- (67) Yablon, D. G. Overview of Atomic Force Microscopy. In *Scanning Probe Microscopy for Industrial Applications: Nanomechanical Characterization*; John Wiley & Sons, Inc.: Hoboken, 2013.

## Chapter 4. Characterization and Anti-fouling Performance of Mixed Bidentate

### Self-Assembled Monolayers

#### 4.1. Introduction

Chemical and physical properties like interfacial morphology and attributes of the functional groups on the surface of the adsorbate affect the wettability of materials.<sup>1,2,11-17,3-10</sup> Researchers have employed numerous techniques, including the development of nanostructures to generate surfaces containing defined interfacial functional groups to control the wettability of solid surfaces. Perhaps the most prevalent nanostructure used by researchers to control surface wettability is self-assembled molecular films.<sup>12-17</sup> Self-assembled monolayers (SAMs) provide a convenient methodology to generate proven reliability for the modification of a surface comprised of metal or metal oxides.<sup>18-20</sup>

Multiple strategies have utilized SAMs to achieve control of surface wettability, in a dynamic and reversible means through the incorporation of various adsorbates. Some adsorbates that contain the ability to control surface wettability in a dynamic and reversible means include: light-active adsorbates,<sup>14,15</sup> ion-exchange adsorbates,<sup>16</sup> and electric field-responsive adsorbates.<sup>12,13</sup> One limitation of using these adsorbates to control surface wettability is the requirement for an external stimuli. Additional investigations utilizing a mixture of adsorbates, by changing the ratios of the SAM development solutions, have proven applicable in controlling the wettability of gold surfaces, yet problems still exist.<sup>17,21-23</sup>

When alkanethiols, which contain a single attachment point at the S-Au interface are used to generate SAMs with varying ratios in development solutions, three factors

influence and limit the control over the surface wettability of the mixed SAMs.<sup>24-26</sup> First, the solution to surface composition can vary. Second, the adsorbate composition on the surface changes over time. These two limiting factors arise in large part to the character of the bonding between the adsorbate and the gold substrate. Since the S-Au bonds can be considered labile, alkanethiol adsorbates on gold surfaces are able to relocate and easily exchange with the adsorbates in the SAM development solution. Lastly, phase separation on both the macroscopic and microscopic levels can be observed which results in "islanding".<sup>24-26</sup>

Researchers have investigated various adsorbates in efforts to overcome the limitations imposed from monodentate alkanethiols to generate mixed SAMs with the ability to control surface wettability. Studies investigating phosphonic acid adsorbates have shown that surface migration is mitigated due to multiple surface interactions between the substrate and the phosphonic headgroups.<sup>17</sup> Adsorbates comprised of a mixture of CH<sub>3</sub>-terminated and HOCH<sub>3</sub>-terminated alkanethiols were investigated for their wettability and structural properties. The investigation showed that long methylene linkers improved stability of the mixed adsorbates, although it failed to show that all adsorbate compositions had linear wettability.<sup>27,28</sup> Additional studies investigated mixed SAMs generated by coadsorption from solutions containing equal amounts of alkyl and fluoroalkyl disulfides. Although the adsorbates contain multiple attachment points on the headgroups, the fixed 1:1 ratio of the terminal groups combined with the potential for cleavage on the surface, which can result in desorption back into the development solution; therefore, the study failed to generate adsorbates for controlled surface wettability.<sup>29,30</sup>

In continued efforts to generate a mixed SAM with the ability to enhance and control surface wettability, and overcome the limitations of the monodentate adsorbates, Lee and coworkers designed and synthesized a set of perfluoro- and *n*-alkyl-terminated adsorbates identified as **PFPDT** and **HDPDT**, which are found in Figure 4.1.<sup>5</sup> The custom-designed adsorbates contain a key structural feature comprised of a dithiol headgroup that enhances the stability of the mixed SAMs as shown in previous studies.<sup>31–33</sup> Bidentate adsorbates have proven to bind strongly with the gold surface which results in increased resistance to desorption and exchange with thiols in the development solution.<sup>31</sup> Analysis of the mixed SAMs generated from the coadsorption of solutions with multiple ratios of the bidentate adsorbates showed the formation of mixed monolayers with composition ratios that closely aligned with the development solutions. Additionally, solution-phase displacement tests revealed remarkable stability of the SAMs.<sup>5</sup>

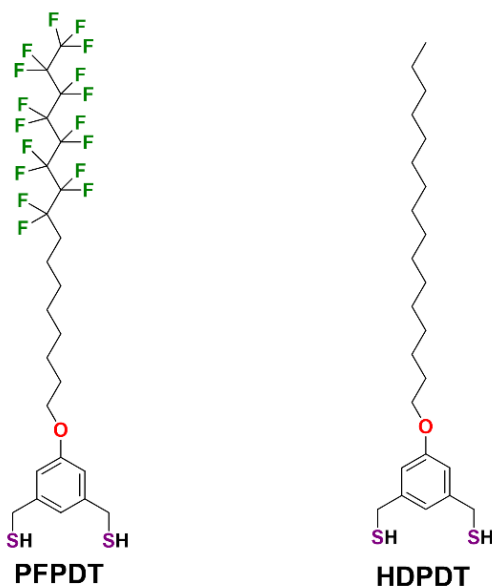


**Figure 4.1.** Molecular structures of the bidentate adsorbates, **PFPDT** and **HDPDT**, used to derive mixed SAMs in this study.

Herein, we investigate the interaction of various ratios of mixed SAMs, as described in Table 4.1 with multiple proteins to assess the ability of the surfaces to resist protein adhesion. Specifically, we prepared SAMs generated from binary mixtures of hydrocarbon adsorbates (**HDPDT**) and perfluorinated adsorbates (**PFPDT**). The SAMs were prepared alongside fully perfluorinated and hydrocarbon adsorbates to compare the performance of the mixed SAMs with the single component SAMs, and to evaluate the impact of the mixed composition on protein resistance. The proteins, protamine, lysozyme, bovine serum albumin (BSA), and fibrinogen were selected for this investigation to incorporate a wide-range of proteins in order to note any distinctions in response to the specific protein properties. We hypothesized that the chemical heterogeneity of the interface, due to the mixed composition of the SAM, will result in increased favorable interactions between the SAMs and the contacting proteins. Specifically, greater amounts of the hydrocarbon adsorbate in the mixed SAMs will lead to enhanced protein adhesion. The SAMs were characterized qualitatively and quantitatively with ellipsometry, X-ray photoelectron spectroscopy (XPS), and quartz crystal microbalance (QCM). The protein resistance properties of the generated films were characterized with optical ellipsometry, quartz crystal microbalance (QCM), and atomic force microscopy (AFM).

## **4.2. Experimental Section**

### **4.2.1. Materials**

Gold shot (99.999%) was purchased from Kamis, Inc., and chromium rods (99.9%) were purchased from Kurt J. Lesker Company and used as received. Polished single-crystal Si(100) wafers were purchased from University Wafer were rinsed with absolute

ethanol (EtOH, 200 proof, AAPER Alcohol and Chemical Co.) before use. Polished AT-cut quartz crystal microbalance sensors coated with Ti and plated with 1000 Å of gold, oscillating at a 10 MHz frequency, were purchased from Novatech. NTESPA (MPP-11220-10) AFM cantilevers comprised from antimony (n)-doped silicon tips with reflective aluminum coating were used as received from Bruker. Ultra-flat gold, with 1000 Å of gold on a silicon wafer, was purchased from Platypus technology and used as received.

The adsorbates, 5-(9,9,10,10,11,11,12,12,13,13,14,14,15,15,16,16,16-heptafluorohexadecyloxy)-1,3-phenylene)dimethanethiol (**PFPDT**) and 5-(hexadecyloxy)-1,3-phenylene)dimethanethiol (**HDPDT**) were synthesized according to procedures found in the literature<sup>5</sup>. All chemicals were used as received unless otherwise noted. Sulfuric acid (H<sub>2</sub>SO<sub>4</sub>), hydrogen peroxide (30% H<sub>2</sub>O<sub>2</sub>), and tetrahydrofuran (THF), were purchased from Avantor Performance Materials. Fibrinogen, lysozyme, bovine serum albumin, and protamine were purchased from Sigma-Aldrich. Phosphate Buffer Solution (PBS) 10x, from GenDepot, was diluted to 1x using water (H<sub>2</sub>O) generated from a Milli-Q water system with resistance of 18.2 MΩ.

#### **4.2.2. Preparation of Substrates**

A thermal evaporator was used to coat gold onto Si(100) wafers at a vacuum pressure  $\leq 6 \times 10^{-5}$  torr to prepare the gold substrates used in obtaining the ellipsometric thickness measurements and in the X-ray photoelectron spectroscopy studies. Under ultrahigh pressure, an initial 100 Å of a chromium adhesion layer was deposited; followed by the deposition of a 1000 Å gold layer at a rate of 0.5 Å/s. Immediately prior to preparation of the SAMs, QCM sensors required submersion in piranha solution, then followed by rinsing with copious amounts of water (H<sub>2</sub>O), absolute ethanol, and finally

dried in a stream of ultra-pure nitrogen gas. *Caution: Piranha solution reacts violently with organic materials and should be handled carefully!*

### 4.2.3. Preparation of SAMs

Glass vials containing the SAM solution were previously cleaned using piranha solution (3:1 mixture of concentrated H<sub>2</sub>SO<sub>4</sub>: H<sub>2</sub>O<sub>2</sub>), rinsed with copious amounts of deionized water, and finally with absolute ethanol. The organic thin films were prepared by immersing the freshly prepared substrates (evaporated gold, QCM, or ultra-flat gold on silica) in ethanolic solutions containing the binary mixture of the bidentate adsorbates, as found in Table 4.1 with a set of abbreviations also provided. The surfactant ratios were varied while maintaining the overall thiol solution at a concentration of 0.1 mM. All substrates were incubated at rt for 48 h to equilibrate, rinsed with THF, absolute ethanol, and then dried with a stream of ultra-pure nitrogen prior to characterization.

**Table 4.1.** Mole Fractions of Adsorbates Used to Generate the Mixed SAMs

Adsorbate Abbreviation	Mole Fraction of Bidentate Adsorbates in the Development Solution <sup>A</sup>	
	PF PDT	HD PDT
<b>PF PDT 1</b>	1.00	0.00
<b>PF PDT75</b>	0.75	0.25
<b>PF PDT50</b>	0.50	0.50
<b>PF PDT25</b>	0.25	0.75
<b>HD PDT 1</b>	0.00	1.00

<sup>A</sup>The overall thiol concentration was maintained at 0.1 mM.

#### **4.2.4. Protein Preparation/Exposure**

Protein solutions were prepared by dissolving 1 mg of protein in 1 mL of 1x PBS buffer solution to make a 1 mg/mL concentration, followed by sonication for 15 min. The protein solutions and buffers were filtered with a 0.2  $\mu\text{m}$  filter, prior to use. All substrates (thermally evaporated Au samples, QCM sensors, and ultra-flat gold) were immersed in the protein solutions for 1 h for saturation of protein on the surface of the SAMs, followed by a rinse with 1x PBS buffer, water ( $\text{H}_2\text{O}$ ), and then dried with a stream of ultra-pure nitrogen gas.

#### **4.2.5. Ellipsometry Measurements**

A J. A. Woolam Alpha SE ellipsometer at an incident angle of  $70^\circ$ , and a refractive index of 1.45 was used to obtain the monolayer thickness for each substrate sample. Data processing was carried out using the CompleteEase software from J. A. Woolam. The thickness values were determined with the software using a Cauchy method with  $A = 1.40$ ,  $B = 0.01$ , and  $C = 0.00$ . The reported thickness values are an average of 24 measurements (3 independent trials of 4 slides per adsorbate with 2 measurements for each slide). Thickness measurements were taken after immersion of the gold slide in the respective SAM development solution at rt for 48 h. To determine the thickness after exposure to protein solutions, the substrates containing the SAMs were immersed in protein solutions for 1 h to allow saturation of the surface with the protein.

Removal from the protein solution was followed by rinsing with 1x PBS buffer followed by water, and dried with a stream of ultra-pure nitrogen gas prior to measuring the ellipsometric thickness. Calculation of the change in thickness occurs by subtracting

the initial thickness value of the SAM from the thickness measurement of the SAM after exposure of the protein. The reported thickness measurements of the SAMs after protein exposure are from the evaporated gold surface, as there were no distinguishable differences among the various surfaces. The reported values are an average of 6 measurements (2 measurements per slide with 3 individual trials per adsorbate and protein). All surfaces (evaporated gold, SPR, QCM, and AFM) were characterized for the formation of the SAM by using optical ellipsometry.

#### **4.2.6. X-ray Photoelectron Spectroscopy (XPS) Measurements**

X-ray photoelectron spectra of the SAMs on freshly evaporated gold were obtained using a PHI 5700 X-ray photoelectron spectrometer equipped with a monochromatic Al K $\alpha$  X-ray source ( $h\nu = 1486.7$  eV) incident at 90° relative to the axis of a hemispherical energy analyzer. In a base pressure of  $2 \times 10^{-8}$  torr, ultra-high vacuum environment, the spectrometer analyzed a 2 mm diameter spot with high resolution and pass energy of 23.5 eV, with a photoelectron takeoff angle of 45° from the surface. The spectra were collected at rt and the binding energies were referenced to the Au 4f $_{7/2}$  peak at 84.0 eV.

#### **4.2.7. Quartz Crystal Microbalance Measurements**

The parallel and series frequency ( $f$ ) measurements of functionalized AT-cut quartz crystal microbalance sensors were obtained simultaneously using a Gamry eQCM at the bare gold state, SAMs layer, and again after exposure to protein. Normalization of the frequency was completed by taking readings of the bare gold sensor, after SAM formation, and after protein exposure. The reported values are an average of the resonant frequency after stabilization of the eQCM, which maintains a continuous driving voltage to the

piezoelectric crystal. Voltage is applied to the sensor to excite it near the resonant frequency. Once voltage is applied to a thin piezoelectric crystal sensor sandwiched between two Au plates acting as electrodes, a mechanical shear wave modulate and a vibrational mode is produced from an alternating electric field on either side of the crystal, generating a resonate frequency. When material adheres to the surface of the sensor, a decrease in resonate frequency ( $\Delta f$ ) is observed and is proportional to the change in mass ( $\Delta m$ ). Quantification of the mass loading of each sensor for the SAM and the protein was determined using Equation 4.1, known as the Sauerbrey equation.<sup>34-36</sup>

$$\Delta m = -C_f \Delta f \quad (4.1)$$

Where  $C_f$  (the mass sensitivity constant) is  $-226 \mu\text{g Hz}^{-1} \text{cm}^{-2}$  for a 10 MHz AT-cut QCM crystal.<sup>36</sup>

#### **4.2.8. Atomic Force Microscopy Imaging and Evaluation**

The SAMs on ultra-flat gold were exposed to the respective protein solution for 1 h, rinsed, dried, and was imaged within 2 h of removing from the protein solution. All AFM images were obtained in air using an Agilent 5000 atomic force microscope in acoustic (AC) mode with NTESPA AFM cantilevers made from antimony (n)-doped silicon tips with reflective aluminum coating. Gwyddion was used to process all images and to obtain the arithmetic average ( $R_a$ ), root mean square (RMS), and height density plots. Each surface was imaged at least six times, and surface roughness measurements include standard deviations.

### 4.3. Results and Discussion

#### 4.3.1. Characterization of SAMs Formation with Varied Surfactant Ratios

SAM formation was done following previous studies in the literature,<sup>5,37</sup> where the gold substrates were immersed in ethanolic solutions containing the various ratios of adsorbates, while maintaining an overall thiol concentration of 0.1 mM; the mole fractions of the thiols used in this study are found in Table 4.1. The adsorbates were allowed to incubate for 48 h to ensure the mixed SAMs reached complete equilibrium. Characterization of the mixed SAM surfaces was completed prior to the investigation of the interactions with the proteins. Characterization was completed using ellipsometry, XPS, and QCM. Ellipsometry was used to confirm SAM formation by determining film thickness with reported values found in Table 4.2; all thicknesses were consistent with reported values in the literature.<sup>5</sup> XPS was used to qualitatively and quantitatively analyze the SAMs which includes the characterization of surface bonds and determination of atomic composition. Lastly, QCM was used to correlate mass loading ratios of the SAMs to the ratios of the development solutions.

**Table 4.2.** Ellipsometric Film Thickness Values of the Mixed SAMs

Adsorbate	PF PDT1	PF PDT75	PF PDT50	PF PDT25	HDPDT1
Thickness (Å)	21 ± 2	21 ± 1	21 ± 2	21 ± 1	20 ± 2

##### 4.3.1.1. Characterization by XPS

XPS was used to examine the surface composition of the mixed SAM adsorbates by analyzing the high resolution XPS spectra of the Au 4f, C 1s, F 1s, and S 2p regions are

shown in Figure 4.2. The peaks at  $\sim 291$  eV and  $\sim 293$  eV are characteristic of the perfluorocarbons,<sup>38,39</sup> and the peaks at  $\sim 285$  eV are characteristic of the saturated hydrocarbons.<sup>32,33</sup> The peak intensities showed systematic decrements associated with the perfluorocarbon moieties that correlate with the changes in the adsorbate ratios of the development solutions for the mixed SAM adsorbates (see Figure 4.2B). These results indicate that the **PFPDT** and the **HDPDT** adsorbates form mixed SAMs that vary with the ratios of the development solution and are in agreement with the literature.<sup>5</sup> The peaks at  $\sim 688$  eV showed systematic decrements associated with the perfluorocarbon moieties to further confirm the correlation of the adsorbate ratios of the development solutions for the mixed SAM adsorbates (see Figure 4.2C). The peaks at  $\sim 162$  eV are indicative of thiol bound to the Au substrate (see Figure 4.2D). The Au 4f spectra indicates the gold substrate is present and was used for normalization (see Figure 4.2A).

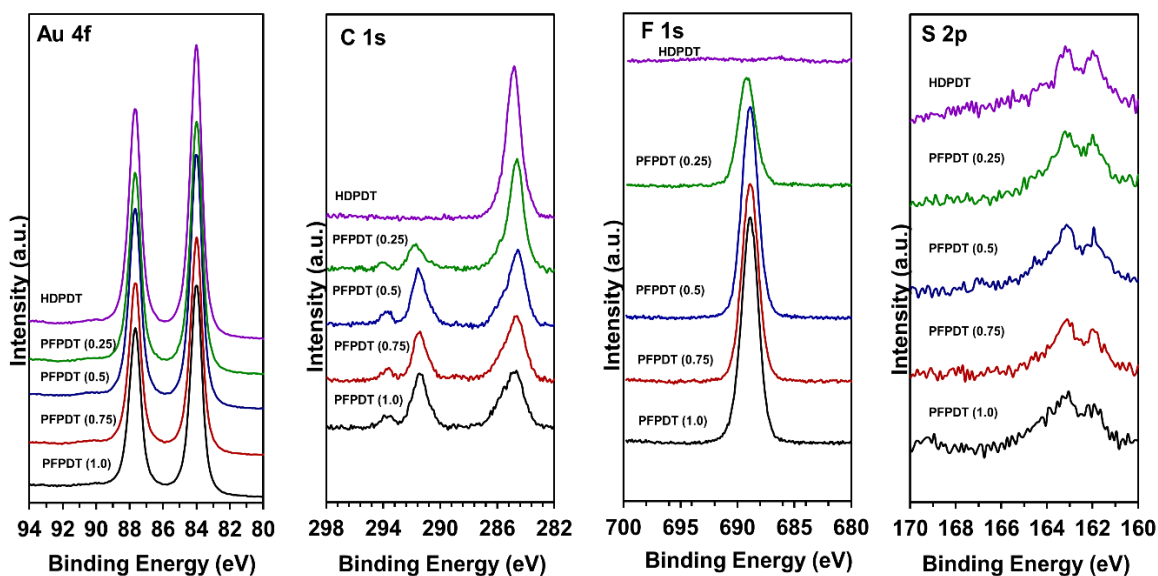


**Figure 4.2.** X-ray photoelectron spectra of the (A) Au 4f, (B) C 1s, (C) F 1s, and (D) S 2p regions of the mixed SAMs derived from the bidentate alkanethiols (**PFPDT** and **HDPDT**).

Quantitative analysis of the composition of the adsorbate ratios for the mixed SAMs was calculated using the F/Au and the F/C ratios from the integrated peaks associated with the spectral data of the Au 4f, C 1s, and the F 1s regions of the X-ray photoelectron spectra (see Figure 4.3). The combinations of the mixed SAMs exhibit a trend that is almost a linear decrease with respect to the **PF PDT** fraction present in the development solutions for the F/Au and the F/C ratios.<sup>5</sup> Both the quantitative and qualitative analysis of the elemental composition is consistent for the F 1s and the C 1s X-ray photoelectron spectra and confirms that ratios of the mixed SAMs composition as described in Table 4.1.<sup>5</sup>

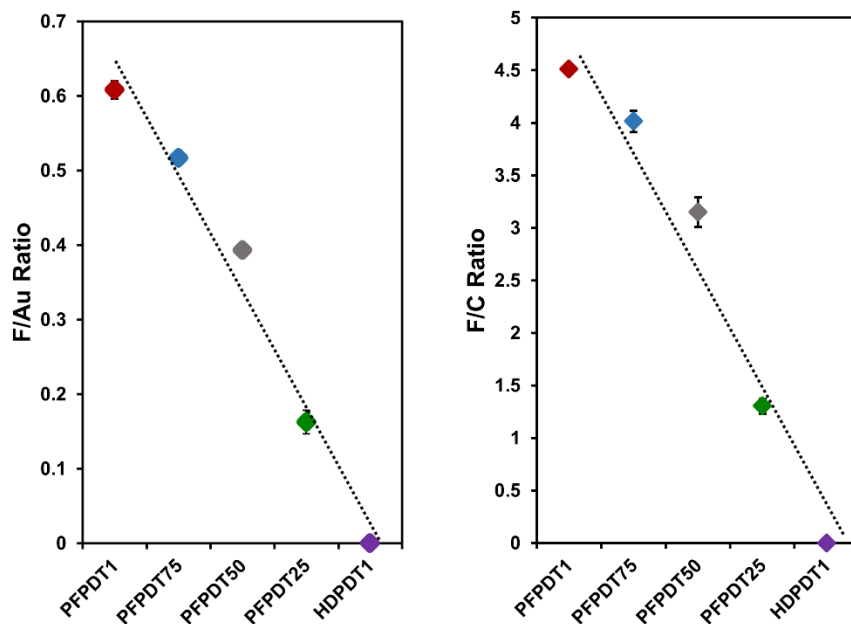


**Figure 4.3.** XPS elemental composition for the mixed SAMs derived from the bidentate alkanethiols in ethanol. (A) The fluorine to carbon (F/C) ratios and (B) the gold to fluorine (Au/F) ratio. Error bars indicate the standard deviation for the data. Error bars not visible fall within the symbols.

#### 4.3.1.2. QCM Characterization of the Mixed SAMs

The amount of adsorbate chemisorbed onto the substrate was measured with a QCM by subtracting the frequency measured in Hertz (Hz) of the formed adsorbate from

the initial frequency reading of the bare sensor, prior to SAM formation. Using the Sauerbrey equation (Equation 4.1), the  $\Delta m$  can be calculated from the  $\Delta f$  and is presented in Figure 4.4. When considering the mass loading of the **PF PDT1** and **HDPDT1** sensors to be 609 ng/cm<sup>2</sup> and 304 ng/cm<sup>2</sup> respectively, assuming a molecule for molecule loading and **PF PDT1** and **HDPDT1** are considered 100%. The ratios of the other mass loadings of the SAMs show a decrease in mass that correlates to the ratios of the development solutions.

For example, **PF PDT75** is 75% **PF PDT** and 25% **HDPDT**, where the mass loading of  $547 \pm 119$  ng/cm<sup>2</sup> shows a decrease in mass and correlates to the theoretical value of 533 ng/cm<sup>2</sup> when compared to the **PF PDT1** sensor. Likewise, **PF PDT50** which is a 50% mixture of **PF PDT** and **HDPDT**, shows a decrease in mass at of  $494 \pm 70$  ng/cm<sup>2</sup>, also correlates to the theoretical mass of 457 ng/cm<sup>2</sup> when compared to the **PF PDT1** sensor. However, the **PF PDT25** surface is a 25% **PF PDT** and 75% **HDPDT** and shows a slightly lower mass loading of  $307 \pm 47$  ng/cm<sup>2</sup>, compared to the theoretical mass value of 380 ng/cm<sup>2</sup> compared to the **PF PDT1** sensor which may be a result of additional **HDPDT1** occupying the space on the surface allowing less space for the helical fluorinated molecules to be present. The QCM mass loading of the surface is in correlation with the XPS data (*vide supra*), which shows that the SAMs formed from the mixed adsorbate development solutions generate SAM surfaces with comparable percentages.

**Table 4.3.** Mass Loading of Surfaces Coated with Mixed SAMs and Theoretical Values

Adsorbate	PF PDT1	PF PDT75	PF PDT50	PF PDT25	HDPDT1
Theoretical Mass (ng/cm <sup>2</sup> )	609	533	457	380	304
Actual Mass (ng/cm <sup>2</sup> )	609 ± 79	547 ± 119	494 ± 70	307 ± 47	304 ± 104

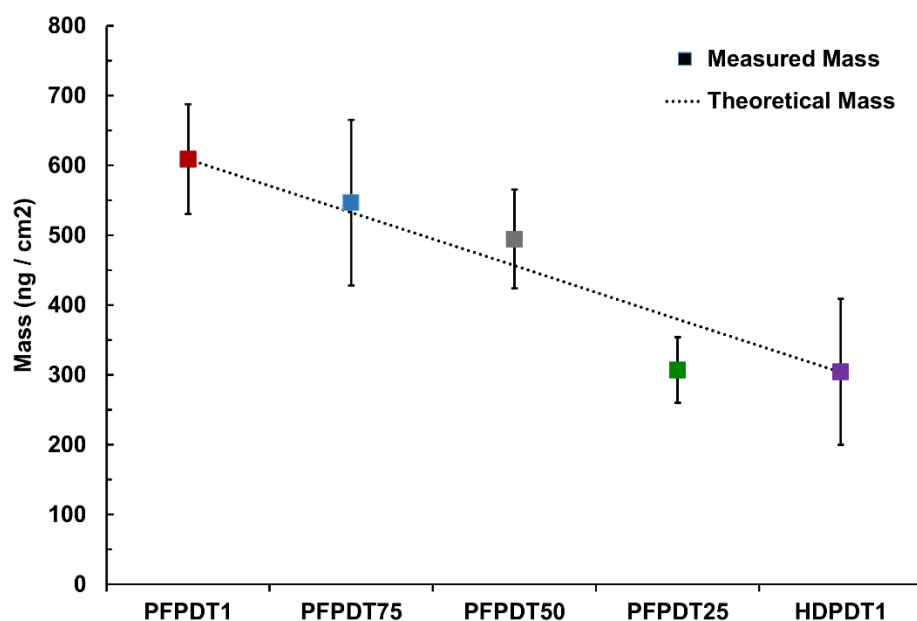


**Figure 4.4.** Mass loading of the SAMs on QCM sensors compared to the theoretical values.

#### 4.3.2. Anti-fouling Properties of the Mixed SAMs

Four proteins were selected with a range of properties to evaluate how the protein properties may influence adhesion to the SAM surfaces. The proteins were selected based on size, isoelectric point (pI), and molecular weight. A list of the protein properties are found in Table 4.4 and include commonly used proteins, such as bovine serum albumin (BSA) with a molecular weight of 55 KDa,<sup>40</sup> and fibrinogen, a larger molecular weight

protein with 340 KDa, but also has a neutral isoelectric point and tends to be a sticky protein.<sup>41</sup> Other proteins included for their smaller size and isoelectric points which produce a charged surface are lysozyme and protamine.<sup>42,43</sup> The variety of proteins with a diverse set of properties allows for evaluation of protein interactions with the surface of the adsorbates. Since the proteins were all stable in phosphate buffer solution (PBS), the protein solutions were prepared in PBS. The surfaces were exposed to PBS to ensure no aberrations resulting from the buffer were observed prior to exposure to protein solutions.<sup>44,45</sup> Several analytical techniques were selected to analyze the adhesion of proteins to the surface of the adsorbates and include ellipsometry, quartz crystal microbalance (QCM), and atomic force microscopy (AFM).

**Table 4.4.** Physical Properties of Proteins Examined in this Investigation

<b>Protein</b>	<b>BSA<sup>40</sup></b>	<b>Fibrinogen<sup>41</sup></b>	<b>Protamine<sup>43</sup></b>	<b>Lysozyme<sup>42</sup></b>
<b>Molecular Weight</b>	55 KDa	340 KDa	4 KDa	14 KDa
<b>pI</b>	4.8	5.7	12.1	11.1
<b>Shape</b>	Prolate Ellipsoid <sup>a</sup>	Cylindrical <sup>b</sup>	Spherical	Stubby Prolate Ellipsoid
<b>Size (dia.)</b>	140 × 40 × 40 Å	450 × 90 Å	5 Å	18 Å <sup>c</sup>

<sup>a</sup> where a=b<c

<sup>b</sup> with round ends

<sup>c</sup> diameter

#### 4.3.2.1. Quartz Crystal Microbalance Analysis of Protein Adhesion

Evaluation of mass loading of the proteins onto each adsorbate surface was evaluated by measuring the change in frequency of the sensor coated with the adsorbate

and subtracting the value from the frequency measured after protein exposure. The change in frequency  $\Delta f$  is used to calculate the change in mass ( $\Delta m$ ) using Equation 4.1, and the reported values are found in Table 4.5 and graphically presented in Figure 4.5. The calculated values are an average of at least 3 independent trials for each protein on each substrate.

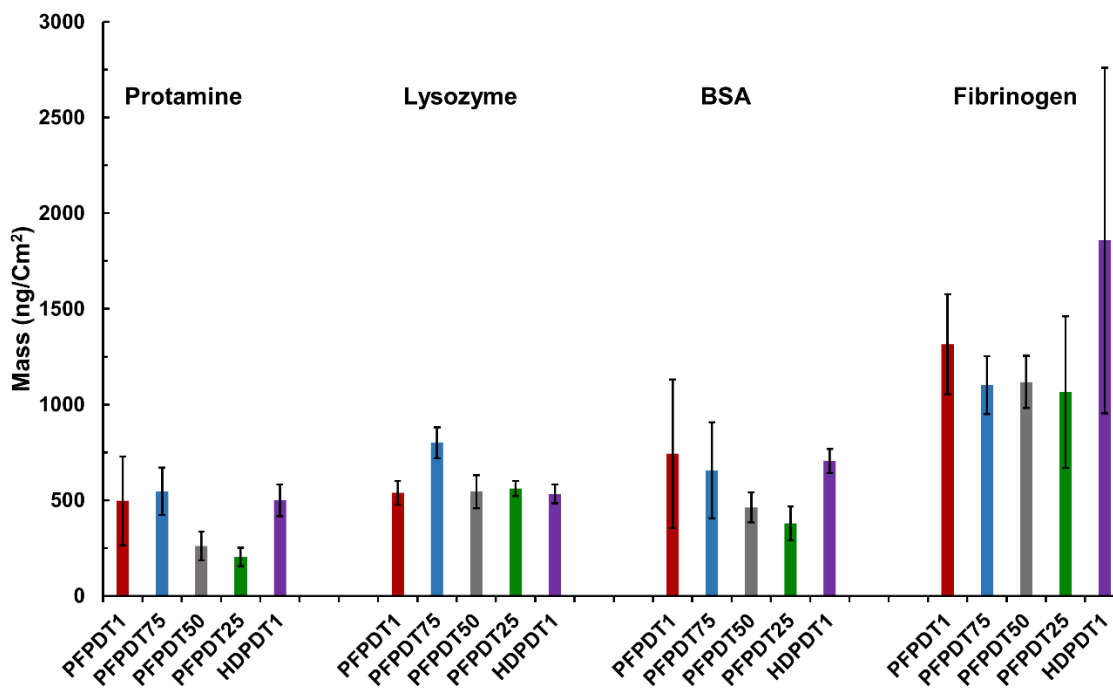


**Figure 4.5.** Calculated mass loading values determined by QCM for the mixed SAMs, **PFPDT1**, **PFPDT75**, **PFPDT50**, **PFPDT25**, and **HDPDT1**, after exposure to 1 mg/mL of protein in PBS solution for 1 h.

After protein exposure, both protamine and BSA show similar trends. For the protamine, the mass increases to 497 ng/cm<sup>2</sup>, 546 ng/cm<sup>2</sup>, 261 ng/cm<sup>2</sup>, 203 ng/cm<sup>2</sup> and 500 ng/cm<sup>2</sup> for **PFPDT1**, **PFPDT75**, **PFPDT50**, **PFPDT25**, and **HDPDT1**, respectively. With the BSA, the mass increases to 743 ng/cm<sup>2</sup>, 656 ng/cm<sup>2</sup>, 462 ng/cm<sup>2</sup>, 379 ng/cm<sup>2</sup>, and 706 ng/cm<sup>2</sup> for **PFPDT1**, **PFPDT75**, **PFPDT50**, **PFPDT25**, and **HDPDT1**,

respectively. The trend denoted that **PF PDT1**, **PF PDT75**, and **HDPDT1** behave similarly, but there is a decrease in mass on the **PF PDT50** and an even greater mass on the **PF PDT25** surface. When considering the size of the proteins, an increase in mass is expected in the overall trend when comparing protamine, a molecular weight protein of 4 KDa, to BSA, a protein with a molecular weight of 55 KDa. Likewise, fibrinogen shows an increase of 1315 ng/cm<sup>2</sup>, 1102 ng/cm<sup>2</sup>, 1118 ng/cm<sup>2</sup>, 1065 ng/cm<sup>2</sup>, and 1857 ng/cm<sup>2</sup> for **PF PDT1**, **PF PDT75**, **PF PDT50**, **PF PDT25**, and **HDPDT1**, respectively.

**Table 4.5.** QCM Mass Loading Values after Exposure to Protein Solutions

<b>Adsorbate</b>	<b>Protamine Mass ng/cm<sup>2</sup></b>	<b>Lysozyme Mass ng/cm<sup>2</sup></b>	<b>BSA Mass ng/cm<sup>2</sup></b>	<b>Fibrinogen Mass ng/cm<sup>2</sup></b>
<b>PF PDT1</b>	497 ± 232	539 ± 62	743 ± 387	1315 ± 261
<b>PF PDT75</b>	546 ± 124	800 ± 81	656 ± 251	1102 ± 151
<b>PF PDT50</b>	261 ± 75	545 ± 86	462 ± 78	1118 ± 136
<b>PF PDT25</b>	203 ± 48	561 ± 39	379 ± 88	1065 ± 396
<b>HDPDT1</b>	500 ± 83	534 ± 49	706 ± 63	1857 ± 750

SAM surfaces were exposed for 1 h to 1 mg/mL of protein in PBS solution.

Fibrinogen is a large neutral protein;<sup>41</sup> therefore, a greater deviations are noted are values fall within the large error bars and no distinctions can be determined between the adsorbates. An exception to the trend and the noticeable increase of adsorption of protein on the substrate is noticed with the interaction of lysozyme, a charged protein.<sup>42</sup> The increase in mass after exposure to lysozyme was 539 ng/cm<sup>2</sup>, 800 ng/cm<sup>2</sup>, 545 ng/cm<sup>2</sup>, 561 ng/cm<sup>2</sup>, and 534 ng/cm<sup>2</sup> for **PF PDT1**, **PF PDT75**, **PF PDT50**, **PF PDT25**, and

**HDPDT1**, respectively. The **PF PDT75** surface exhibited more interactions resulting in a greater amount of mass adhered to the surface when compared to the other adsorbates. The mixed adsorbates show an overall trend of lower mass loading, with the exception of a charged protein surface, which is likely due to increased hydrophobic patches on the surface of the protein that generates greater attraction to the hydrophobic component of the mixture. However, the introduction of the **HDPDT1** in the mixture generated a conformational order that likely allows for maximized van der Waals interactions within the adsorbates on the surface generating less favorable surface interactions; therefore, it ultimately has less adhesion of protein on the SAM surface.<sup>5,46-49</sup>

#### **4.3.2.2. Ellipsometric Thickness Measurements of Protein Adhesion**

Ellipsometric measurements were taken on all surface with no distinguishable differences in surfaces; note, the results reported here are for the evaporated gold substrates. The numerical values of the changes in thickness after exposure to protein are found in Table 4.6, and are graphically represented in Figure 4.6. The changes in ellipsometric thickness values may provide information relating to the amount of material adhered to the surface after protein exposure. Ellipsometric thickness measurements increase as the molecular mass of the proteins increase, with the exception of lysozyme, which is similar in values to BSA, indicative of greater surface interactions between the protein and the surface. The adhesion of the protein to the surface can generate surfaces with greater roughness. Increased surface roughness generates greater scatter, producing larger errors, and is confirmed with AFM measurements (*vide infra*) of the surface. Ellipsometric measurements show similar performance of protein resistance for the mixed SAMs, with the exception of protamine (the smallest protein). The change in thickness

values for protamine were  $1 \pm 1$ ,  $4 \pm 2$ ,  $2 \pm 1$ ,  $10 \pm 1$ , and  $9 \pm 3$  Å for **PF PDT1**, **PF PDT75**, **PF PDT50**, **PF PDT25**, and **HDPDT1**, respectively. The interactions of protamine show similar increased performance for **PF PDT1**, **PF PDT75**, and **PF PDT50** when compared to **PF PDT25** and **HDPDT1**, which have similar performance.

For the surfaces exposed to BSA, the protein adhesion appears to be similar for all of the SAM surfaces,  $16 \pm 3$ ,  $18 \pm 2$ ,  $15 \pm 3$ ,  $19 \pm 1$ , and  $20 \pm 4$  Å for **PF PDT1**, **PF PDT75**, **PF PDT50**, **PF PDT25**, and **HDPDT1**, respectively. Likewise, exposure to fibrinogen led to increased thicknesses likely due to the larger size of the protein and was  $31 \pm 7$ ,  $38 \pm 9$ ,  $40 \pm 10$ ,  $39 \pm 11$ , and  $43 \pm 8$  Å for **PF PDT1**, **PF PDT75**, **PF PDT50**, **PF PDT25**, and **HDPDT1**, respectively. However, the thickness values for all of the SAMs remained within their standard deviation. For lysozyme, the thickness values fall within the standard deviation for all of the SAM surfaces, which were  $19 \pm 1$ ,  $18 \pm 1$ ,  $23 \pm 1$ ,  $21 \pm 1$ , and  $18 \pm 2$  Å for **PF PDT1**, **PF PDT75**, **PF PDT50**, **PF PDT25**, and **HDPDT1**, respectively. However, the thickness values for lysozyme, a 14 KDa molecular weight protein, were similar to or greater than BSA, a 55 KDa molecular weight protein. This correlates to the increased mass loading trend observed with the QCM data, and is likely due to the interaction of the charged protein with the substrates. Thickness measurements alone do not indicate one surface has greater improvement over others, but the values tend to indicate that surface charge may play a vital role in protein adhesion. Additional analysis of the surfaces with AFM (*vide infra*) indicate variations in surface roughness which can impact ellipsometric measurements due to increased scattering from the surface roughness.

**Table 4.6.** Change in Ellipsometric Thickness Values for the Mixed SAMs after Exposure to Protein Solutions

$\Delta$ Thickness (Å)	Protamine	Lysozyme	BSA	Fibrinogen
<b>PFPDT 1</b>	1 ± 0.5	19 ± 1.3	16 ± 2.6	31 ± 7.3
<b>PFPDT75</b>	4 ± 2.2	18 ± 0.8	18 ± 1.5	38 ± 9.3
<b>PFPDT50</b>	2 ± 0.4	23 ± 1.0	15 ± 3.3	40 ± 9.8
<b>PFPDT25</b>	10 ± 0.9	21 ± 1.13	19 ± 1.0	39 ± 11.1
<b>HDPDT 1</b>	9 ± 3.2	18 ± 2.0	20 ± 3.9	43 ± 7.9

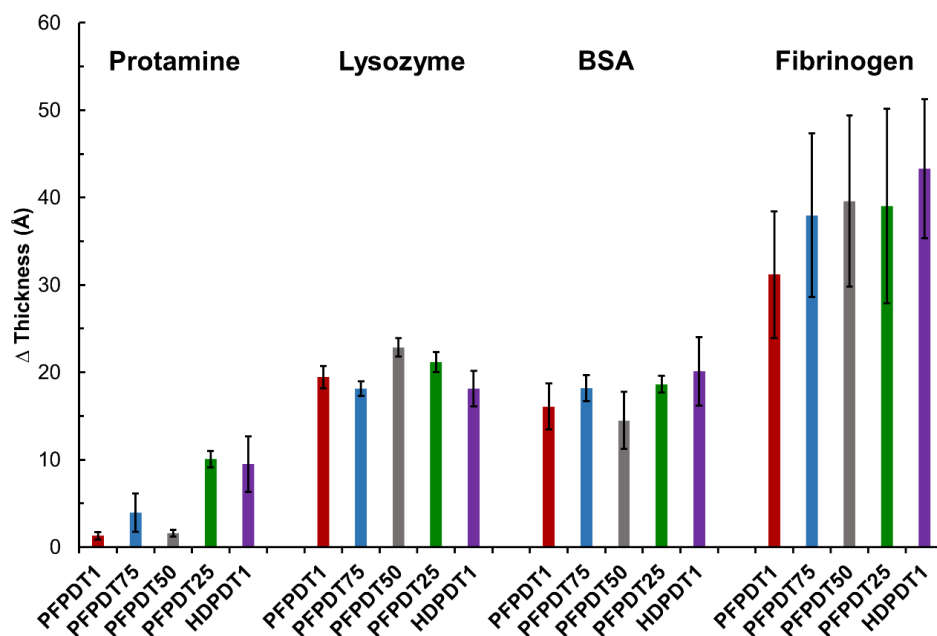


**Figure 4.6.** Graphical representation of the changes in film thickness of the mixed SAMs derived from the bidentate alkanethiols (**PFPDT** and **HDPDT**) after exposure to protein solutions.

#### 4.3.2.3. Evaluation of Surface Topography by AFM

Since AFM is widely used to determine the surface topography of surfaces after interaction with biological materials, distinctions in surface patterning after exposure to the protein solutions was evaluated using AFM.<sup>50-56</sup> The surface topography imaging of the

SAMs after exposure to the proteins are shown in Figure 4.7 for protamine, Figure 4.8 for lysozyme, Figure 4.9 for BSA, and Figure 4.10 for fibrinogen. Each figure contains both a  $5\ \mu\text{m} \times 5\ \mu\text{m}$  and a  $1\ \mu\text{m} \times 1\ \mu\text{m}$  image of each adsorbate after exposure to the protein. Patterning displayed in AFM images indicate differences in surface topography, which may indicate distinctions among the adsorbates from this displayed pattern.<sup>52,55,57,58</sup>

For example, Figure 4.7, shows an image with a few bright spots on the **PFPDT1** surface (Figure 4.7F) and more spots on the **PFPDT75** surface (Figure 4.7G) surface. The **PFPDT50** surface (Figure 4.7H) exhibited spherical-like globule pattern, **PFPDT25** (Figure 4.7I) exhibited a network like structure, and **HDPDT1** (Figure 4.7J) exhibited a network with globules present in the image. As the larger proteins adhere to the surface, the network patterning became more visible, as seen in Figure 4.8F, Figure 4.9F, and Figure 4.10F, which shows an increasing network pattern for **PFPDT1** exposed to lysozyme, BSA, and fibrinogen, respectively. Additional statistical evaluation of surface topography may provide quantitative measurements that may yield insight into surface interactions at the protein surface interface and help to correlate the topography to the amount of material present on the surface.

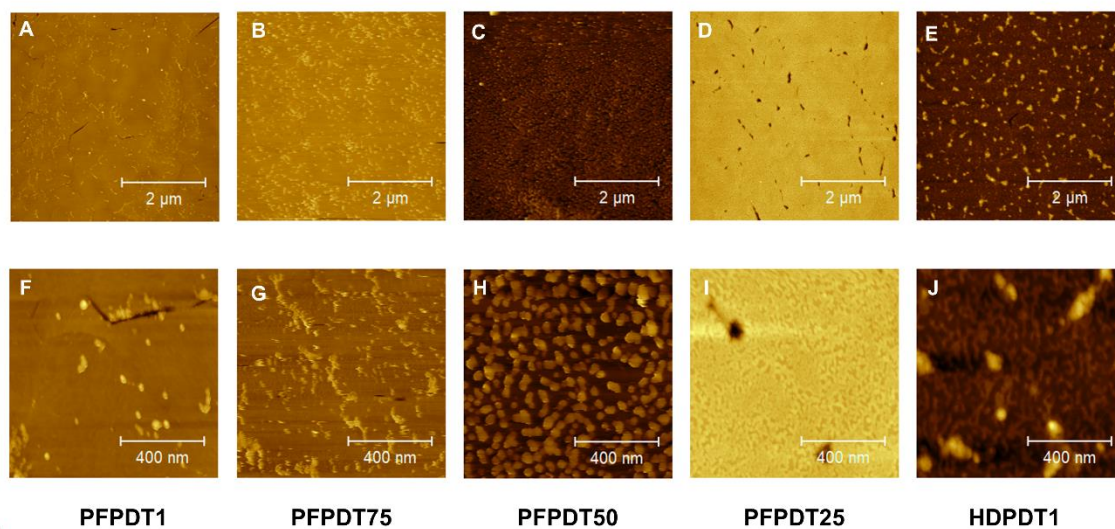


**Figure 4.7.** Topography after exposure to protamine for (A, F) **PFPDT1**, (B, G) **PFPDT75**, (C, H) **PFPDT50**, (D, I) **PFPDT25** and (E, J) **HDPDT1** at  $5\ \mu\text{m} \times 5\ \mu\text{m}$  (top) and  $1\ \mu\text{m} \times 1\ \mu\text{m}$  (bottom).

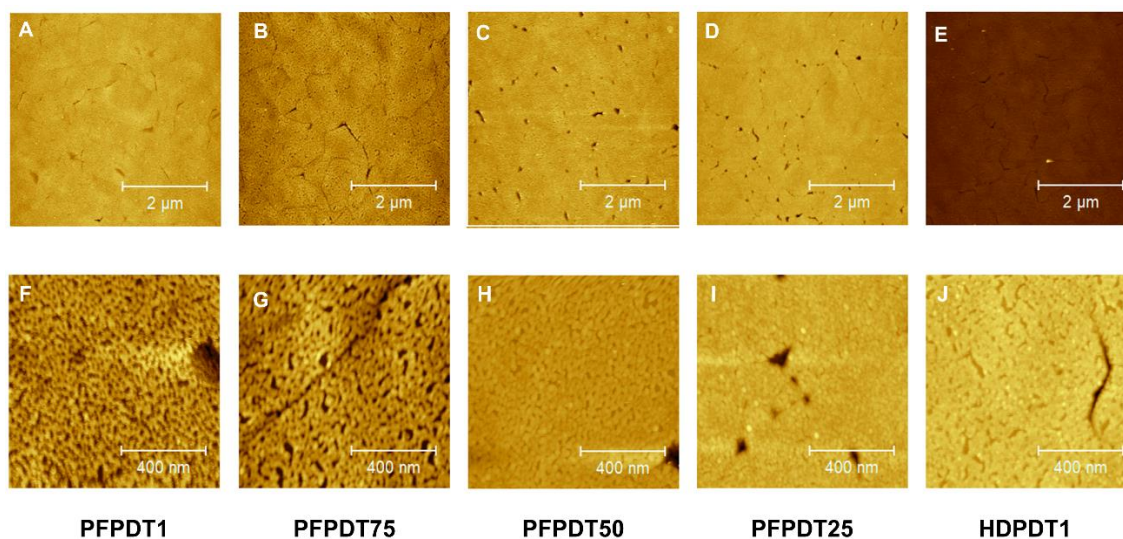


**Figure 4.8.** Topography after exposure to lysozyme for (A, F) **PFPDT1**, (B, G) **PFPDT75**, (C, H) **PFPDT50**, (D, I) **PFPDT25** and (E, J) **HDPDT1** at  $5\ \mu\text{m} \times 5\ \mu\text{m}$  (top) and  $1\ \mu\text{m} \times 1\ \mu\text{m}$  (bottom).

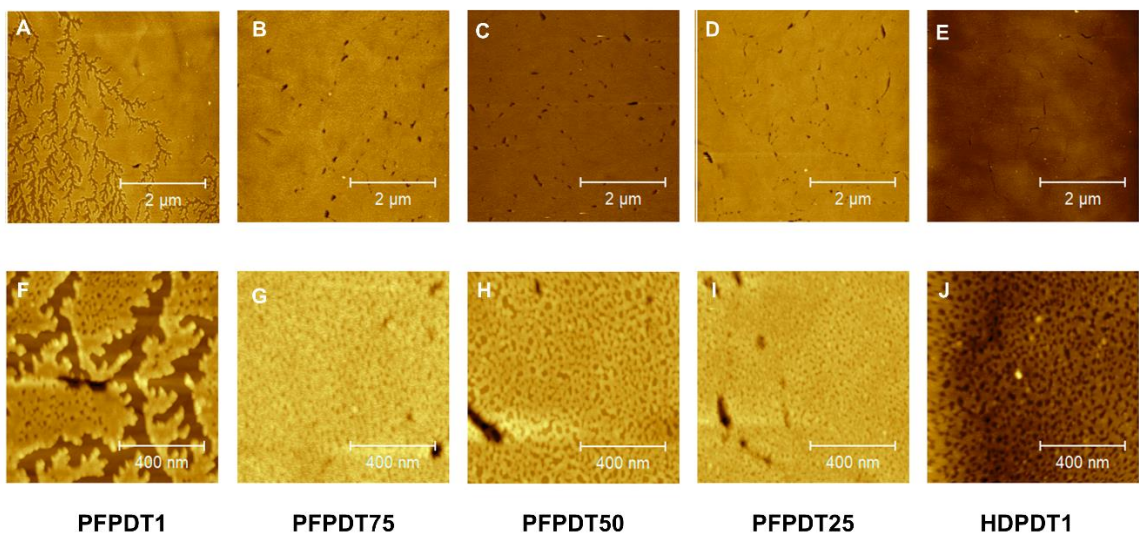


**Figure 4.9.** Topography after exposure to BSA for (A, F) **PFPDT1**, (B, G) **PFPDT75**, (C, H) **PFPDT50**, (D, I) **PFPDT25** and (E, J) **HDPDT1** at  $5\ \mu\text{m} \times 5\ \mu\text{m}$  (top) and  $1\ \mu\text{m} \times 1\ \mu\text{m}$  (bottom).

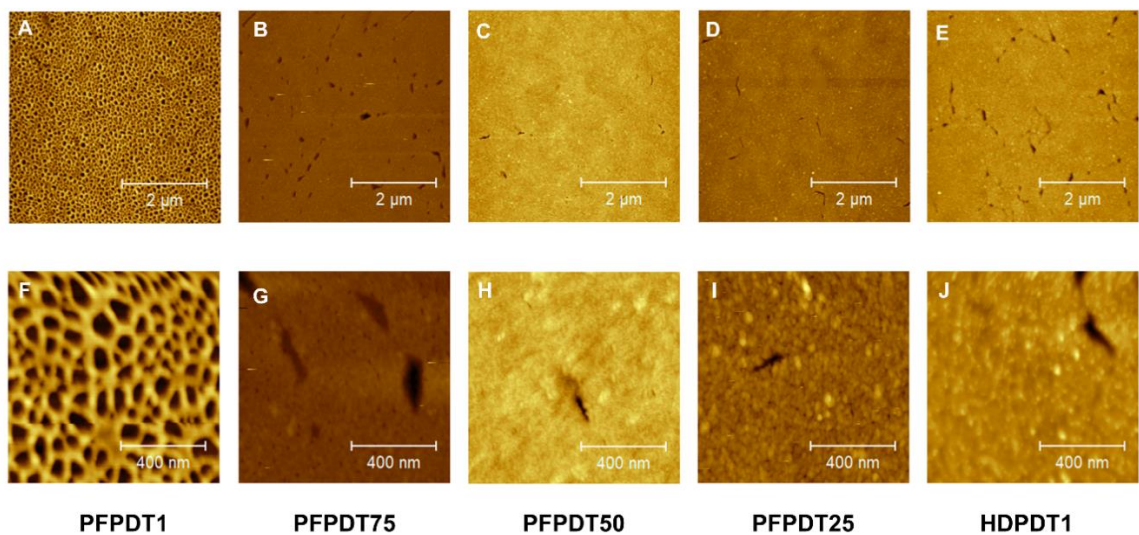


**Figure 4.10.** Topography after exposure to fibrinogen for (A, F) **PFPDT1**, (B, G) **PFPDT75**, (C, H) **PFPDT50**, (D, I) **PFPDT25** and (E, J) **HDPDT1** at  $5\ \mu\text{m} \times 5\ \mu\text{m}$  (top) and  $1\ \mu\text{m} \times 1\ \mu\text{m}$  (bottom).

To determine surface roughness, the arithmetic average ( $R_a$ ) and the root mean square ( $R_{ms}$ ) are commonly used. Both  $R_a$  and  $R_{ms}$  values (see Table 4.7 and Table 4.8,

respectively) were determined using Gwyddion and are graphically displayed in Figure 4.11. Surface roughness measurements account for the peak heights and valleys across the imaged area. The measurements supply information regarding the heights in the pattern and are likely to increase with more material and/or larger proteins attached to the surface. Surface roughness measurements are an average of the peaks and valleys of the entire imaged area, so it is possible that multiple surfaces with different patterns can have the same numerical values. For example, **PFPDT1** after exposure to protamine (Figure 4.7F) has an  $R_a$  value of 0.65 nm and **HDPDT1** after exposure to lysozyme (Figure 4.8J) has a  $R_a$  value of 0.69 nm, yet they have very different patterns on the surfaces. With Rms calculations, both **PFPDT1**, after exposure to protamine, and **PFPDT25**, after exposure to lysozyme, have the same Rms values of 1.14 nm, but they maintain different patterns on the surface as well.

Surface roughness measurements alone, do not clearly correlate the roughness of a surface to the material adhered to the surface. For example, protamine should have the least amount of material on the surface, but it contains some of the highest roughness measurements across the series. This is likely due to the high heights where the adhesion took place compared to the low valleys with little protein. Comparing the values in fibrinogen, the expectation would be high roughness values, yet the surfaces that adhered the most protein have low roughness measurements which are likely due to the high surface coverage of the protein on the surface of the adsorbate. This results in the peaks and valleys being closer together, which ultimately translates to lower roughness values. Evaluation

of the height density distribution may provide the interpretation and clarification of the  $R_a$  and Rms values to relate surface topography to the amount of material on the surface.

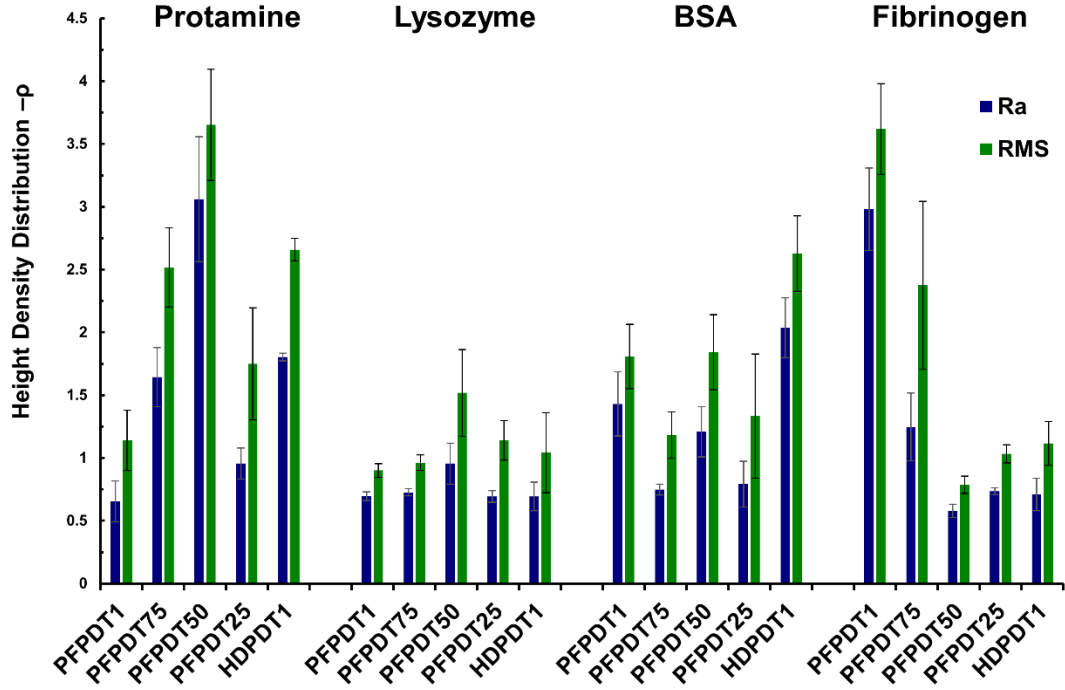


**Figure 4.11.** Comparison of average roughness ( $R_a$ ) and root mean square (Rms) values for each of the mixed SAM surfaces (PFPDT1, PFPDT75, PFPDT50, PFPDT25, and HDPDT1) after exposure to protamine, lysozyme, BSA, and fibrinogen, respectively.

**Table 4.7.** Calculated  $R_a$  Values for the Mixed SAMs

Protein	$R_a$ (nm)				
	PFPDT1	PFPDT75	PFPDT50	PFPDT25	HDPDT1
Protamine	$0.65 \pm 0.16$	$1.64 \pm 0.24$	$3.06 \pm 0.50$	$0.96 \pm 0.12$	$1.80 \pm 0.03$
Lysozyme	$0.70 \pm 0.04$	$0.73 \pm 0.03$	$0.95 \pm 0.16$	$0.69 \pm 0.05$	$0.69 \pm 0.11$
BSA	$1.43 \pm 0.26$	$0.75 \pm 0.04$	$1.21 \pm 0.20$	$0.79 \pm 0.18$	$2.04 \pm 0.24$
Fibrinogen	$2.98 \pm 0.33$	$1.25 \pm 0.27$	$0.58 \pm 0.05$	$0.73 \pm 0.03$	$0.71 \pm 0.13$

**Table 4.8.** Calculated Rms Values for the Mixed SAMs

Protein	Rms (nm)				
	PF PDT1	PF PDT75	PF PDT50	PF PDT25	HDPDT1
Protamine	1.14 ± 0.23	2.52 ± 0.31	3.65 ± 0.44	1.75 ± 0.45	2.66 ± 0.09
Lysozyme	0.90 ± 0.05	0.96 ± 0.06	1.52 ± 0.35	1.14 ± 0.16	1.04 ± 0.32
BSA	1.81 ± 0.25	1.18 ± 0.18	1.84 ± 0.30	1.33 ± 0.49	2.63 ± 0.30
Fibrinogen	3.62 ± 0.36	2.37 ± 0.67	0.79 ± 0.07	1.03 ± 0.07	1.12 ± 0.17

The height density distributions for the mixed ratio adsorbates with each protein are found in Figure 4.12. For protamine, the height density distribution found in Figure 4.12A, **HDPDT1** exhibits a broad peak, with a maximum height of ~26 nm with peaks ranging past 40 nm in height. **PF PDT25** has the second highest peak values, ~ 23 nm, with a narrow peak, which would correlate to lower surface roughness values. **PF PDT1** also has a narrow peak with a higher density at ~ 17 nm. However, **PF PDT75** and **PF PDT50** have broad peaks with maximum values of ~ 18 nm and 12 nm, respectively, but **PF PDT50** has lower surface density. For the protein lysozyme, Figure 4.12B shows that the surfaces all have tall narrow peaks with similar heights -- ~15 nm, ~19 nm, ~19 nm, and ~17 nm for **PF PDT1**, **PF PDT75**, **PF PDT50**, and **HDPDT1**, respectively -- except for the **PF PDT75** surface, which has a similar peak height at ~18 nm with a wider peak, which results in the higher surface roughness.

The aforementioned distributions are likely the cause for the similar roughness measurements observed. For BSA (Figure 4.12C), the **HDPDT1** adsorbate has the

broadest peak, with a height of ~20 nm, followed by **PF PDT1**, which has a lower peak height (~15 nm). The **PF PDT75** adsorbate has a narrower peak with greater surface coverage, but it has the same peak height as **PF PDT1** at ~ 15 nm. The **PF PDT50** and **PF PDT25** surfaces have similar peak shapes, but **PF PDT50** is slightly broader and has a peak height of ~ 24 nm, compared to **PF PDT25** which has a peak height at ~20 nm, with a higher surface coverage. The height density plot for fibrinogen, found in Figure 4.12D, shows that **HDPDT1**, **PF PDT25**, and **PF PDT50** all have similar peak shape, which indicate similar surface roughness measurements, but the peak heights are at ~20 nm, ~18 nm, and ~14 nm, respectively. The **PF PDT1** and **PF PDT75** have narrower peaks, but **PF PDT1** has a peak maximum at ~11 nm and higher surface coverage compared to **PF PDT75**, which has a peak max at ~8 nm and lower surface coverage.

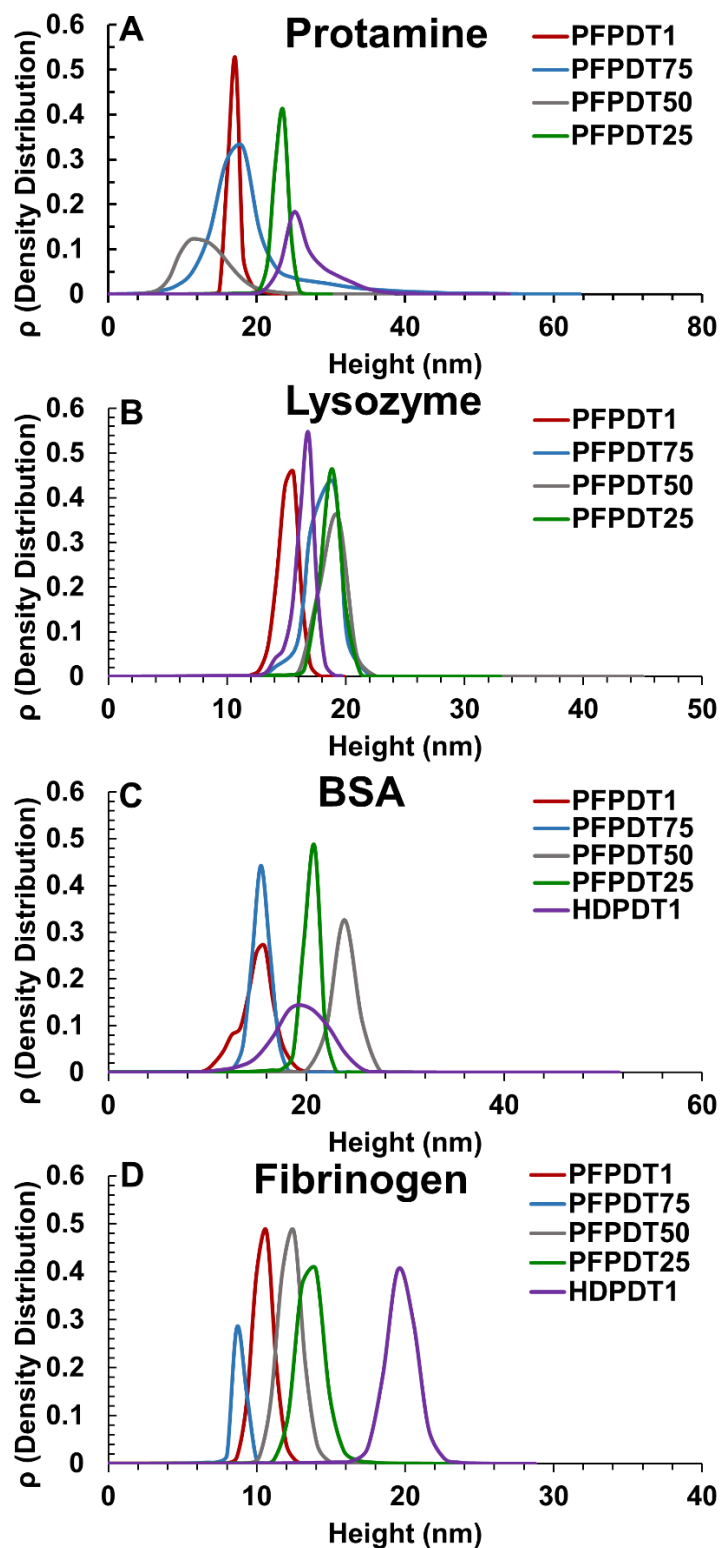


**Figure 4.12.** Height distribution density plots determined from AFM images of the PFPDT1, PFPDT75, PFPDT50, PFPDT25, and HDPDT1 SAMs after exposure to (A) protamine, (B) lysozyme, (C) BSA, and (D) fibrinogen.

The AFM images display surface topographies with various patterns and surface roughness measurements that are able to provide insight into protein adhesion by analyzing height distribution density plots for the mixed SAMs after exposure to the protein solutions. Surface roughness variances can be explained by evaluation of height density plots; also, the increase in surface roughness as observed with protamine is indicative of greater scatter from the ellipsometry measurements; thus, scattering accounts for the greater errors observed. Analysis of the surface patterns correlates with the QCM data and the ellipsometry data. It confirms that the mixed SAMs **PF PDT75**, **PF PDT50**, and **PF PDT25** have slightly improved protein resistant properties when compared to **HDPDT1** and **PF PDT1**. It is likely due to the conformational order observed in the mixed SAM ratios, and the ability to maximize van der Waals forces to generate less favorable interactions between the adsorbates and the proteins.<sup>5</sup> However, the results also indicate that the charge on the surface of the protein plays a vital role in the anti-adhesive properties of the films as well. This is clearly seen for lysozyme, which exhibited similar roughness measurements and density distributions on all of the analyzed surfaces. Moreover, these observations correlate with the mass loading data and the thickness values, which fall within their standard deviations.

#### **4.4. Conclusions**

Binary SAMs generated from various ratios of **HDPDT** and **PF PDT** in the development solutions, along with the single component SAMs were characterized with ellipsometry, XPS, and QCM, which confirmed bidentate adsorbates readily formed mixed monolayers with composition ratios that closely align with the ratios of the development solutions. The performance of the mixed SAMs was compared to the single component

SAMs to evaluate the impact of the mixed composition on protein resistance. Ellipsometry data shows changes in thickness after protein exposure for all adsorbates, which fall within the standard deviation, with large error values arising from additional scattering, confirmed by AFM surface roughness measurements. AFM imaging revealed different patterns on the surface of the SAMs, indicating that surface topographies can help to distinguish protein patterns on the surface.

The most revealing data was found with QCM, which shows increased performance in protein resistance as the alkyl component was increased, where **PPPDT75** < **PPPDT50** < **PPPDT25**, which is likely due to the conformational order found in the mixed SAMs that allows for maximized van der Waals interactions. However, the QCM data for the proteins with charged surfaces indicated similar mass loading for all of the surfaces, revealing the impact of charged proteins on adhesion to the SAMs. Overall, multiple analytical techniques confirm the formation of the mixed SAMs, and provided a means to analyze protein interactions. Specifically, ellipsometry, QCM, and AFM show a reliable method to investigate the interactions between SAMs and various proteins to understand how the adsorbate structure influences protein resistance, in addition to how various protein properties affect adhesion to the adsorbate surface.

#### 4.5. References

- (1) Sun, T.; Wang, G.; Liu, H.; Feng, L.; Jiang, L.; Zhu, D. Control over the Wettability of an Aligned Carbon Nanotube Film. *J. Am. Chem. Soc.* **2003**, *125*, 14996–14997.
- (2) Zheng, Z.; Azzaroni, O.; Zhou, F.; Huck, W. T. S. Topography Printing to Locally Control Wettability. *J. Am. Chem. Soc.* **2006**, *128*, 7730–7731.

- (3) Kawai, T.; Suzuki, M.; Kondo, T. Fabrication of Flexible Gold Films with Periodic Sub-Micrometer Roughness and Their Wettability Control by Modification of SAM. *Langmuir* **2006**, *22*, 9957–9961.
- (4) Fukuzawa, K.; Deguchi, T.; Yamawaki, Y.; Itoh, S.; Muramatsu, T.; Zhang, H. Control of Wettability of Molecularly Thin Liquid Films by Nanostructures. *Langmuir* **2008**, *24*, 2921–2928.
- (5) Lee, H. J.; Jamison, A. C.; Lee, T. R. Two Are Better than One: Bidentate Adsorbates Offer Precise Control of Interfacial Composition and Properties. *Chem. Mater.* **2016**, *28* (15), 5356–5364.
- (6) Lee, M.; Kwak, G.; Yong, K. Wettability Control of ZnO Nanoparticles for Universal Applications. *ACS Appl. Mater. Interfaces* **2011**, *3*, 3350–3356.
- (7) Lee, M. W.; An, S.; Joshi, B.; Lathe, S. S.; Yoon, S. S. Highly Efficient Wettability Control via Three-Dimensional (3D) Suspension of Titania Nanoparticles in Polystyrene Nanofibers. *ACS Appl. Mater. Interfaces* **2013**, *5*, 1232–1239.
- (8) Pakdel, A.; Bando, Y.; Golberg, D. Plasma-Assisted Interface Engineering of Boron Nitride Nanostructure Films. *ACS Nano* **2014**, *8*, 10631–10639.
- (9) Linhui, L.; Yang, Z.; Bo, L.; Changyou, G. Fabrication of Thermoresponsive Polymer Gradients for Study of Cell Adhesion and Detachment. *Langmuir* **2008**, *24*, 13632–13639.
- (10) Pei, Y.; Travas-Sejdic, J.; Williams, D. E. Reversible Electrochemical Switching

- of Polymer Brushes Grafted onto Conducting Polymer Films. *Langmuir* **2012**, *28*, 8072–8083.
- (11) Nguyen, P. Q. M.; Yeo, L. P.; Lok, B. K.; Lam, Y. C. Patterned Surface with Controllable Wettability for Inkjet Printing of Flexible Printed Electronics. *ACS Appl. Mater. Interfaces* **2014**, *6*, 4011–4016.
- (12) Lahann, J.; Mitragotri, S.; Tran, T. N.; Kaido, H.; Sundaram, J.; Choi, I. S.; Hoffer, S.; Somorjai, G. A.; Langer, R. A Reversibly Switching Surface. *Science* (80-. ). **2003**, *299*, 371–374.
- (13) Pei, Y.; Ma, J. Electric Field Induced Switching Behaviors of Monolayer-Modified Silicon Surfaces: Surface Designs and Molecular Dynamics Simulations. *J. Am. Chem. Soc.* **2005**, *127*, 6802–6813.
- (14) Chen, K. Y.; Ivashenko, O.; Carroll, G. T.; Robertus, J.; Kistemaker, J. C. M.; London, G.; Browne, W. R.; Rudolf, P.; Feringa, B. L. Control of Surface Wettability Using Tripodal Light-Activated Molecular Motors. *J. Am. Chem. Soc.* **2014**, *136*, 3219–3224.
- (15) Kwak, G.; Lee, M.; Senthil, K.; Yong, K. Wettability Control and Water Droplet Dynamics on SiC-SiO<sub>2</sub> Core-Shell Nanowires. *Langmuir* **2010**, *26*, 12273–12277.
- (16) Chi, Y. S.; Lee, J. K.; Lee, S.; Choi, I. S. Control of Wettability by Anion Exchange on Si/SiO<sub>2</sub> Surfaces. *Langmuir* **2007**, *20*, 3024–3027.
- (17) Portilla, L.; Halik, M. Smoothly Tunable Surface Properties of Aluminum Oxide

- Core-Shell Nanoparticles by a Mixed-Ligand Approach. *ACS Appl. Mater. Interfaces* **2014**, *6*, 5977–5982.
- (18) Christopher Love, J.; Wolfe, D. B.; Haasch, R.; Chabynyc, M. L.; Paul, K. E.; Whitesides, G. M.; Nuzzo, R. G. Formation and Structure of Self-Assembled Monolayers of Alkanethiolates on Palladium. *J. Am. Chem. Soc.* **2003**, *125*, 2597–2609.
- (19) Love, J. C.; Estroff, L. A.; Kriebel, J. K.; Nuzzo, R. G.; Whitesides, G. M. Self-Assembled Monolayers of Thiolates on Metals as a Form of Nanotechnology. *Chem. Rev.* **2005**, *105*, 1103–1170.
- (20) Vericat, C.; Vela, M. E.; Benitez, G.; Carro, P.; Salvarezza, R. C. Self-Assembled Monolayers of Thiols and Dithiols on Gold: New Challenges for a Well-Known System. *Chem. Soc. Rev.* **2010**, *39*, 1805–1834.
- (21) Bain, C. D.; Whitesides, G. M. Molecular-Level Control over Surface Order in Self-Assembled Monolayer Films of Thiols on Gold. *Science (80-. )*. **1988**, *240*, 62–63.
- (22) Bain, C. D.; Whitesides, G. M. Formation of Monolayers by the Coadsorption of Thiols on Gold: Variation in the Length of the Alkyl Chain. *J. Am. Chem. Soc.* **1989**, *111*, 7164–7175.
- (23) Bain, C. D.; Evall, J.; Whitesides, G. M. Formation of Monolayers by the Coadsorption of Thiols on Gold: Variation in the Head Group, Tail Group, and

Solvent. *J. Am. Chem. Soc.* **1989**, *111*, 7155–7164.

- (24) Folkers, J. P.; Laibinis, P. E.; Whitesides, G. M.; Deutch, J. Phase Behavior of Two-Component Self-Assembled Monolayers of Alkanethiolates on Gold. *J. Phys. Chem.* **1994**, *98*, 563–571.
- (25) Stranick, S. J.; Parikh, A. N.; Tao, Y. T.; Allara, D. L.; Weiss, P. S. Phase Separation of Mixed-Composition Self-Assembled Monolayers into Nanometer Scale Molecular Domains. *J. Phys. Chem.* **1994**, *98*, 7636–7646.
- (26) Smith, R. K.; Reed, S. M.; Lewis, P. A.; Monnell, J. D.; Clegg, R. S.; Kelly, K. F.; Bumm, L. A.; Hutchison, J. E.; Weiss, P. S. Phase Separation within a Binary Self-Assembled Monolayer on Au{111} Driven by an Amide-Containing Alkanethiol. *J. Phys. Chem. B* **2001**, *105*, 1119–1122.
- (27) Folkers, J. P.; Laibinis, P. E.; Whitesides, G. M. Self-Assembled Monolayers of Alkanethiols on Gold: Comparisons of Monolayers Containing Mixtures of Short- and Long-Chain Constituents with CH<sub>3</sub> and CH<sub>2</sub>OH Terminal Groups. *Langmuir* **1992**, *8*, 1330–1341.
- (28) Shevade, A. V.; Zhou, J.; Zin, M. T.; Jiang, S. Phase Behavior of Mixed Self-Assembled Monolayers of Alkanethiols on Au(111): A Configurational-Bias Monte Carlo Simulation Study. *Langmuir* **2001**, *17*, 7566–7572.
- (29) Schönherr, H.; Ringsdorf, H. Self-Assembled Monolayers of Symmetrical and Mixed Alkyl Fluoroalkyl Disulfides on Gold. 1. Synthesis of Disulfides and

- Investigation of Monolayer Properties. *Langmuir* **2002**, *12*, 3891–3897.
- (30) Schönherr, H.; Ringsdorf, H.; Jaschke, M.; Butt, H.-J.; Bamberg, E.; Allinson, H.; Evans, S. D. Self-Assembled Monolayers of Symmetrical and Mixed Alkyl Fluoroalkyl Disulfides on Gold. 2. Investigation of Thermal Stability and Phase Separation. *Langmuir* **2002**, *12*, 3898–3904.
- (31) Chinwangso, P.; Jamison, A. C.; Lee, T. R. Multidentate Adsorbates for Self-Assembled Monolayer Films. *Acc. Chem. Res.* **2011**, *44*, 511–519.
- (32) Lee, H. J.; Jamison, A. C.; Yuan, Y.; Li, C. H.; Rittikulsittichai, S.; Rusakova, I.; Lee, T. R. Robust Carboxylic Acid-Terminated Organic Thin Films and Nanoparticle Protectants Generated from Bidentate Alkanethiols. *Langmuir* **2013**, *29*, 10432–10439.
- (33) Lee, H. J.; Jamison, A. C.; Lee, T. R. Boc-Protected  $\omega$ -Amino Alkanedithiols Provide Chemically and Thermally Stable Amine-Terminated Monolayers on Gold. *Langmuir* **2015**, *31*, 2136–2146.
- (34) Buttry, D. A.; Ward, M. D. Measurement of Interfacial Processes at Electrode Surfaces with the Electrochemical Quartz Crystal Microbalance. *Chem. Rev.* **1992**, *92*, 1355–1379.
- (35) Sauerbrey, G. Verwendung von Schwingquarzen Zur Wägung Dünner Schichten Und Zur Mikrowägung. *Zeitschrift für Phys.* **1959**, *155*, 206–222.
- (36) Gamry Instruments. Basics of a Quartz Crystal Microbalance. *Spectrum* **2012**, *1*,

1–7.

- (37) Atre, S. V.; Liedberg, B.; Allara, D. L. Chain Length Dependence of the Structure and Wetting Properties in Binary Composition Monolayers of OH- and CH<sub>3</sub>-Terminated Alkanethiolates on Gold. *Langmuir* **1995**, *11*, 3882–3893.
- (38) Venkataraman, N. V.; Stefan Zürcher; Rossi, A.; Lee, S.; Naujoks, N.; Spencer, N. D. Spatial Tuning of the Metal Work Function by Means of Alkanethiol and Fluorinated Alkanethiol Gradients. *J. Phys. Chem. C* **2009**, *113*, 5620–5628.
- (39) Ballav, N.; Terfort, A.; Zharnikov, M. Mixing of Nonsubstituted and Partly Fluorinated Alkanethiols in a Binary Self-Assembled Monolayer. *J. Phys. Chem. C* **2009**, *113*, 3697–3706.
- (40) Tsai, D. H.; Delrio, F. W.; Keene, A. M.; Tyner, K. M.; MacCuspie, R. I.; Cho, T. J.; Zachariah, M. R.; Hackley, V. A. Adsorption and Conformation of Serum Albumin Protein on Gold Nanoparticles Investigated Using Dimensional Measurements and in Situ Spectroscopic Methods. *Langmuir* **2011**, *27*, 2464–2477.
- (41) Bachmann, L.; Schmitt-Fumain, W. W.; Hammel, R.; Lederer, K. Size and Shape of Fibrinogen, 1. Electron Microscopy of the Hydrated Molecule. *Die Makromol. Chemie* **1975**, *176*, 2603–2618.
- (42) Colvin, J. R. The Size and Shape of Lysozyme. *Can. J. Chem.* **1952**, *30*, 831–834.
- (43) Bolan, C. D.; Klein, H. G. Blood Component and Pharmacologic Therapy for Hemostatic Disorders. In *Consultative Hemostasis and Thrombosis: Third Edition*;

Saunders: Philadelphia, 2013.

- (44) Marucco, A.; Catalano, F.; Fenoglio, I.; Turci, F.; Martra, G.; Fubini, B. Possible Chemical Source of Discrepancy between in Vitro and in Vivo Tests in Nanotoxicology Caused by Strong Adsorption of Buffer Components. *Chem. Res. Toxicol.* **2015**, *28*, 87–91.
- (45) Parkes, M.; Myant, C.; Cann, P. M.; Wong, J. S. S. The Effect of Buffer Solution Choice on Protein Adsorption and Lubrication. *Tribol. Int.* **2014**, *72*, 108–117.
- (46) Porter, M. D.; Bright, T. B.; Allara, D. L.; Chidsey, C. E. Spontaneously Organized Molecular Assemblies. 4. Structural Characterization of n-Alkyl Thiol Monolayers on Gold by Optical Ellipsometry, Infrared Spectroscopy, and Electrochemistry. *J. Am. Chem. Soc.* **1987**, *109*, 3559–3569.
- (47) Lee, S.; Shon, Y. S.; Colorado, R.; Guenard, R. L.; Lee, T. R.; Perry, S. S. Influence of Packing Densities and Surface Order on the Frictional Properties of Alkanethiol Self-Assembled Monolayers (SAMs) on Gold: A Comparison of SAMs Derived from Normal and Spiroalkanedithiols. *Langmuir* **2000**, *16*, 2220–2224.
- (48) Chinwangso, P.; St. Hill, L. R.; Marquez, M. D.; Randall Lee, T. Unsymmetrical Spiroalkanedithiols Having Mixed Fluorinated and Alkyl Tailgroups of Varying Length: Film Structure and Interfacial Properties. *Molecules* **2018**, *23*, 2632.
- (49) Chinwangso, P.; Lee, H. J.; Lee, T. R. Self-Assembled Monolayers Generated from Unsymmetrical Partially Fluorinated Spiroalkanedithiols. *Langmuir* **2015**, *31*,

13341–13349.

- (50) Kushmerick, J. G.; Weiss, P. S. Scanning Probe Microscopes. In *Encyclopedia of Spectroscopy and Spectrometry*; Academic Press: Cambridge, 2016.
- (51) Dupont-Gillain, C. C.; Fauroux, C. M. J.; Gardner, D. C. J.; Leggett, G. J. Use of AFM to Probe the Adsorption Strength and Time-Dependent Changes of Albumin on Self-Assembled Monolayers. *J. Biomed. Mater. Res. - Part A* **2003**, *67A*, 548–558.
- (52) Jalili, N.; Laxminarayana, K. A Review of Atomic Force Microscopy Imaging Systems: Application to Molecular Metrology and Biological Sciences. *Mechatronics* **2004**, *14*, 907–945.
- (53) Variola, F. Atomic Force Microscopy in Biomaterials Surface Science. *Phys. Chem. Chem. Phys.* **2015**, *17*, 2950–2959.
- (54) Engel, A.; Lyubchenko, Y.; Müller, D. Atomic Force Microscopy: A Powerful Tool to Observe Biomolecules at Work. *Trends Cell Biol.* **1999**, *9*, 77–80.
- (55) Schönherr, H.; Vancso, G. J. Atomic Force Microscopy in Practice. In *Scanning Force Microscopy of Polymers*; Springer: Berlin, 2010.
- (56) Friedbacher, G. Atomic Force Microscopy (AFM). In *Surface and Thin Film Analysis: A Compendium of Principles, Instrumentation, and Applications, Second Edition*; Wiley-VCH: Weinheim, 2011.

- (57) Cruz, T. G. S.; Albuquerque, D. A. C.; De, R. R. L.; Yamaji, F. M.; Leite, F. L. Measurement of the Nanoscale Roughness by Atomic Force Microscopy: Basic Principles and Applications. In *Atomic Force Microscopy - Imaging, Measuring and Manipulating Surfaces at the Atomic Scale*; IntechOpen: London, 2012.
- (58) Yablon, D. G. Overview of Atomic Force Microscopy. In *Scanning Probe Microscopy for Industrial Applications: Nanomechanical Characterization*; John Wiley & Sons, Inc.: Hoboken, 2013.

## **Chapter 5. Conclusions**

The work presented in this dissertation developed a protocol to incorporate a synergistic approach, combining multiple techniques, to evaluate the anti-fouling properties of SAMs. The method provided a robust and reliable means to determine the protein resistant properties, consistent with a variety of proteins, and insight into the interactions at the protein-adsorbate interface. Chapter 1 provided an overview of various analytical techniques that have been used to qualitatively or quantitatively analyze biofilm formation on the surface of self-assembled monolayers (SAMs).

In Chapter 2, SAMs were generated from unsymmetrical partially fluorinated spiroalkanedithiols to evaluate their performance towards protein adhesion; the analogous monothiol adsorbates were included as a reference. Surface plasmon resonance (SPR) and quartz crystal microbalance (QCM) both confirmed that the partially fluorinated spiroalkanedithiols possessed improved anti-fouling properties over the monothiol analogues. Atomic force microscopy (AFM) provided insight to the ellipsometric analysis results, which showed greater error as a result of increased scatter but confirmed that the surfaces maintained the overall trend that partially fluorinated spiroalkanedithiol adsorbates can reduce the non-specific absorption of proteins. The branched structure of the adsorbate, for the inclusion of the secondary alkyl chain, was found to influence the order of the films, which provided an environment to better resist protein adhesion. It is likely that the non-restricted conformation of the fluorocarbons in this type of adsorbate maximized van der Waals interactions between the fluorocarbon chains, which ultimately led to the improved anti-fouling properties of the SAMs.

In Chapter 3, the anti-fouling properties of SAMs generated from unsymmetrical oligo(ethylene glycol) (OEG) spiroalkanedithiols were evaluated and compared to the those of the monothiol congeners. The SAMs were investigated with the complementary techniques ellipsometry, SPR, QCM, and AFM to determine the influence of adsorbate structure on the anti-fouling properties of the resulting films. Results obtained through QCM and SPR confirmed that the tri(ethylene glycol) monothiol maintained the best performance, compared to the spiroalkanedithiol SAMs, which exhibited higher protein adhesion than the hydrocarbon monothiol. However, between the two spiroalkanedithiols, the shorter alkyl chain length film was found to adhere less protein than the longer chained congener. The increase in protein adhesion is likely due to the addition of the hydrocarbon chain, which restrains the degrees of freedom of the OEG chain -- a crucial factor in resisting protein adhesion. It is likely that the OEG portion is able to sit on top of the shorter hydrocarbon chain, which allows for less disruption in the degrees of freedoms, as seen by the lower protein adhesion between the aforementioned SAMs. The increased adhesion of protein observed from this study, has inspired the use of these adsorbates in use a biosensor for the detection of proteins at low concentrations.

In Chapter 4, binary SAMs composed of various ratios of a hydrocarbon and a partially fluorinated aromatic dithiol were generated and their anti-fouling properties evaluated using ellipsometry, X-ray photoelectron spectroscopy (XPS), and QCM. Furthermore, the mixed surfaces were investigated using ellipsometry, QCM, and AFM as complementary techniques to determine the anti-adhesive properties of the SAMs. The synergistic studies revealed that the mixed SAMs exhibited improved protein resistant properties compared to the single component SAMs that is likely attributed to the

conformational order introduced by mixed nature of the surface, allowing for maximized van der Waals interactions.

Overall, an approach was developed to investigate the anti-fouling properties of self-assembled monolayers using ellipsometry, surface plasmon resonance spectroscopy, quartz crystal microbalance, and atomic force microscopy as complementary techniques. The various analytical techniques provide a robust synergistic characterization method with reproducibility to determine the anti-fouling properties of mixed interfaces. Surfaces containing species that are conflicted in nature exhibited properties that impacted the structure of the SAMs, which ultimately alters their ability to interact with proteins and their anti-fouling properties. This multi-approach method is currently being employed to investigate other SAM surfaces to characterize the anti-fouling properties and biofilm formation in a holistic approach. Future work may include analysis of AFM imaging patterns to explore molecular modeling of protein interactions with the substrate surface.